NAVAL POSTGRADUATE SCHOOL

MONTEREY, CALIFORNIA

THESIS

ENHANCING THE SCIENCE COLLECTION CAPABILITY OF NASA'S LUNAR RECONNAISSANCE ORBITER (LRO)

by

Travis A. Lippman

December 2017

Thesis Co-Advisors: Mark Karpenko
Isaac M. Ross

THIS PAGE INTENTIONALLY LEFT BLANK

REPORT DOCUMENTATION PAGE

Form Approved OMB No. 0704–0188

1. AGENCY USE ONLY *(Leave Blank)*	2. REPORT DATE	3. REPORT TYPE AND DATES COVERED
	December 2017	Master's Thesis 09-28-2015 to 12-15-2017

4. TITLE AND SUBTITLE

ENHANCING THE SCIENCE COLLECTION CAPABILITY OF NASA'S LUNAR RECONNAISSANCE ORBITER (LRO)

5. FUNDING NUMBERS

6. AUTHOR(S)

Travis A. Lippman

7. PERFORMING ORGANIZATION NAME(S) AND ADDRESS(ES)

Naval Postgraduate School
Monterey, CA 93943

8. PERFORMING ORGANIZATION REPORT NUMBER

9. SPONSORING / MONITORING AGENCY NAME(S) AND ADDRESS(ES)

N/A

10. SPONSORING / MONITORING AGENCY REPORT NUMBER

11. SUPPLEMENTARY NOTES

The views expressed in this document are those of the author and do not reflect the official policy or position of the Department of Defense or the U.S. Government. IRB Protocol Number: N/A.

12a. DISTRIBUTION / AVAILABILITY STATEMENT

Approved for public release. Distribution is unlimited.

12b. DISTRIBUTION CODE

13. ABSTRACT *(maximum 200 words)*

The mission of NASA's Lunar Reconnaissance Orbiter (LRO) was to map the Moon's surface when it was launched in 2009. Since then, LRO's mission set has expanded to include providing scientific data to contribute to a better understanding of the lunar surface, its history, potential lunar habitat, as well as a more general understanding of human spaceflight for future lunar or other terrestrial missions. With seven different payload instruments onboard the LRO, daily operations of the spacecraft are requested by different scientist communities and ultimately approved and implemented through the LRO mission operations center. The mission effectiveness is limited by the target planning process and the vehicle capabilities. Currently, NASA Goddard is interested in improving the throughput of the mission. The focus of this thesis is to address this challenge and to develop an automated process for target selection as well as solve for a rapid slew to the desired targets.

An automated target selection strategy is developed based on bipartite graph theory. An example is presented that demonstrates the usefulness of this approach. To ensure the plan can be executed and the science objectives satisfied, rapid slew maneuvers are developed using optimal control theory. A key challenge to the rapid slew is meeting operational constraints, which are treated as path constraints in optimal control. It is shown that the slew time for a payload instrument science target can be reduced by up to 50%.

14. SUBJECT TERMS

optimal control, target selection, minimum-time maneuvers, rapid slew, reaction wheel, bipartite graph theory, Lunar Reconnaissance Orbiter

15. NUMBER OF PAGES 143

16. PRICE CODE

17. SECURITY CLASSIFICATION OF REPORT	18. SECURITY CLASSIFICATION OF THIS PAGE	19. SECURITY CLASSIFICATION OF ABSTRACT	20. LIMITATION OF ABSTRACT
Unclassified	Unclassified	Unclassified	UU

NSN 7540-01-280-5500

Standard Form 298 (Rev. 2–89)
Prescribed by ANSI Std. 239–18

THIS PAGE INTENTIONALLY LEFT BLANK

Approved for public release. Distribution is unlimited.

ENHANCING THE SCIENCE COLLECTION CAPABILITY OF NASA'S LUNAR RECONNAISSANCE ORBITER (LRO)

Travis A. Lippman
Lieutenant, United States Navy
B.S., United States Naval Academy, 2011

Submitted in partial fulfillment of the
requirements for the degrees of

MASTER OF SCIENCE IN ASTRONAUTICAL ENGINEERING
and
ASTRONAUTICAL ENGINEER

from the

NAVAL POSTGRADUATE SCHOOL
December 2017

Approved by: Mark Karpenko
Thesis Co-Advisor

Isaac M. Ross
Thesis Co-Advisor

Garth V. Hobson
Chair, Department of Mechanical and Aerospace Engineering

THIS PAGE INTENTIONALLY LEFT BLANK

ABSTRACT

The mission of NASA's Lunar Reconnaissance Orbiter (LRO) was to map the Moon's surface when it was launched in 2009. Since then, LRO's mission set has expanded to include providing scientific data to contribute to a better understanding of the lunar surface, its history, potential lunar habitat, as well as a more general understanding of human spaceflight for future lunar or other terrestrial missions. With seven different payload instruments onboard the LRO, daily operations of the spacecraft are requested by different scientist communities and ultimately approved and implemented through the LRO mission operations center. The mission effectiveness is limited by the target planning process and the vehicle capabilities. Currently, NASA Goddard is interested in improving the throughput of the mission. The focus of this thesis is to address this challenge and to develop an automated process for target selection as well as solve for a rapid slew to the desired targets.

An automated target selection strategy is developed based on bipartite graph theory. An example is presented that demonstrates the usefulness of this approach. To ensure the plan can be executed and the science objectives satisfied, rapid slew maneuvers are developed using optimal control theory. A key challenge to the rapid slew is meeting operational constraints, which are treated as path constraints in optimal control. It is shown that the slew time for a payload instrument science target can be reduced by up to 50%.

THIS PAGE INTENTIONALLY LEFT BLANK

Table of Contents

List of Figures

List of Tables

THIS PAGE INTENTIONALLY LEFT BLANK

List of Acronyms and Abbreviations

ADCS	Attitude Determination and Control System
CRaTER	Cosmic Ray Telescope for the Effects of Radiation
DLRE	Diviner Lunar Radiometer Experiment
LAMP	Lyman-Alpha Mapping Project
LEND	Lunar Exploration Neutron Detector
LOLA	Lunar Orbiter Laser Altimeter
LRO	Lunar Reconnaissance Orbiter
LROC	Lunar Reconnaissance Orbiter Camera
Mini-RF	Miniature Radio Frequency Radar
NPS	Naval Postgraduate School
NASA	National Aeronautics and Space Administration

THIS PAGE INTENTIONALLY LEFT BLANK

Acknowledgments

I would like to thank Dr. Ross and Dr. Karpenko for inspiring me to continually seek out knowledge and challenging me to always understand the problem I am trying to solve. I entered graduate classes with little interest in trajectory planning or guidance and control theory and their teaching style and passion have completely changed that for me.

I would also like to acknowledge the continued support and technical knowledge provided by the Lunar Reconnaissance Orbiter program office located at NASA Goddard. The team was quick to respond to any requests for information and were gracious hosts for two visits, which were instrumental in my pursuit of this thesis.

Finally, I would like to thank my beautiful wife, Mylee, who has continuously supported me throughout this journey while also taking care of our baby girl, Evie, and our dog, Cosmo. Without her support it would be difficult to achieve even a small portion of what I have been able to.

THIS PAGE INTENTIONALLY LEFT BLANK

CHAPTER 1:
Introduction

1.1 The Scientific Mission

Throughout our upbringing, humankind has always exerted an enormous amount of time and interest in trying to understand the environment. Science is one of the most integral foundations of education in order to understand the environment. Science has evolved as our ability to observe has—these two ideas are intertwined. In the last half century, one major advance in our ability to better scientifically understand concepts from an atomic to a macro level has been through satellites and their observations. Scientific discovery made possible by a satellite dates back to as far as January of 1958, when Explorer 1 discovered the Van Allen radiation belts with its cosmic ray detector [1]. With the advances in technology, specifically the ability to produce parts with less mass, satellites can now be outfitted with state-of-the-art sensors for performing a number of vastly different scientific missions. NASA has numerous satellites, past and present, which were launched with the primary purpose of gathering scientific data to further understand the world in which we live.

The purpose of this thesis is to explore how one can maximize science output from spacecraft assets. Although this short mission statement may sound simple, it carries a lot of important concepts with it. Firstly, what does it mean to maximize science output? Could one person interpret an answer to this question differently than another? Thus, in order to actually "maximize" science, one must be able to first characterize, or put a value, to it and have that value agreed upon by the experts within a particular field. Secondly, what are the constraints? Examples of constraints to this type of problem are target selection (i.e., what to observe and when), physical capability of the spacecraft, limitations of the given remote sensor, ability to store and transmit data, and the mechanisms in place to be able to process any received data. Thirdly, once a targeting plan is decided for a particular spacecraft, the way in which the maneuvers are performed to collect the targets may impact the amount of science data that can actually be acquired.

A typical satellite may be outfitted with any number of payload sensors (instruments) and these need to be prioritized in some manner. In general, target prioritization is done manually by the human component of the missions operations team. The human component could be multiple stakeholders or a single individual–it just depends on the way the missions operations center (or its equivalent) is setup. The payload sensors of the satellite were installed because they directly contribute to the scientific community in some way. The operations team will generate a slew plan that is for some window of time, detailing exactly how they want the satellite to maneuver. For example, the missions team may establish that they want the satellite to observe Target 1 on Day 1 and Target 2 on Day 2. The desired plan must be constructed in a way such that it can be transmitted to the satellite Telemetry Tracking Navigation and Control (TTNC) subsystem. This being said, it can be seen that a ground station of some kind is required to transmit the commanding data. Once the data is received by the satellite, it must be stored onboard, within the Command and Data Handling (C&DH) subsystem. The satellite then executes the slew plan. If a target capture is desired, the payload sensor initiates and raw data is collected. Depending on design, this data can be compressed or uncompressed, processed or remain unprocessed, and may be encrypted if desired. Depending on the architecture, the satellite may store the data and dump periodically when in view of a ground station, or there may be some real-time downlink capability. Once the data is received on the ground, the mission data obtained from the payload needs to be reviewed and interpreted by the scientists who made the requests.

1.2 Thesis Scope and Objectives

The objectives of this thesis are threefold. Firstly, bipartite graph theory will be used to demonstrate its usability for autonomous target selection. This process is useful in that it is one that could automate the process from target request to target capture, reducing timeliness and complexity involved with currently used manual techniques. Secondly, once a target is identified, optimal control theory will be used to establish a minimum time solution for a nadir-pointing to target capture slews. This theory can be used for any satellite and target and will take into account operational constraints such as physical limitations of the momentum exchange devices, the desired angular momentum rate of the spacecraft, and bright object (sometimes referred to as occultation) avoidance. Thirdly, an actual maneuver of the LRO

will be examined and compared to the minimum time solution in order to show how to reduce the slew time between targets. The combination of automated target selection and enhanced slew performance will ultimately enable NASA to increase the scientic throughout of the LRO mission.

1.3 Thesis Layout

The layout of this thesis will start broad and eventually narrow down to an actual maneuver comparison of the LRO. The background of the LRO will be discussed in Chapter 2. Bipartite graph theory and its use for autonomous target selection will be discussed in Chapter 3. An overview of satellite Attitude Determination and Control System (ADCS) and pointing of satellites will be explained in Chapter 4. Chapter 5 will go a step further and discuss applications of slewing and pointing to real-world applications. This will include reference frame transformations and the introduction to operational constraints. A detailed problem formulation and the mathematical approach to solving a minimum time slew problem for a low-fidelity dynamics model (while considering path constraints) is solved in Chapter 6. A high-fidelity dynamics model of a satellite is then considered in Chapter 7. The rapid slew concept will then be applied to the LRO in Chapter 8. Chapter 8 will include a comparison between the currently used targeting technique to a possible minimum time solution. Two maneuvers actually implemented by NASA will be presented and compared against the rapid slew maneuver. Finally, concluding remarks and suggestions for future work will be presented in Chapter 9.

THIS PAGE INTENTIONALLY LEFT BLANK

CHAPTER 2:
Lunar Reconnaissance Orbiter

The purpose of this chapter is to describe the background and concept of operations for NASA's Lunar Reconnaissance Orbiter. It will include the different subsystems which must work together in order to meet the scientific mission of the satellite.

2.1 LRO Background

NASA's Lunar Reconnaissance Orbiter provides a great case study for the purposes of this thesis. The LRO was launched on June 18, 2009, to collect detailed information about the moon and its environment. The initial mission of the LRO was to map the Moon's surface and, "after a year of exploration, was extended with a unique set of science objectives" [2]. The LRO has continued to provide scientific data throughout, and has contributed to a better understanding of the Lunar surface, its history, potential Lunar habitat, as well as a more general understanding of human spaceflight for future Lunar or other terrestrial missions. The LRO is outfitted with seven instruments, each of which contribute to the scientific community when used individually or when used in combination. An overview of LRO's instruments is given in Figure 2.1. As shown in Figure 2.1, multiple instruments are available and, whether used individually or in conjunction with one another, the instruments can help to answer any number of scientific questions. To illustrate the wide spectrum of data available, LRO products for the Lunar south pole are displayed in Figure 2.2.

Instrument	Example key data products	Example of exploration benefits	Example of science benefits
LOLA Lunar Orbiter Laser Altimeter	35 m polar topography at < 10 cm vertical, global topography, surface slopes and roughness	Identify safe landing sites, image shadowed regions, map potential surface ice, improve gravity field model	Global topography and gravity for interior structure and geological evolution
LROC Lunar Reconnaissance Orbiter Camera	Thousands of 50 cm/pixel images, and entire Moon at 100 m in UV, Visible. Polar illumination conditions	Surface landing hazards, locations of near constant solar illumination	Impact and volcanic processes, resource evaluation, and crustal evolution
LEND Lunar Exploration Neutron Detector	Maps of hydrogen in upper 1 m of Moon at 10 km scales, neutron albedo	Locate potential water-ice in lunar soil or concentrations of implanted hydrogen	Distribution, sources, and history of polar volatiles
DLRE Diviner Lunar Radiometer Experiment	500 m scale maps of surface temperature, albedo, rock abundance, and ice stability	Measures thermal environment in permanent shadow and permanent light ice stability depth map	Distribution, sources, and history of polar volatiles
LAMP Lyman Alpha Mapping Project	Maps of frosts and landforms in permanently shadowed regions (PSRs)	Locate potential water-ice on the surface, image shadowed areas, and map potential landing areas in PSRs	Distribution, sources, and history of polar volatiles
CRaTER Cosmic Ray Telescope for the Effects of Radiation	Lunar and deep space radiation environment and tissue equivalent plastic response to radiation	Safe, lighter weight space vehicles. Radiation environment for human presences at the Moon and journeys to Mars and beyond	Radiation boundary conditions for biological response. Map radiation reflected from lunar surface
Mini-RF Technology Demonstration	X and S-band radar imaging and interferometry	Demonstrate new lightweight SAR and communication technologies, locate potential water-ice	Source, history, deposition of polar volatiles

Figure 2.1. LRO instrument overview. Source: [3].

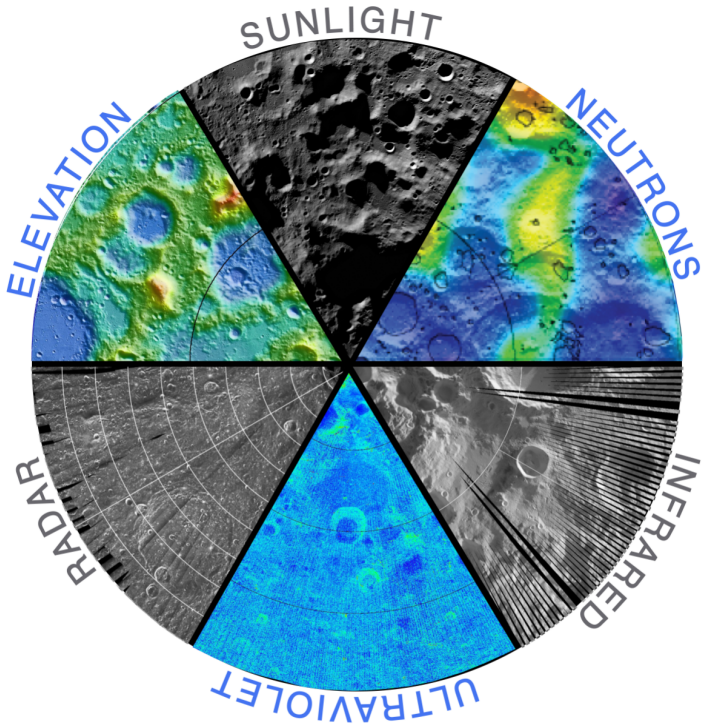

Figure 2.2. Full spectrum image capability of the LRO for the Lunar south pole. Source: [4].

2.2 LRO Current State of Practice

Prior to discussing ideas on on how to maximize the science collected by the LRO, it is important to examine the current standard operating procedures; more specifically, an understanding of how target selection and maneuvering is currently done. With seven separate scientific instruments, it is essential to task the sensors to targets that are selected by subject matter experts with the hope of answering a larger question or achieving some specific scientific purpose. Typically, any one of the seven payload stakeholders (or scientists) provide a target or instrument calibration request in the form of a verbal description or by delivering roll, pitch, and yaw maneuver requests with final and settling time requirements and the duration time specified [5]. These inputs are given to the mission operations team to ensure no two requests interfere with one another. A weekly slew plan request is created and loaded into NASA's ADCS attitude maneuver planning utility software, AttMan. AttMan interfaces with the attitude ground system software and creates a slew plan, both daily and for the upcoming week. The AttMan software was written to try and satisfy all maneuvering requirements, such as meeting power and thermal requirements, as well as bright object avoidance. It was written in MATLAB and the NASA team has continued to evolve the package since the LRO launch in 2009 [6]. If AttMan determines that the maneuver cannot be accomplished, it will inform the team which constraint or constraints were violated and the maneuver request can either be modified as appropriate or canceled. If AttMan approves the maneuver and the maneuver is not greater than 20 degrees, the data will be up-linked to the LRO, typically in the form of commanded roll, pitch, and yaw. If AttMan approves the maneuver but there is greater than a 20 degree rotation, then the MOC will further study the maneuver for adherence to the various engineering constraints and approve or disapprove it. The current state of practice for operating LRO is shown in Figure 2.3.

The higher level tasking of the LRO mission planning is primarily done by each instrument team inputting their specific maneuver requests to the NASA operations team. The requests are selected by the subject matter experts to answer or partially answer a larger question. For example, the question may be asked "Is there existing water on the Lunar surface?" The team in charge of LEND may choose to test for the concentration of existing hydrogen in a permanently shadowed target area of the Moon, where cold temperatures would keep the water static and frozen.

For the most part, the instrument teams do not have direct access to the existing NASA

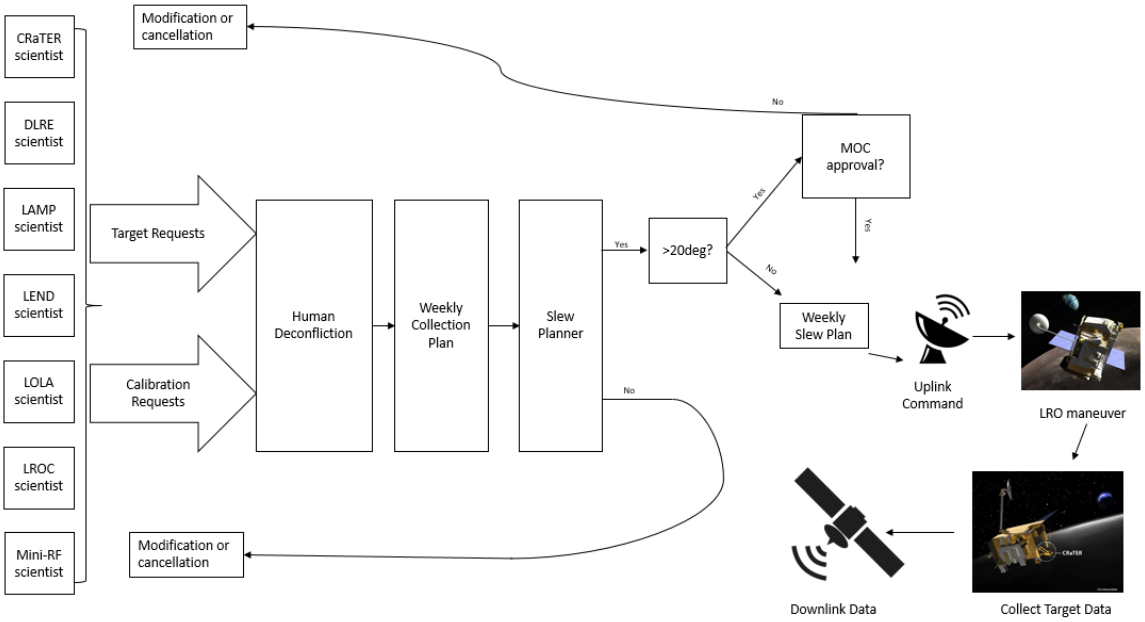

Figure 2.3. Current state of practice for the LRO.
Adapted from [7].

AttMan software and can only provide their slew requests in terms of roll, pitch, and yaw maneuvers or a combination thereof. They do, however, know the orbit and the target they would like to point at. Typically, a maneuver request will consist of date, desired change in roll, pitch, yaw, and final, settling and duration times. If two maneuvers appear to conflict with one another, a person at NASA is designated to help resolve the situation. This may simply be by reaching back to the scientific community and asking if a particular request can be shifted in time or it could be the rejection of one of the requests. Some maneuver requests are to point an instrument or star tracker to a specific orientation in order to test or calibrate. These calibration requests are usually large, timely maneuvers when compared to target pointing and extra attention should be paid to when these are scheduled.

After the higher level tasking has been sorted out, a weekly slew plan is generated. Note that although the weekly slew plan is established, it is visited again every 24 to 48 hours and modified if there are any requested updates. The AttMan software is the primary source of the trajectory planning for the LRO [5].

Regardless of the type of input, per NASA documentation, the output of AttMan will be in the form of any of the following three methods:

1. Offsets from nominal (nadir) attitude in LOCS.
2. Absolute attitudes given at every time step.
3. Absolute attitudes given as a few long, direct slews. [8]

The output of AttMan is processed by the ground station software and uplinked to the LRO and stored onboard the spacecraft. The attitude of the LRO is known to a high degree through the use of three different types of sensors. The types of sensors are (1) Course Sun Sensors (CSS); (2) Inertial Reference Unit (IRU); (3) Star Trackers [9]. There are a total of ten CSS, which provide some redundancy. The locations of the sensors are shown in Figure 2.4.

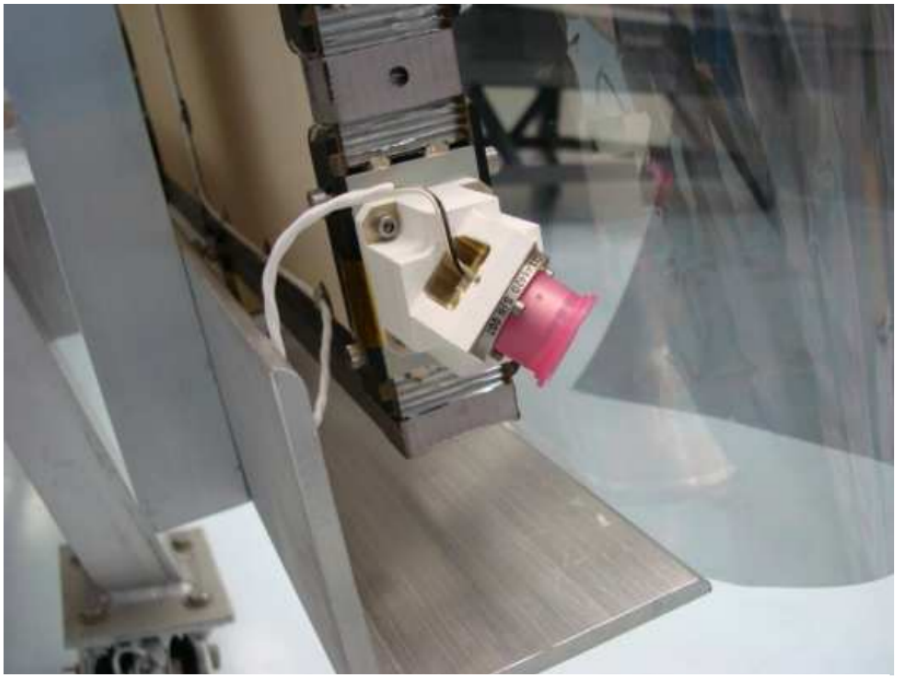

Figure 2.4. Photograph of a LRO course Sun sensor. Source: [10].

There is a single, 3-axis unit IRU. Two star trackers are used, which output the quaternion attitude representation in ECI to the star tracker reference frame (ST). Because these three types of sensors were installed, the attitude state of the LRO is assumed to be known to a

high degree at any given instant in time. The measurements from the sensors is down-linked to any of the Near Earth Network NASA ground stations so operators on the ground can track the state of the spacecraft as well.

Dynamic modeling of the LRO was completed by NASA and is incorporated in MATLAB. Simulink software, which is a subset of the overall MATLAB program, was also used to model the dynamics. Actuators, dynamics, and environmental models are all included. Ephemeris data, noise, spacecraft properties (i.e., moment of inertia), and sensor modeling is also included. It was determined that the high fidelity model will be used to test the rapid slew trajectories that are developed as part of this thesis.

Low-level actuator control is accomplished on board LRO at the desired time tag after the slew plan has been uplinked to it. Maneuver is accomplished through a quaternion error feedback control, in either inertial or off-nadir quaternion reference frames. In general, the quaternion error feedback control system is incorporating quaternion attitude representation along with a standard PD controller. This will be discussed further in Chapter 4.

To further illustrate the current state of practice for LRO attitude maneuvers original NASA documents were examined. The different types of maneuvers LRO can execute are outlined below:

1. Transitions
    - Slewing LRO between inertial and nadir-pointing nominal attitudes.
2. Thrust vector pointing
    - Thrusters are nominally used to support orbit maneuvers.
3. Roll, pitch, and yaw slews
    - Roll, pitch, or yaw the LRO to desired attitude by specified angles, either in one step or multiple steps. This is the primary type of manuever required for science data gathering and sensor calibrations.
4. Sensor calibration slews
    - Specific maneuver for the sensor calibrations, either commanded by roll, pitch, yaw offsets or as an absolute attitude.
5. Z-axis pointing slews
    - Align the body +Z axis to a selected target on an Earth ground station or a given right ascension/declination, while satisfying constraints.

6. Mini-RF calibration
    - Align the Mini-RF instrument with a selected Earth ground station. The option also exists to sweep across the long or short Mini-RF axis with the scan direction specified relative to the Earth north/south direction.
7. Lunar eclipse attitude
    - Align LRO to maximize power prior to eclipse to minimize heat loss during an eclipse. [6]

There are six operational constraint considerations for the LRO, which were also obtained from NASA documentation.

1. Sun avoidance constraint
    - A Sun keep-out cone was defined in order to protect the +Z (nadir) pointing instruments, with a cone half-angle of 63 degrees.
2. Power constraint
    - In order to provide solar power, the angle between the Sun and the body -Y axis must be small.
3. Slew rate constraint
    - The magnitude of the angular velocity is 0.10 degree/sec per axis.
4. Omni-antenna constraint
    - Omni-antenna performance is maximized when keeping Earth in a referred quadrant in X-Y plane; only applicable to the cruise phase from Earth to Lunar orbit.
5. Star tracker constraint
    - There are two ASTs (star trackers), each with a circular field of view (FOV) of 8.2 degrees, which must not be occulted by the Sun, Earth, or Moon. The exclusion angles, measured from the center of the FOV to the limb of the interfering body, were selected to be 25 degrees for the Sun, 15 degrees for the Moon, and 15 degrees for the Earth. For Z-axis pointing, the rotation angle about the specified axis (Z or X, respectively) is chosen to avoid simultaneous AST interference while trying to keep some Sun on the -Y side.
6. Thermal constraints.
    - During extended Lunar eclipse, a specific attitude is commanded to conserve heat. Additionally, post launch analysis discovered that offsetting the solar

array by 30 degrees from the Sun was better for thermal control. For nominal nadir pointing, this was accomplished by a 30 degrees solar array gimbal angle offset. [6]

The maneuver types that will be considered in this thesis will be transitions, roll, pitch and yaw slews, and Z-axis pointing slews. The constraints that will be considered are the Sun avoidance and Star tracker constraints. The slew rate constraint will also be considered. Satisfaction of other constraints will be verified after maneuver design but before flight.

2.3 Summary

This chapter has provided some background information on the LRO and described the current operational work flow. Note that this rate limit has since been increased to $0.13\ deg/s$ [11]. The concept of operations of the LRO were explored and the maneuver types and operational constraints were defined.

With the mission and background of LRO defined, target prioritization and valuation can be discussed. In the following chapter, a bipartite graph approach will be used to demonstrate the potential for autonomous target selection.

THIS PAGE INTENTIONALLY LEFT BLANK

CHAPTER 3:
Applying Bipartite Graph Theory to the LRO

In this chapter, some concepts of graph theory will be defined. A subset of graph theory, referred to as bipartite graph theory, will be discussed as a means to assign some type of scientific value for any given target. If a scientific value can be assigned to any given target based on the overall goals of the mission team, target valuation and prioritization can be accomplished. First, a simple example of a bipartite graph will be presented to show the basic approach used with bipartite graph theory. This application will then be tied to the LRO.

3.1 Graph Theory Introduction

Graph theory can be linked in history to as far back as 1736, the year in which Leonhard Euler wrote an article where he proposed a method to solving "The Problem of the Konigsberg bridges" [12]. The River Pregel flowed through this historical city located in Eastern Prussia. The city of Konigsberg was located on an island, which was surrounded by the River Pregal, as shown in Figure 3.1.

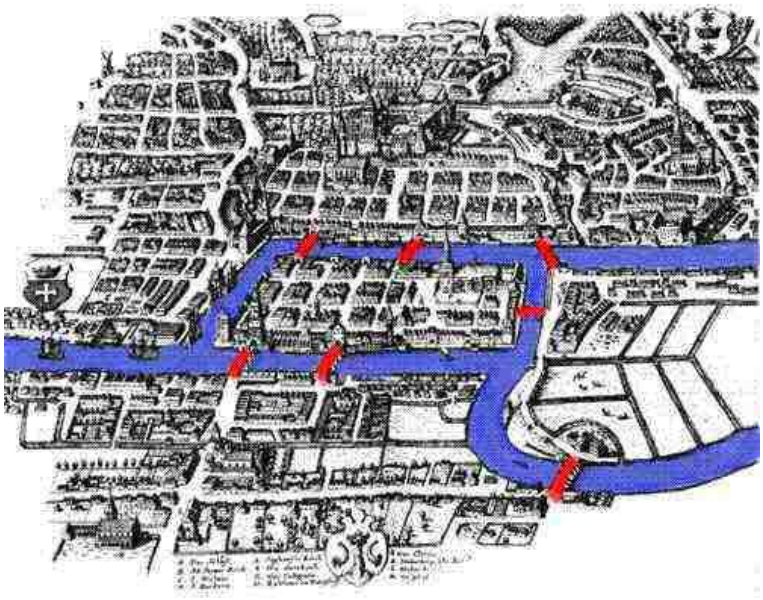

Figure 3.1. Geographical map of the River Pregal surrounding the city of Konigberg. Source: [13].

It is believed that some citizens of Konigberg used to entertain themselves by trying to create a plan to traverse the entire city while crossing each of the seven bridges only once. Because no one could come forward with a plan which met this objective, it was thought of as impossible. However, Euler wrote an article entitled "The solution of a problem relating to the geometry of position." In the article, Euler not only derived a solution to the Konigsberg bridge problem, but he also created a more general method, applicable to a variety of problems [12]. A breakthrough occurred when Euler realized that the physical map does not matter; what really matters mathematically is the list or pictorial depiction (graph) of which regions are connected by the bridges [14], and graph theory was born.

Since Euler, graph theory has proven extremely useful to solve numerous different types of problems, both real-world and purely mathematical. To demonstrate the large variety of problems in which graph theory has been used as a solution technique, some examples will be listed. As described in an introductory text for graph theory, the concept can be used to solve the following types of problems: "How can we lay cable at minimum cost to make every telephone reachable from every other? What is the fasted route from the national capital to each state capital? How can n jobs be filled by n people with maximum

total utility? What is the maximum flow per unit time from source to sink in a network of pipes? How many layers does a computer chip need so that wires in the same layer don't cross? How can the season of a sports league be scheduled into the minimum number of weeks?" [15].

Clearly, graph theory goes beyond visually representing a problem. It is a subset of mathematics which can be used to solve many problems for real-life applications. Before applying a graph theory approach—specifically a bipartite graph for target valuation—it is necessary to establish some definitions.

3.2 Graph Theory Definitions

In general, a "graph [**G**] consists of a finite set of vertices [**V**], a finite set of edges [**E**], and a rule [that defines] which edges join which pairs of vertices" [12]. A graph can be visualized by drawing a point for each vertex and drawing a curve for each edge between the vertices, in accordance with the rule set. For example, Figure 3.2 is a graph consisting of four vertices (points) and three edges (lines connecting the points). In another example, for the map shown in Figure 3.1, each region would be represented by a vertex and the bridges connecting the regions would be represented by an edge.

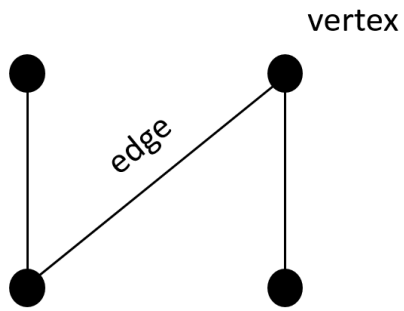

Figure 3.2. Example of a graph.

3.2.1 Bipartite Graphs Defined

As defined in [16], "a graph **G** is bipartite if the vertex set **V**(**G**) can be partitioned into two sets V_1 and V_2 in such a way that no two vertices from the same set are adjacent. The

sets V_1 and V_2 are called color classes of G and (V_1,V_2) is a bipartition of G. In fact a graph being bipartite means that the vertices of G can be colored with at most two colors, so that no two adjacent vertices have the same color... [A graph shall be called] m by n bipartite, if $|V_1| = m$ and $|V_2| = n$." An example 3 by 2 bipartite graph is shown in Figure 3.3. Note that, per the definition, no vertex can be connected to a like vertex; rather, the only path option that exists is for a black and white dot to be connected or nothing at all. In other words, any of the x-labeled vertices cannot be connected together, nor any of the y-labeled vertices can be connected together. This stems from the definition that no two vertices from the same set or color can be adjacent (or connected) with one another.

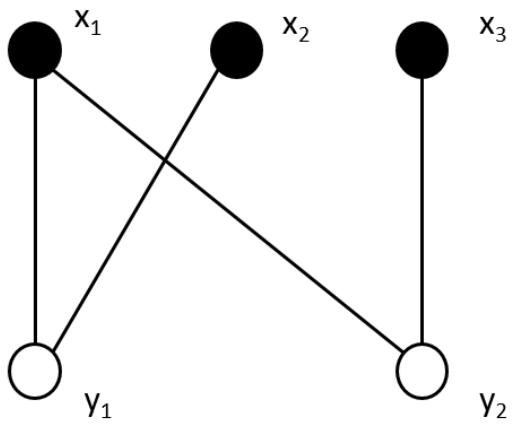

Figure 3.3. Example of a bipartite graph.

In this context, it can be seen that V_1 and V_2 can be used to link relationships of one category to another. For example, one could use x_i to represent i number of automobile owners, and y_j to represent the types of automobiles. A simple linkage (edge) between the two sets can convey the meaning that "Person x_i owns automobile y_j." If person x_i owns two separate automobiles, another edge will be used to connect the person to the other vehicle. Although this example may seem overly simplistic, the powerful ability of a bipartite representation to mathematically represent large data sets can prove to be extremely advantageous; for example, to facilitate decision making.

3.2.2 Mathematical Representation of a Bipartite Graph

Let Figure 3.4 be a given bipartite graph. One way to mathematically represent this graph is to use binary representation, where a 0 represents no connection between the different sets and a 1 represents that the edge exists. The binary representation can be presented in a table (see Table 3.1).

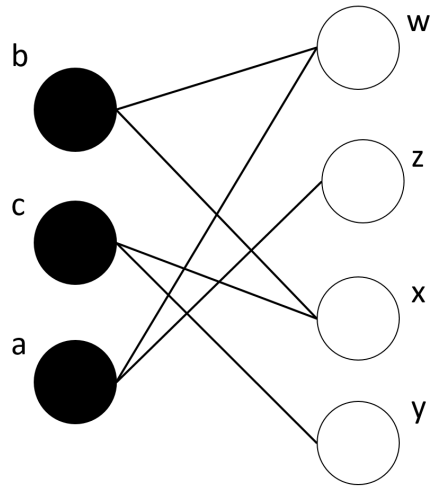

Figure 3.4. Another bipartite graph example.

Table 3.1. Tabular representation of a bipartite graph.

	w	x	y	z
a	1	0	0	1
b	1	1	0	0
c	0	1	1	0

The table data, then, can be represented by a matrix of m by n dimensions; in this case 3 by 4, as shown in (3.1).

$$C = \begin{bmatrix} 1 & 0 & 0 & 1 \\ 1 & 1 & 0 & 0 \\ 0 & 1 & 1 & 0 \end{bmatrix} \tag{3.1}$$

3.3 Expanding the Bipartite Graph

Once the definition and mathematical interpretation of bipartite graphs are understood, the basic principles can be expanded to solve or represent larger problem sets. In the above examples, the bipartite graph consisted of only two vertex sets (V_1 and V_2). One way to represent a more complex problem is by adding additional vertex sets. An example will be used to demonstrate the concept.

Consider three individuals who are interested in buying new vehicles. Mylee wants a car or a truck, Evie only wants a truck, and Travis only wants a SUV, as shown in Table 3.2. However, the only dealerships in the vicinity are Jeep, Subaru, Ford, and Lexus. The types of vehicles that each dealership sells is summarized in Table 3.3.

Table 3.2. Individual vehicle preferences.

Person	Desired Vehicle Type(s)
Mylee	Car or Truck
Evie	Truck
Travis	SUV

Table 3.3. Available products from each dealership.

Vehicle Brand	Offered Vehicle Type(s)
Jeep	SUV
Subaru	Car
Ford	SUV, Car, Truck
Lexus	SUV, Car

In this example, there are two separate opportunities to represent the data utilizing a bipartite graph; the first being the individual person to their preference of vehicle type and the second being the vehicle types offered by the different dealerships. By connecting these two otherwise disparate bipartite graphs, a direct link can be made to establish which dealerships the individual can go to. This is represented in Figure 3.5, where the set $V_1(G)$ represents the individuals, set $V_2(G)$ represents the vehicle types, and set $V_3(G)$ represents the available dealerships. In this case, $E_1(G)$ represents the edges between the individual and desired vehicle type and $E_2(G)$ represents the edges between vehicle types and dealership.

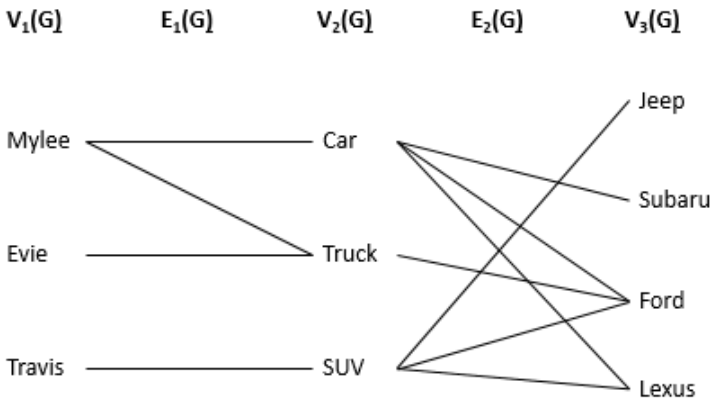

Figure 3.5. A bipartite graph for vehicle selection.

The corresponding tabular representations of $E_1(G)$ and $E_2(G)$ are given in Table 3.4 and Table 3.5, respectively.

Table 3.4. Table derived from $E_1(G)$.

	Car	Truck	SUV
Mylee	1	1	0
Evie	0	1	0
Travis	0	0	1

Table 3.5. Table derived from $E_2(G)$.

	Jeep	Subaru	Ford	Lexus
Car	0	1	1	1
Truck	0	0	1	0
SUV	1	0	1	1

Matrix representations for $E_1(G)$ and $E_2(G)$ are given in (3.2) and (3.3), respectively. The matrix variable names were arbitrarily selected.

$$\mathbf{X}_1 = \begin{bmatrix} 1 & 1 & 0 \\ 0 & 1 & 0 \\ 0 & 0 & 1 \end{bmatrix} \tag{3.2}$$

$$\mathbf{X}_2 = \begin{bmatrix} 0 & 1 & 1 & 1 \\ 0 & 0 & 1 & 0 \\ 1 & 0 & 1 & 1 \end{bmatrix} \tag{3.3}$$

Note that $\mathbf{X}_1$ and $\mathbf{X}_2$ can be multiplied together. The result will be a 3 by 4 matrix, where the three rows represent each individual, and the four columns represent the available dealerships. The resultant matrix, $\mathbf{R}$, is shown below in (3.4). To interpret the results, the resultant matrix was also transformed back into a more readable tabular form, as seen in Table 3.6.

$$\mathbf{R} = \mathbf{X}_1 * \mathbf{X}_2 = \begin{bmatrix} 1 & 1 & 0 \\ 0 & 1 & 0 \\ 0 & 0 & 1 \end{bmatrix} * \begin{bmatrix} 0 & 1 & 1 & 1 \\ 0 & 0 & 1 & 0 \\ 1 & 0 & 1 & 1 \end{bmatrix} = \begin{bmatrix} 0 & 1 & 2 & 1 \\ 0 & 0 & 1 & 0 \\ 1 & 0 & 1 & 1 \end{bmatrix} \tag{3.4}$$

Table 3.6. Tabular form derived from (3.4).

	Jeep	Subaru	Ford	Lexus
Mylee	0	1	2	1
Evie	0	0	1	0
Travis	1	0	1	1

The resultant matrix, $\mathbf{R}$, takes into account the desires of each individual and directly ties them to the dealerships that can suit his or her needs. Not only does the resultant matrix encode the connections, it can be used to support decision making. For example, it is observed that a value of 2 is calculated for Mylee going to the Ford dealership. This is correlated to the fact that the Ford dealership can offer Mylee more value or selection, because in one visit she can view both cars and trucks (which is what she wanted). This added value may be something that Mylee would like to consider before making her vehicle searching plans!

A bipartite graph representation seems to be a natural way to model scientific target selection and valuation for a satellite mission. This is explored next.

3.4 Automated Target Prioritization and Valuation

Previous sections have discussed possible applications for the use of bipartite graph theory. This section explores if bipartite graphs can be used to help answer the following scientific questions, given a sensor or network of heterogeneous sensors:

1. What instrument will give the most "value" at the given time?
2. What area of interest should be targeted in order to obtain the highest value?

Establishing what items will make up the vertex sets is a prerequisite to using bipartite graph theory. The approach used in this thesis was to start at the right side of the bipartite graph system at most restrictive (or narrow) tasks or questions. Each subsequent vertex set that was connected (visually to the left) would represent a broader set of tasks or questions.

3.4.1 Defining the Vertex Sets

Due to LRO having seven separate instruments, the LRO mission is a prime candidate to test if the mathematical method of bipartite graphs could be applied when determining scientific value available from a given Lunar target at any given time. First, each instrument was studied in order to determine, at the most basic level, its purpose. These basic purposes were termed "atomic tasks". The atomic tasks of each instrument were derived from [3] to create a vertex set, in order to apply bipartite graph theory. The atomic tasks identified for each instrument are listed below.

1. CRaTER
    - Measure the energy deposited in the silicon detectors by charged particles and photons entering the telescope.
2. DLRE
    - Measure the irradiance from the surface of the Moon.
3. LAMP
    - Perform spectrographic analysis.
4. LEND
    - Detect neutron collisions and associated energy.
    - Detect when a high energy neutron collides with a hydrogen nucleus.
5. LOLA
    - Activate the LASER in accordance with 5 spot pattern.

6. LROC
    - Take a picture with the Narrow Angle Camera (NAC).
    - Take a picture with the Wide Angle Camera (WAC).
7. Mini-RF
    - Collect synthetic aperture radar (SAR) data.

Once the basic purpose of each instrument was understood, a more broad set of mission level questions was explored. These were more inclusive and not tied to an individual instrument, but rather developed to help answer a larger scientific question. These were termed "molecular" questions or tasks. Examples are included below:

1. Is there an abundance of hydrogen?
2. Are there any cold traps where ice could have been preserved?
3. What is the Lunar surface temperature?
4. What is the Lunar subsurface temperature?
5. What is the characterization of deep space radiation in Lunar orbit?
6. Is the Lunar surface region of interest flat?
7. Is the Lunar surface illuminated?
8. Are potential landing hazards present?
9. Measure Lunar topography.
10. Take a high resolution picture.
11. Can future communication technologies be demonstrated?
12. Is the Lunar surface region of interest permanently shadowed?
13. Create an image of the Lunar surface.

It should be noted that the above list was constructed as a means to demonstrate a basic approach of bipartite graphs in order to prove the concept. When evaluating from the atomic level all the way up to to the most broad, any number of groups of intermediate questions/tasks could be considered. In this case, the overarching "macro" question, molecular, and atomic levels were considered. In this study, only three overarching questions were considered:

1. Is there evidence of water?
2. Is there a favorable landing spot?
3. What is the radiation environment in a particular direction?

Each macro question was then tied either to a single or to multiple areas of interest. To illustrate the idea, assume LRO to be in a stationary orbit about the moon. The total Lunar surface view available is broken up into different areas of interest (or targets) that have been identified as having potential to provide scientific a value of some kind. A total of six areas of interest, labeled A-F are considered as in Figure 3.6. The areas of interest are scalable; in other words, changing the number of areas of interest will not change any of the steps needed to calculate the scientific value. One will simply deal with larger or smaller matrices.

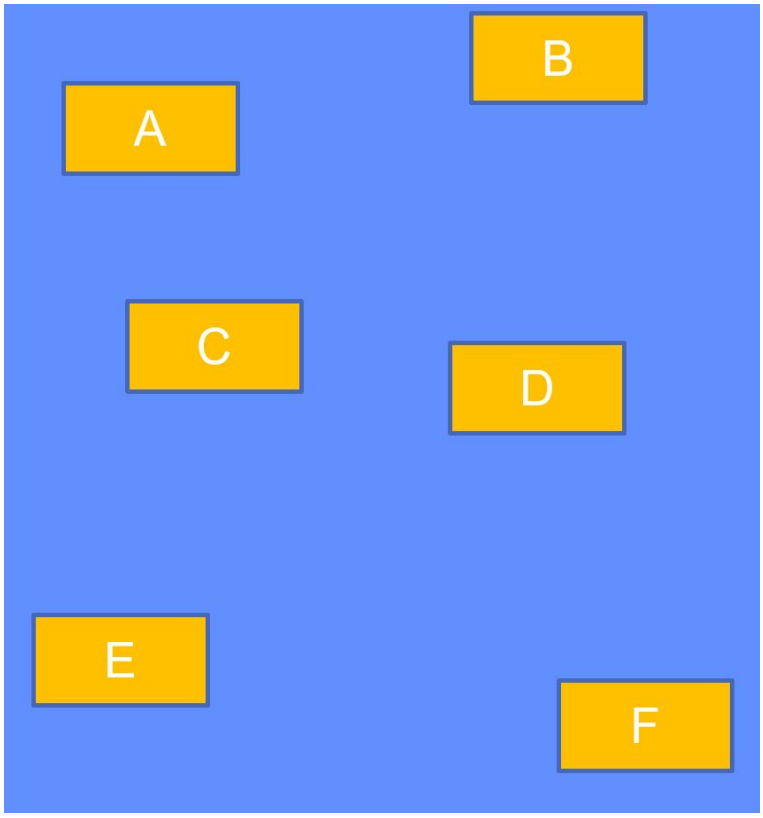

Figure 3.6. Lunar surface view of areas (A-F) of scientific interest.

Lunar surface view of the LRO from stationary orbit. A-F are the identified areas of scientific interest.

To further illustrate the flow, each instrument on the LRO is designed to answer specific questions. If one were to ask if a particular area on the Lunar surface were smooth, both the panchromatic camera or synthetic aperture radar may be used to help answer that question.

Looking next at a broader level, asking if an area is smooth may be one of several questions pertaining to a larger question. In this case, the question could be whether that particular area would be a safe landing spot for a manned spacecraft. The procedure started at the most specific atomic level and broadened until the macro questions could be answered.

There are three overarching questions tied to specific targets.

1. Is there evidence of water in A, B, C, or D?
2. Is there a favorable landing spot location in C or F?
3. Is there an opportune radiation reading opportunity in B or E?

Four vertex sets have thus been established. These are shown in Table 3.7.

Table 3.7. Vertex sets for LRO science gathering example.

Vertex Set	Category
V_1	Area Target
V_2	Broad Science Question
V_3	Intermediate Question
V_4	Atomic Task/Individual Sensor

3.4.2 Bipartite Graph Results for Automated Targeting

A series of bipartite graphs were set up to interpret the results of linking an overarching question to specific sensors through a series of bipartite graphs, as shown in Figure 3.7. The vertex and edge sets are represented by $\mathbf{V}_i$ and $\mathbf{E}_i$ in the assigned column. Since there are three different sets of edges within this bipartite graph, three matrices were developed to mathematically represent them, $\mathbf{X}_{E_1}$, $\mathbf{X}_{E_2}$, and $\mathbf{X}_{E_3}$. The representative matrices for the edge connections connecting the Question, Intermediate (IM) Question, and Sensor are shown in (3.5) through (3.7), respectively.

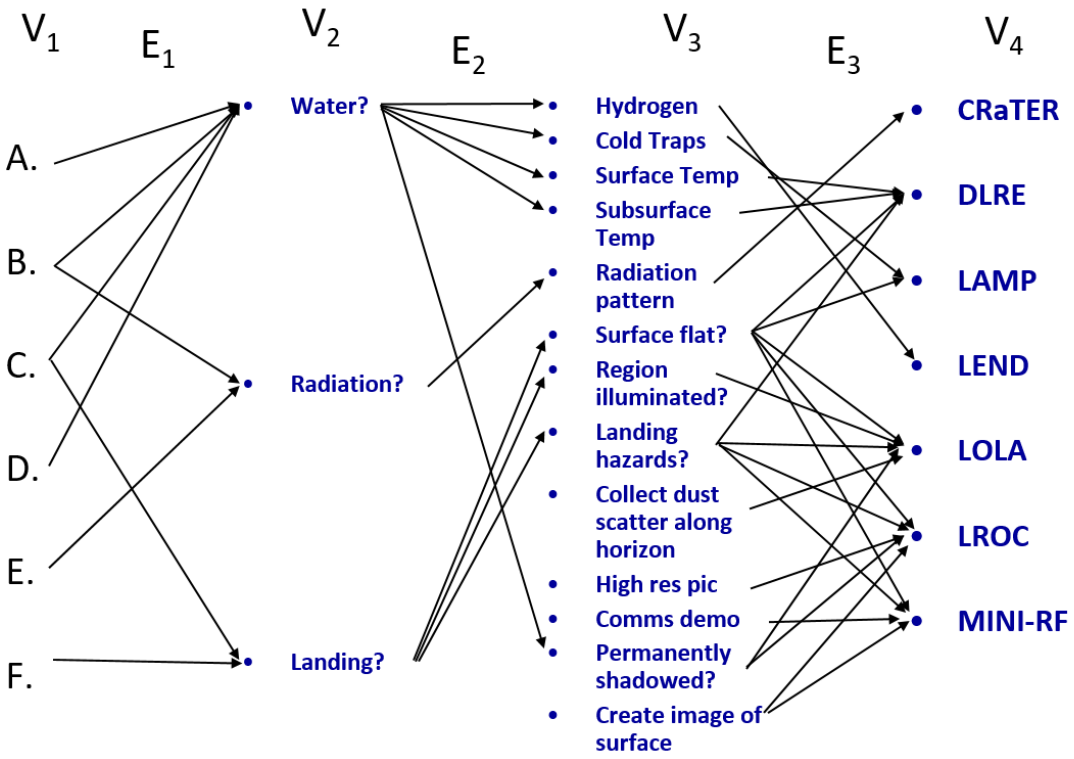

Figure 3.7. Example bipartite graph for the LRO mission.

$$\mathbf{X}_{E_1} = \begin{bmatrix} 1 & 0 & 0 \\ 1 & 1 & 0 \\ 1 & 0 & 1 \\ 1 & 0 & 0 \\ 0 & 1 & 0 \\ 0 & 0 & 1 \end{bmatrix} \tag{3.5}$$

$$\mathbf{X}_{E_2} = \begin{bmatrix} 1 & 1 & 1 & 1 & 0 & 0 & 0 & 0 & 0 & 0 & 0 & 1 & 0 \\ 0 & 0 & 0 & 0 & 1 & 0 & 0 & 0 & 0 & 0 & 0 & 0 & 0 \\ 0 & 0 & 0 & 0 & 0 & 1 & 1 & 1 & 0 & 0 & 0 & 0 & 0 \end{bmatrix} \tag{3.6}$$

$$\mathbf{X}_{E_3} = \begin{bmatrix} 0 & 0 & 0 & 1 & 0 & 0 & 0 \\ 0 & 0 & 1 & 0 & 0 & 0 & 0 \\ 0 & 1 & 0 & 0 & 0 & 0 & 0 \\ 0 & 1 & 0 & 0 & 0 & 0 & 0 \\ 1 & 0 & 0 & 0 & 0 & 0 & 0 \\ 0 & 1 & 1 & 0 & 1 & 1 & 1 \\ 0 & 0 & 0 & 0 & 1 & 0 & 0 \\ 0 & 1 & 0 & 0 & 1 & 1 & 1 \\ 0 & 0 & 0 & 0 & 1 & 0 & 0 \\ 0 & 0 & 0 & 0 & 0 & 1 & 0 \\ 0 & 0 & 0 & 0 & 0 & 0 & 1 \\ 0 & 0 & 0 & 0 & 1 & 1 & 0 \\ 0 & 0 & 0 & 0 & 0 & 1 & 1 \end{bmatrix} \tag{3.7}$$

The resultant matrix (**R**) was then calculated utilizing (3.8), where $\mathbf{X}_{E_1}$, $\mathbf{X}_{E_2}$, and $\mathbf{X}_{E_3}$ were multiplied together. The calculated result is shown in Figure 3.8. The resultant matrix is an *m* by *n* matrix, where *m* is the number of targets and n is the number of instruments; in this case a 6 by 7. The dimensions have been shown next to each edge matrix, showing that the dimensions are appropriate for the matrix multiplication operations.

$$\mathbf{R}|_{[6x7]} = \mathbf{X}_{E_1}|_{[6x3]} * \mathbf{X}_{E_2}|_{[3x14]} * \mathbf{X}_{E_3}|_{[14x7]} \tag{3.8}$$

Transforming the resultant matrix back into tabular form, it can be observed that the Grid Locations (or area targets) make up the rows and the sensors to employ make up the columns.

GRID LOCATION	CRATER	DLRE	LAMP	LEND	LOLA	LROC	MINI-RF
A	0	2	1	1	1	1	0
B	1	2	1	1	1	1	0
C	0	4	2	1	4	3	2
D	0	2	1	1	1	1	0
E	1	0	0	0	0	0	0
F	0	2	1	0	3	2	2

Figure 3.8. Example resultant matrix for automated targeting of the LRO mission.

3.4.3 Interpreting the Results

Depending on the application or ultimate goal of a particular system, one may interpret the entries of the resultant matrix of Figure 3.8 in different ways. For this analysis, four interpretations are described, but others can also be conceived.

The four interpretations of the resultant matrix are:

1. Column Sum
2. Max Column
3. Row Sum
4. Max Row

Column Sum

The column sums of the resultant matrix were calculated and are shown in Figure 3.9. By taking the column sums, one can determine which instrument provides the most value for the overall set of questions. Referring to Figure 3.9, it is evident that operating the DLRE would provide the most value since DLRE output can be used to help answer the most macro questions.

GRID LOCATION	CRATER	DLRE	LAMP	LEND	LOLA	LROC	MINI-RF
A	0	2	1	1	1	1	0
B	1	2	1	1	1	1	0
C	0	4	2	1	4	3	2
D	0	2	1	1	1	1	0
E	1	0	0	0	0	0	0
F	0	2	1	0	3	2	2
Column Sum	2	12	6	4	10	8	4

Figure 3.9. Column sum of the resultant matrix.

Max Column

The maximum of each columns of the resultant matrix were identified and are shown in Figure 3.10.

GRID LOCATION	CRATER	DLRE	LAMP	LEND	LOLA	LROC	MINI-RF
A	0	2	1	1	1	1	0
B	1	2	1	1	1	1	0
C	0	4	2	1	4	3	2
D	0	2	1	1	1	1	0
E	1	0	0	0	0	0	0
F	0	2	1	0	3	2	2
Max	1	4	2	1	4	3	2

Figure 3.10. Maximum column of the resultant matrix.

By examining the column maximum, one can determine which instrument provides the single highest value for a particular target. Therefore, if only one target can be acquired, it should be target C using DLRE or LOLA.

Row Sum

The row sums of the resultant matrix were calculated and are shown in Figure 3.11.

By taking the row sums, one can determine which target provides the most "scientific value." In this context, note that scientific value is associated with how much knowledge can be

GRID LOCATION	CRATER	DLRE	LAMP	LEND	LOLA	LROC	MINI-RF	Row Sum
A	0	2	1	1	1	1	0	6
B	1	2	1	1	1	1	0	7
C	0	4	2	1	4	3	2	16
D	0	2	1	1	1	1	0	6
E	1	0	0	0	0	0	0	1
F	0	2	1	0	3	2	2	10

Figure 3.11. Row sum of the resultant matrix.

gained that contributes to any of the overarching scientific questions. Considering the row sums, it would seem best to collect on Target C using all the instruments but CRATER.

Max Row

The maximum of each row of the resultant matrix were identified and are shown in Figure 3.12.

GRID LOCATION	CRATER	DLRE	LAMP	LEND	LOLA	LROC	MINI-RF	Max
A	0	2	1	1	1	1	0	2
B	1	2	1	1	1	1	0	2
C	0	4	2	1	4	3	2	4
D	0	2	1	1	1	1	0	2
E	1	0	0	0	0	0	0	1
F	0	2	1	0	3	2	2	3

Figure 3.12. Maximum row of the resultant matrix.

By examining the row maximum, one can determine which target provides the most “scientific value" for any individual instrument. In this case, if only one instrument can be used and only one target acquired, DLRE should be used to target Target C.

3.4.4 Weighted Matrices

Rather than taking a binary approach for the bipartite graphs, where a one is used to indicate that a connection exists and a zero is used to indicate no connection, there is an opportunity

to place a weighting scale to any or all of the vertex sets. For example, detecting an abundance of hydrogen directly by the neutron detector (LEND) may be more valuable than determining if the area is permanently shadowed using the laser altimeter (LOLA) if asking whether water may be present in a particular area. Both contribute to answering the overall question; hydrogen must be present in the water molecule and permanently shadowed areas are more likely to sustain frozen water due to the frigid temperatures. In this case, detecting an abundance of hydrogen is more valuable to a scientist in search of water than knowledge of a permanently shadowed location. The weighting scale could range from zero to one, where the numerical value would be evaluated and established by a subject matter expert.

3.5 Summary

This chapter has introduced bipartite graph theory and the related mathematical concepts. A bipartite graph approach was then tied to a satellite mission, where the ultimate goal was to prioritize and value potential targets based on the overarching scientific questions of the missions team. Specifically, a series of bipartite graphs were developed for the LRO based on realistic overarching scientific questions and its seven instruments. It was demonstrated that one can calculate a resultant decision matrix, which can be interpreted by the team to autonomously prioritize and value potential targets as desired. Finally, the idea of weighting the edge matrices was presented, which can allow the subject matter experts an additional tool to assist in more realistically representing the scenario.

CHAPTER 4:
Slewing and Pointing

Many spacecraft have a requirement to slew and point in order to fulfill mission requirements. This chapter will provide an introductory look as to how satellites achieve slewing and pointing requirements. In general, slewing refers to a continuous rotational motion, commonly used to maneuver the spacecraft from one target to another. Pointing refers to the spacecraft payload locking in on a target for a period of time. The chapter will focus on the fundamentals of how a spacecraft achieves slewing and pointing. An overview of a standard quaternion-error feedback control algorithm will be discussed. The Attitude Control System (ACS) logic of LRO will also be explained.

4.1 Maneuvering Considerations for Spacecraft

For context, the term slew is used to represent rotational motion of the spacecraft. These rotations are typically referred to as roll, pitch, and yaw. Slewing of a spacecraft can be accomplished in many ways. In general, rotations of the spacecraft are achieved by propulsive thrust, internal energy dissipation, or momentum transfer [17]. For satellites which require slewing and pointing as part of their mission set, transfer of momentum is the most common and is the method described in this chapter. The transfer of momentum to achieve rotation of a satellite can be accomplished by using either reaction wheels or control moment gyros (CMGs). This chapter will focus on the utilization of reaction wheels to achieve three-axis stabilization and rotational control, as it aligns directly to the LRO.

If mounted rigidly inside the body of the spacecraft, a reaction wheel provides torque along a single axis within the body-fixed reference frame. The reaction wheel is typically powered via the bus electrical control system and electrical energy is converted to mechanical energy in order to spin a wheel. The wheel moment of inertia about its spin axis, combined with its angular velocity, make up its momentum state, as shown in (4.1), where I_{spin} represents the wheel moment of inertia about its spin axis and ω_{wh} represents the angular velocity of a single wheel. The maximum rotation speed of the wheel represents its maximum angular momentum capability, meaning it would be operating at the edge of its momentum envelope. This is represented in (4.2).

$$h_{wh} = I_{spin}\omega_{wh} \tag{4.1}$$

$$h_{wh_{max}} = I_{spin}\omega_{wh_{max}} \tag{4.2}$$

A reaction wheel torque is produced whenever there is a non-zero time variation of the wheel angular velocity. If the reaction wheel rotation rate is held constant, the total angular momentum of the spacecraft can simply be expressed in the inertial frame as shown in (4.3), where $\mathbf{H}$ is angular momentum, $\mathbf{I}$ represents the spacecraft moment of inertia, and ω is the satellite body rotational velocity with respect to the inertial frame.

$$\mathbf{H} = \mathbf{I}\boldsymbol{\omega} + h_{wh} \tag{4.3}$$

Torque is defined as the time derivative of the angular momentum in the inertial frame, as shown in (4.4). Torque can also be trasnformed into the body frame, as seen in (4.5). By substituting in the terms for angular momentum, Euler's Equation of Motion is obtained and is shown in (4.6) [17].

$$\boldsymbol{\tau} = \left.\frac{dH}{dt}\right|_I \tag{4.4}$$

$$\boldsymbol{\tau} = \left.\frac{dH}{dt}\right|_B + \boldsymbol{\omega} \times \mathbf{H}\Big|_B \tag{4.5}$$

$$\boldsymbol{\tau} = \mathbf{I}\dot{\boldsymbol{\omega}} + \boldsymbol{\omega} \times \mathbf{I}\boldsymbol{\omega} \tag{4.6}$$

If no other external torques act on the body, the Conservation of Angular Momentum dictates that the torque produced by the reaction wheel must be the result of an 'exchange' from the spacecraft body in the inertial frame [17]. Therefore, the total angular momentum equation can be expanded, as shown in (4.7). Note that the direction cosine matrix C_{BN} has been included to transfer the angular momentum produced by the reaction wheel from the body frame to the inertial frame. Since $\mathbf{H}|_I$ must be constant, it can be seen that a change

in reaction wheel momentum can be traded for spacecraft rate, or vice-versa.

$$\mathbf{H} = \mathbf{I}\boldsymbol{\omega} + C_{BN} I_{spin} \omega_{wh} = \text{constant} \tag{4.7}$$

A spacecraft requires a minimum of three reaction wheels, each aligned about a separate axis, to achieve three-axis stabilization. Typically, an array of four reaction wheels are utilized for redundancy [17]. A common practice is to configure the array in a pyramid scheme, such that a failure of any single reaction wheel can be tolerated and three-axis control maintained. As an example, the LRO employs a tetrahedron reaction wheel array assembly configuration, which is shown in Figure 4.1. The distribution of torque in any given direction can be calculated by multiplying by the torque distribution matrix, **Z**, which can be expressed mathematically by projecting each wheel's angular momentum along each axis of rotation. The three rows of **Z** represent the angular momentum about the roll, pitch, and yaw axis, respectively. Each row represents a different wheel, where a_{ij} notation dictates a dot product between unit vectors for axis i and reaction wheel j. The resulting **Z** matrix equation is shown in (4.8).

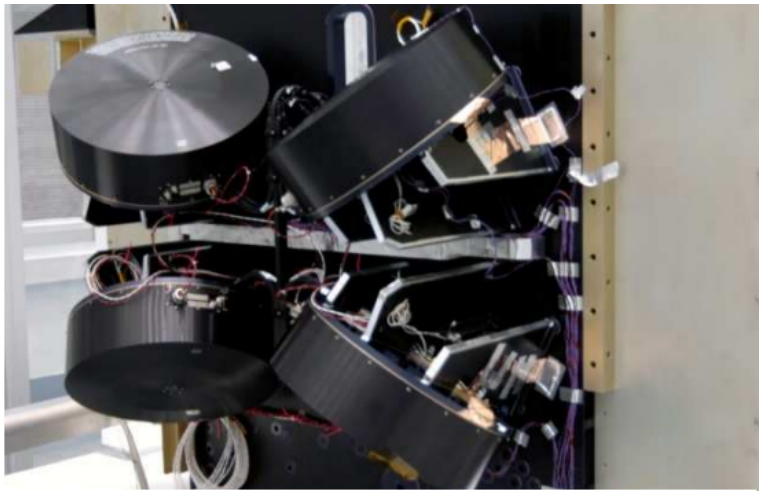

Figure 4.1. LRO reaction wheel assembly. Source: [10].

$$\mathbf{Z} = \begin{pmatrix} a_{11} & a_{12} & a_{13} & a_{14} \\ a_{21} & a_{22} & a_{23} & a_{24} \\ a_{31} & a_{32} & a_{33} & a_{34} \end{pmatrix} \tag{4.8}$$

(4.7) can now be restated when including the reaction wheel distribution matrix, as shown in (4.9). Let $\mathbf{\Omega}_w$ represent the vector of the reaction wheel angular rates that make up the assembly.

$$\mathbf{H} = \mathbf{I\Omega}_w + C_{BN}\mathbf{Z}h_{wh} = \text{constant} \tag{4.9}$$

Using these relationships, the satellite capabilities can now be modeled.

4.2 Modeling

4.2.1 Satellite Dynamics

In this section the dynamical model for a typical reaction wheel satellite is developed by combining kinematics with the dynamic relationships described above.

For any spacecraft, a model may be constructed by assembling the differential equations for the attitude kinematics and the rotational dynamics together with the equations describing the dynamics of the reaction wheel array. In this thesis the attitude of the satellite is parameterized using a quaternion representation, with the differential equation [18] defined in (4.10).

$$\dot{\mathbf{q}} = \mathbf{Q}(\omega)\mathbf{q} \tag{4.10}$$

where

$$\mathbf{Q}(\omega) = \frac{1}{2}\begin{bmatrix} 0 & \omega_3 & -\omega_2 & \omega_1 \\ -\omega_1 & 0 & \omega_1 & \omega_2 \\ \omega_2 & -\omega_1 & 0 & \omega_3 \\ -\omega_1 & -\omega_2 & -\omega_3 & 0 \end{bmatrix} \tag{4.11}$$

Euler's equations for the rotational motion of the satellite are reshown for the readers

convenience in (4.12) [18].

$$\mathbf{I}\dot{\boldsymbol{\omega}} = -\boldsymbol{\omega} \times (\mathbf{I}\boldsymbol{\omega} + \mathbf{h}) - \boldsymbol{\tau} \tag{4.12}$$

Vector $\mathbf{h}$ is the reaction wheel angular momentum and $\boldsymbol{\tau}$ is the reaction wheel control torque vector expressed in the spacecraft body-fixed frame.

The reaction wheel angular momenta and the reaction wheel control torques are transformed from the individual wheel spin axes to the spacecraft body-fixed frame by the computations in (4.13) and (4.14), shown again to illustrate the step-by-step development of developing a dynamical model.

$$\mathbf{h} = I_{\mathrm{w}}\mathbf{Z}\boldsymbol{\Omega}_{\mathrm{w}} \tag{4.13}$$

$$\boldsymbol{\tau} = \frac{d\mathbf{h}}{dt} = I_{\mathrm{w}}\mathbf{Z}\dot{\boldsymbol{\Omega}}_{\mathrm{w}} = \mathbf{Z}\boldsymbol{\tau}_{\mathrm{w}} \tag{4.14}$$

In (4.13) and (4.14), I_{w} is the inertia of the wheel rotor, $\boldsymbol{\Omega}_{\mathrm{w}}$ is the vector of reaction wheel angular rates, and $\mathbf{Z}$ is the column matrix of unit vectors relating the wheel spin axes to the spacecraft body-fixed frame, as previously discussed.

Selecting the state vector as $\mathbf{x} = [\mathbf{q}|\boldsymbol{\omega}|\boldsymbol{\Omega}]^T$, and the control vector as $\mathbf{u} = \boldsymbol{\tau}_{\mathrm{w}}$, gives the following state-space model of the spacecraft dynamics, as shown in (4.15).

$$\mathbf{x} = \begin{bmatrix} \mathbf{Q}(\boldsymbol{\omega})\mathbf{q} \\ \mathbf{I}^{-1}\left[-\boldsymbol{\omega} \times (\mathbf{I}\boldsymbol{\omega} + I_{\mathrm{w}}\mathbf{Z}\boldsymbol{\Omega}_{\mathrm{w}}) - \mathbf{Z}\mathbf{u}\right] \\ I_{\mathrm{w}}^{-1}\mathbf{u} \end{bmatrix} \tag{4.15}$$

This higher fidelity dynamic model can also be represented by allowing both the angular velocity and reaction wheel assembly torques as the control, provided the path constraints are written to represent the physical limitations of the spacecraft. This concept will be explored further in Chapter 7.

The initial rapid slew formulation, however, will first be developed using a low fidelity dynamics model (see Chapter 6). An initial low fidelity example provides a good study of how to apply optimal control while applying operational constraints while only taking into account the spacecraft kinematics. Low fidelity models also provide one with a general

idea of the solution and whether the desired maneuver is a feasible one. In the low fidelity problem formulation, the state of the spacecraft is the attitude (in quaternion form) and the control is the spacecraft angular velocity.

With a dynamical representation of the spacecraft, feedback control systems to achieve slewing and pointing requirements can be explored.

4.3 Inner Loop Control

Whether a spacecraft is desired to slew or stare at a particular target on the ground, an inner loop closed-feedback system is required. Although an open-loop control is theoretically possible in an idealized environment, any small disturbance will likely have an adverse impact on the orientation of the satellite. The space environment consists of many different types of disturbance torques, some of which may include drag for low earth orbit, magnetic disturbances, orbital perturbations due to orbiting a non-spherical body, and third body gravitational effects [17]. The inner-loop control law can be used to counter any effect on the spacecraft due to these undesired disturbances.

The guidance of the spacecraft is the commanded input to the spacecraft to achieve the desired state. This commanded input is then fed into the inner-loop Attitude Determination and Control System (ADCS), which determines the control required to slew or maintain orientation of the spacecraft. The control algorithm can be run at a preset frequency to continuously feed the required command torques to the reaction wheels. The reaction wheels accelerate accordingly to maneuver the spacecraft to the desired commanded guidance input. The actual or predicted state of the spacecraft is fed back and compared to the commanded input and an error signal is calculated, which is used to drive the controller. For the most common case where only orientation and angular velocity make up the desired states of the spacecraft, a classic PD or PID controller can be used [17]. Note that the desired output solution of the spacecraft may be simply identifying a desired initial and final state, or it could be a desired state at any given time-step—it is based on the operator's preference. A flow diagram of a simple Attitude Control System is shown in Figure 4.2.

Because many spacecraft utilize the quaternion representation to describe the orientation, a quaternion-error feedback control system can be used [17]. This control law is conceptually identical to the PD law, represented in (4.16), with the exception that there is additional

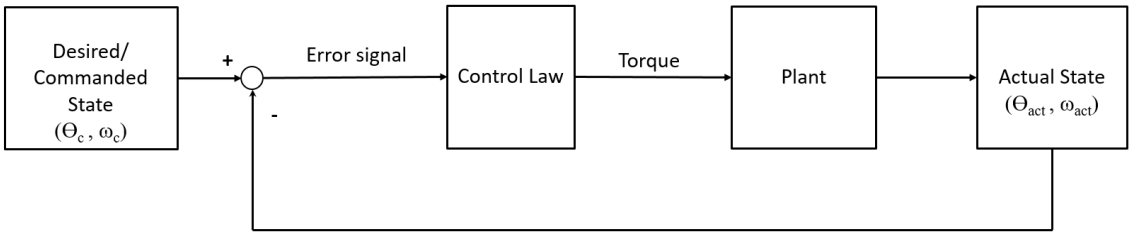

Figure 4.2. Schematic of feedback control system.

mathematics necessary to calculate the error signal for the rotation angles. This is because one cannot simply add or subtract one quaternion from another and have it represent anything meaningful. The proportional and derivative gains that can be manipulated to obtain the desired response of the control system are represented by k_p and k_d, respectively. The proportional gain is tied to the positional orientation of the spacecraft while the derivative gain is tied to the angular velocity. The calculated control output is represented by u.

$$u = k_p(x_c - x_{act}) + k_d(\dot{x}_c - \dot{x}_{act}) \tag{4.16}$$

The control law for a quaternion error feedback system is shown in (4.17) [17].

$$\mathbf{u} = -\mathbf{k}_p\mathbf{q}_e - \mathbf{k}_d\boldsymbol{\omega} \tag{4.17}$$

where $\mathbf{q}_e$ represents the quaternion error signal, which is a function of commanded and actual quaternion of the spacecraft at any point in time, as defined in (4.18). Note that $\boldsymbol{\omega}$ is also an error signal in this context.

$$\begin{bmatrix} q_{1_e} \\ q_{2_e} \\ q_{3_e} \\ q_{4_e} \end{bmatrix} = \begin{bmatrix} q_{4_c} & q_{3_c} & -q_{2_c} & -q_{1_c} \\ -q_{3_c} & q_{4_c} & q_{1_c} & -q_{2_c} \\ q_{2_c} & -q_{1_c} & q_{4_c} & -q_{3_c} \\ q_{1_c} & q_{2_c} & q_{3_c} & q_{4_c} \end{bmatrix} \begin{bmatrix} q_1 \\ q_2 \\ q_3 \\ q_4 \end{bmatrix} \tag{4.18}$$

The quaternion-error feedback control system is oftentimes used to command a spacecraft rotation about a single axis at a specified rotation angle. Given two vectors in the same

inertial frame, the Euler axis (also referred to as the eigenaxis) and rotation angle can be derived. This concept is based on Euler's eigenaxis rotation theorem, which states that any two vectors that are fixed to the body and stationary with respect to an inertial reference frame can maneuver from one orientation to another via a single axis, referred to as the eigenaxis, at a given rotation angle (Φ) [17]. The eigenaxis and rotation angle between two vectors of the same size (i.e., $\hat{\mathbf{a}}$ and $\hat{\mathbf{b}}$) which are represented in the same inertial frame can be calculated using the cross and dot products, respectively, as shown in (4.19) and (4.20).

$$\hat{\mathbf{e}} = \frac{\hat{\mathbf{a}} \times \hat{\mathbf{b}}}{|\hat{\mathbf{a}} \times \hat{\mathbf{b}}|} \tag{4.19}$$

$$\Phi = cos^{-1}(\hat{\mathbf{a}} \cdot \hat{\mathbf{b}}) \tag{4.20}$$

A quaternion attitude representation can be defined using the eigenaxis and rotation angle, as shown in (4.21) [17], where $\hat{e}_i$ represents the unit component of $\mathbf{e}$ for $i = 1, 2, 3$ respectively.

$$\mathbf{q} = \begin{bmatrix} \hat{e}_1 \sin(\Phi/2) \\ \hat{e}_2 \sin(\Phi/2) \\ \hat{e}_3 \sin(\Phi/2) \\ \cos(\Phi/2) \end{bmatrix} \tag{4.21}$$

Because the initial (nadir) orientation of $\mathbf{b}_1$ is prior to any rotation, $\mathbf{q}_0 = [0\ 0\ 0\ 1]$ and $\mathbf{q}_f$ is a function of the pointing vector and boresight. In other words, the output of (4.19) and (4.20) would be used in (4.21) to calculate $\mathbf{q}_f$. It should be noted that this method does constrain the yaw angle, since the problem was not defined using only roll and pitch. In any off-body axis rotations, slewing about the eigenaxis typically has roll, pitch, and yaw components associated with it.

Since the quaternion representation utilizes four components to represent a three-dimensional space, there is one additional constraint to consider, which can prove useful when validating if the derived $\mathbf{q}_f$ is feasible. This unitary norm constraint is shown in (4.22) [17].

$$q_1^2 + q_2^2 + q_3^2 + q_4^2 = 1 \tag{4.22}$$

For pointing, it may be desired to null out the steady state error of the system. One method of minimizing pointing error is to add an integrator into the control law, i.e., utilize a PID type control vice the previously discussed PD [17]. Although this can add a disadvantage of increasing the settling time required to maneuver from the initial to final state, the boresight alignment of the satellite will be able to hold pointing at the desired end-state to a higher tolerance. High tolerance pointing capability is advantageous for many types of payloads and subsystem components, such as cameras, radars, antennas, and autonomous star trackers. To further illustrate the concept, the logic associated with steering and pointing for LRO's Observing Mode will be examined. First, however, it is important to define some of the coordinate systems relevant to the LRO.

4.4 Coordinate Systems

4.4.1 Earth Centered Inertial

The inertial coordinate system selected for use by the LRO team is the Earth Centered Inertial [6], which is based on an epoch (time reference) of J2000. The +Z-axis is aligned with the North Pole, the axis of rotation for Earth. The +X-axis is defined at the point where the ecliptic plane appears to cross the Earth's equatorial plane from the northern to the southern hemisphere. The point of this intersection is oftentimes referred to as the vernal equinox or the first point of Ares. The +Y-axis completes the right hand orthogonal set [19]. Note that this coordinate system is fixed; it does not rotate with the Earth. A schematic form of the ECI coordinate system is shown in Figure 4.3.

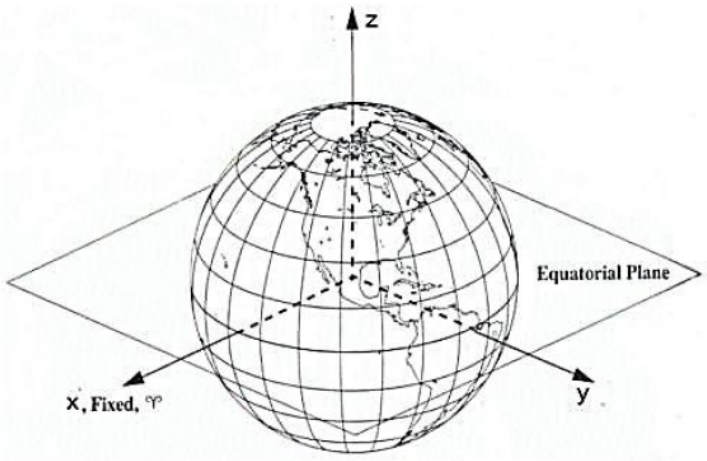

Figure 4.3. Earth Centered Inertial coordinate system. Source: [19].

4.4.2 Lunar Centric Orbital Coordinate System

The Lunar Orbit Coordinate System (Orbital Coordinate System or OCS abbreviated) is defined such that the +Z-axis points to the center of the Moon in the orbit plane, +X-axis is in the direction of orbital velocity, and the +Y axis completes the right hand orthogonal set [3]. The schematic form of the OCS is shown in Figure 4.4.

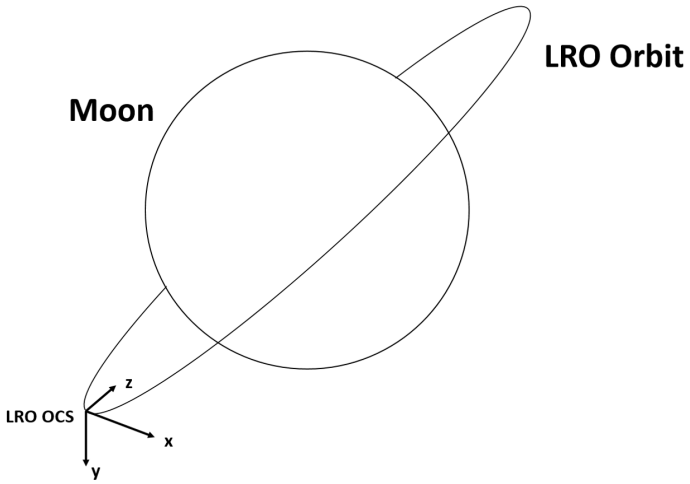

Figure 4.4. LRO Orbital Coordinate System.

4.4.3 Body Coordinate System

The Body Coordinate System (BCS) is defined such that the +X-axis is normal to the separation plane and extends up through the spacecraft. The +Z-axis is normal to the nadir face, and is parallel with the science nadir boresight. The +Y-axis completes the right hand orthogonal set [3]. A schematic of the BCS is shown in Figure 4.5.

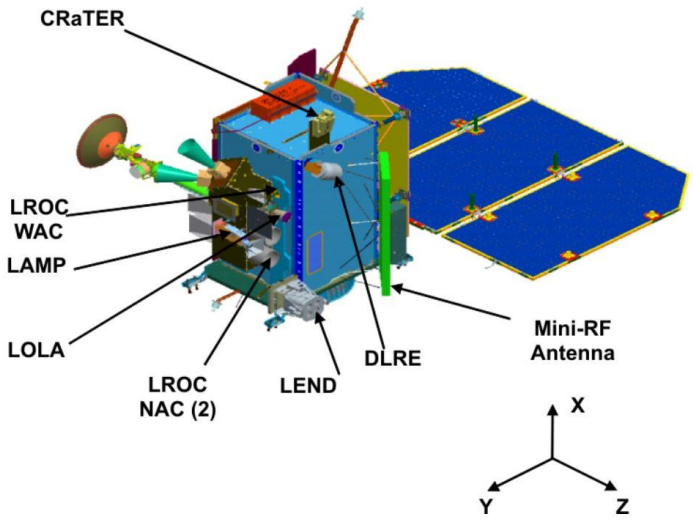

Figure 4.5. LRO Body Coordinate System. Source: [3].

4.5 LRO Observing Mode Attitude Control

The Observing Mode Attitude Control logic is listed in detail in [20]. All of the content presented in this section was derived from this source.

At initialization, the Attitude Control System (ACS) sets the integrated attitude errors to a preset value of 0. This is an important step because the angular errors are being estimated through an integrator calculation of measured angular velocity. In other words, the LRO takes the input angular velocity rates from its gyros and integrates over time to estimate the angles of rotation; without setting an initial known or guessed location, the angle state of the spacecraft could not be known.

Next, a best known value of the spacecraft moment of inertia is determined. Because moment of inertia changes based on the spacecraft configuration (i.e., location of the solar

panel), it cannot simply be held constant for all maneuvers. The developers elected to include a gain matrix used to modify the inertia matrix passed into the PID controller. In doing so, the spacecraft moment of inertia could be held constant, and the software simply would use the observable spacecraft moment of inertia $\mathbf{I}_{obs}$ for any dynamics calculations, which is defined as the product between the gain matrix $\mathbf{K}_{Inertia}$ and spacecraft moment of inertia $\mathbf{I}_{sc}$, as shown in (4.23).

$$\mathbf{I}_{obs} = \mathbf{K}_{Inertia}\mathbf{I}_{sc} \tag{4.23}$$

There are several different base target frame (BTG) target velocities, depending on the type of maneuver. For the target pointing operations that are the subject of this thesis, only the Non-Nadir Pointing mode BTG is of concern.

The estimated quaternion is then transformed from the Base Target Frame to the BCS frame. The commanded body rate is also converted from the BTG to BCS frame. The rate error is then calculated by subtracting the estimated body rates (obtained from the gyros) from the commanded body rate (based on the target quaternion type). Similarly, the attitude error is also computed utilizing (4.24).

$$\text{Attitude Error} = 2 \begin{bmatrix} q_{1_e} \\ q_{2_e} \\ q_{3_e} \end{bmatrix} \text{Sign}(q_{4_e}) \tag{4.24}$$

where the magnitude of the error is calculated by calculating the magnitude (2 Norm) of the attitude error.

Although specific LRO techniques are being listed, one can observe that the algorithms are in place to calculate the rate and attitude errors at any given point in time, which are needed to be input into (4.17) for the quaternion feedback control. One additional item LRO has in place, however, is the logic to apply proportional limiting to the attitude error. By placing a limit on the attitude error limit, a maneuver rate limit is imposed. If the attitude error or rate error exceeds a threshold value, the integral error is set to zero. If conducting a large maneuver, then, the error signals will certainty reach a threshold value prior entering the proximity of the target quaternion. As discussed previously, a PD controller is more useful

for the maneuver while the PID is more useful for settling and pointing. Once either or both of the error signals go below the threshold value, the integrator is again applied, allowing for the reduction of steady state pointing error.

Finally, the ACS applies feed forward torques, filters body control torques, computes wheel drag and wheel momentum redistribution torques. The control torques are then distributed to the wheels and wheel drag compensation and wheel momentum redistribution torque corrections are applied to produce the reaction wheel assembly control torque command. Proportional limiting is also applied to the commanded reaction wheel assembly control torque.

4.6 Summary

This chapter has introduced the concepts related to the slewing and pointing of spacecraft, specifically for those outfitted with reaction wheel assemblies. Inner loop control for attitude control was discussed and different types of control algorithms were introduced. One very common type of steering control logic used is quaternion error feedback control, a control which LRO logic is generally based upon. The ACS for LRO was then explained in more detail. The next chapter of the thesis will start to identify the mechanics and nuances necessary to apply the concepts discussed in this chapter to real-world applications.

THIS PAGE INTENTIONALLY LEFT BLANK

CHAPTER 5:
Summary of Slewing and Pointing in the Real World

The previous chapter identified mechanisms that satellites have in place to point to a desired target. However, the Attitude Control System alone does not provide enough for target collection capabilities. One must identify a desired coordinate system or reference frame of the target, and make transformations as appropriate in order to relate and compare spacecraft orientation, vectors, or a combination thereof with another when solving a problem. Along with this, ephemeris data that locates various objects with respect to a given reference frame must be known for the celestial bodies and satellite. Finally, operational constraints, some of which directly impact the trajectory of the satellite when in route to the target, must be taken into account. The purpose of this chapter is to provide further explanations for these additional real-world considerations.

5.1 Ephemeris and Coordinate Transformations

Ephemeris is data which identifies the coordinates of a celestial body at specific times over a certain period [21]. Ephemeris data, for example, could provide one with the estimated distance and velocity of another celestial body with respect to the Earth. This data is obtained through the application of orbital mechanics. For example, ephemeris data of the Sun with respect to the Earth is available simply because the knowledge of Earth's orbit about the Sun is known to a high level throughout the year.

Similarly, ephemeris data of a particular orbit may exist with respect to a celestial body. For an Earth orbiting satellite, for example, ephemeris data would simply be the position and velocity of the satellite with respect to Earth's center—common knowledge based on the orbital elements. By establishing ephemeris data of celestial bodies such as the Moon and Sun as well as of the LRO orbit, all with respect to the ECI frame, coordinate transformations can be accomplished which allow one to compare data (such as pointing vectors) in the same frame. To illustrate the concept, the LRO mission operations team may want to know the angle between any given instrument and the Sun to avoid saturation of the instrument. If the direction of the instrument boresight and the pointing vector to the Sun are both known in the ECI frame, the angle between the Sun and instrument can be calculated using vector

math concepts, as discussed in the previous chapter. Example ephemeris data used by the LRO team that identifies the position and velocity of the LRO orbit with respect to ECI is shown in Figure 5.1. Note that in this data set, position and velocity are being updated every minute.

Date-hh:mm:ss	x (km)	y (km)	z (km)	vx (km/s)	vy (km/s)	vz (km/s)
A.D. 2017-Oct-30 00:00:00.0000	1.20E+08	8.91E+07	-2.94E+04	-1.75E+01	2.42E+01	-1.64E+00
A.D. 2017-Oct-30 00:01:00.0000	1.20E+08	8.91E+07	-2.95E+04	-1.75E+01	2.41E+01	-1.61E+00
A.D. 2017-Oct-30 00:02:00.0000	1.20E+08	8.91E+07	-2.96E+04	-1.74E+01	2.40E+01	-1.57E+00
A.D. 2017-Oct-30 00:03:00.0000	1.20E+08	8.91E+07	-2.97E+04	-1.74E+01	2.39E+01	-1.52E+00
A.D. 2017-Oct-30 00:04:00.0000	1.20E+08	8.91E+07	-2.98E+04	-1.74E+01	2.39E+01	-1.48E+00
A.D. 2017-Oct-30 00:05:00.0000	1.20E+08	8.91E+07	-2.99E+04	-1.73E+01	2.38E+01	-1.42E+00
A.D. 2017-Oct-30 00:06:00.0000	1.20E+08	8.91E+07	-3.00E+04	-1.73E+01	2.37E+01	-1.36E+00
A.D. 2017-Oct-30 00:07:00.0000	1.20E+08	8.91E+07	-3.01E+04	-1.72E+01	2.37E+01	-1.30E+00
A.D. 2017-Oct-30 00:08:00.0000	1.20E+08	8.91E+07	-3.01E+04	-1.72E+01	2.36E+01	-1.24E+00
A.D. 2017-Oct-30 00:09:00.0000	1.20E+08	8.91E+07	-3.02E+04	-1.72E+01	2.36E+01	-1.17E+00
A.D. 2017-Oct-30 00:10:00.0000	1.20E+08	8.91E+07	-3.03E+04	-1.72E+01	2.35E+01	-1.09E+00
A.D. 2017-Oct-30 00:11:00.0000	1.20E+08	8.91E+07	-3.03E+04	-1.71E+01	2.35E+01	-1.02E+00
A.D. 2017-Oct-30 00:12:00.0000	1.20E+08	8.91E+07	-3.04E+04	-1.71E+01	2.34E+01	-9.37E-01
A.D. 2017-Oct-30 00:13:00.0000	1.20E+08	8.91E+07	-3.05E+04	-1.71E+01	2.34E+01	-8.56E-01
A.D. 2017-Oct-30 00:14:00.0000	1.20E+08	8.91E+07	-3.05E+04	-1.71E+01	2.34E+01	-7.71E-01
A.D. 2017-Oct-30 00:15:00.0000	1.20E+08	8.91E+07	-3.06E+04	-1.70E+01	2.33E+01	-6.85E-01
A.D. 2017-Oct-30 00:16:00.0000	1.20E+08	8.91E+07	-3.06E+04	-1.70E+01	2.33E+01	-5.97E-01
A.D. 2017-Oct-30 00:17:00.0000	1.20E+08	8.91E+07	-3.06E+04	-1.70E+01	2.33E+01	-5.07E-01
A.D. 2017-Oct-30 00:18:00.0000	1.20E+08	8.91E+07	-3.06E+04	-1.70E+01	2.33E+01	-4.17E-01
A.D. 2017-Oct-30 00:19:00.0000	1.20E+08	8.91E+07	-3.07E+04	-1.70E+01	2.33E+01	-3.25E-01
A.D. 2017-Oct-30 00:20:00.0000	1.20E+08	8.91E+07	-3.07E+04	-1.70E+01	2.33E+01	-2.33E-01
A.D. 2017-Oct-30 00:21:00.0000	1.20E+08	8.91E+07	-3.07E+04	-1.70E+01	2.33E+01	-1.41E-01
A.D. 2017-Oct-30 00:22:00.0000	1.20E+08	8.91E+07	-3.07E+04	-1.70E+01	2.33E+01	-4.85E-02
A.D. 2017-Oct-30 00:23:00.0000	1.20E+08	8.91E+07	-3.07E+04	-1.70E+01	2.33E+01	4.34E-02
A.D. 2017-Oct-30 00:24:00.0000	1.20E+08	8.91E+07	-3.07E+04	-1.70E+01	2.33E+01	1.35E-01
A.D. 2017-Oct-30 00:25:00.0000	1.20E+08	8.91E+07	-3.07E+04	-1.70E+01	2.33E+01	2.25E-01
A.D. 2017-Oct-30 00:26:00.0000	1.20E+08	8.91E+07	-3.07E+04	-1.70E+01	2.33E+01	3.14E-01
A.D. 2017-Oct-30 00:27:00.0000	1.20E+08	8.91E+07	-3.07E+04	-1.70E+01	2.33E+01	4.01E-01

Figure 5.1. Ephemeris data of LRO orbit with respect to ECI. Adapted from [22].

Establishing the ephemeris data of the Moon, Sun, and orbit of the LRO with respect to the Earth also allows one to use vectors to define the position and velocity of any of these with respect to the other. If one were to know the position and velocity of the Moon with respect to Earth along with the position and velocity of the Sun with respect to Earth, one can simply use vector addition or subtraction to get the position and velocity of the Sun with respect to the Moon or vice versa. Let $\vec{r}_{ES}$ represent the pointing vector from the Earth to the Sun and $\vec{r}_{EM}$ represent the pointing vector from the Earth to the Moon. These two position vectors are known from the ephemeris data with Earth as the reference point. With these two pieces of information, the position (or pointing) vector of the Moon to the Sun can be calculated, as shown in (5.1) and (5.2). For clarity, a diagram of this example is also shown in Figure 5.2.

$$\vec{r}_{EM} + \vec{r}_{MS} = \vec{r}_{ES} \tag{5.1}$$

$$\vec{r}_{MS} = \vec{r}_{ES} - \vec{r}_{EM} \tag{5.2}$$

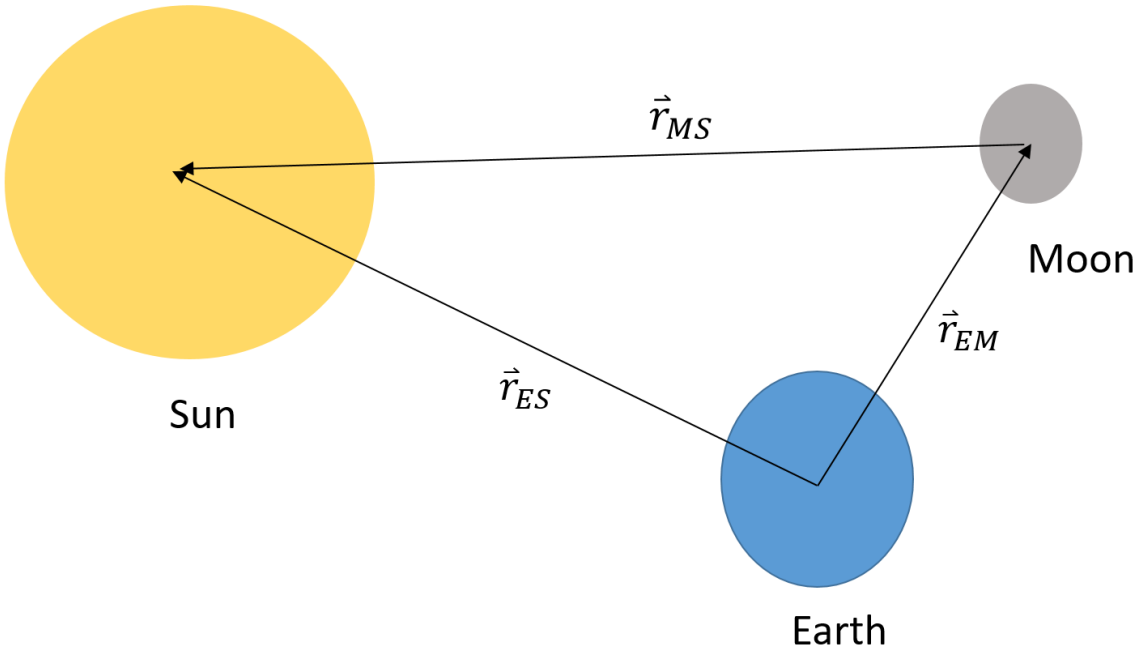

Figure 5.2. Locating objects using ephemeris data.

For LRO, coordinate transformation from ECI to OCS is calculated using the Lunar-centric spacecraft position unit vector $\hat{\mathbf{r}}$ and spacecraft velocity unit vector $\hat{\mathbf{v}}$. Both position and velocity vectors are Lunar centric and relative to the ECI frame. The rotation matrix from ECI to OCS $[A]_{OCS}^{ECI}$ is shown in (5.3) [9]. Similarly, the transpose can be taken to calculate the transformation matrix from OCS to ECI $[A]_{ECI}^{OCS}$, as shown in (5.4).

$$[A]_{OCS}^{ECI} = \begin{bmatrix} \frac{(-\hat{\mathbf{r}}\times\hat{\mathbf{v}})\times-\hat{\mathbf{r}}}{|(-\hat{\mathbf{r}}\times\hat{\mathbf{v}})\times-\hat{\mathbf{r}}|} \\ \\ \frac{-\hat{\mathbf{r}}\times\hat{\mathbf{v}}}{|-\hat{\mathbf{r}}\times\hat{\mathbf{v}}|} \\ \\ -\hat{\mathbf{r}} \end{bmatrix} \tag{5.3}$$

$$[A]_{ECI}^{OCS} = \left([A]_{OCS}^{ECI}\right)^T = \begin{bmatrix} \frac{(-\hat{\mathbf{r}}\times\hat{\mathbf{v}})\times-\hat{\mathbf{r}}}{|(-\hat{\mathbf{r}}\times\hat{\mathbf{v}})\times-\hat{\mathbf{r}}|} & \frac{-\hat{\mathbf{r}}\times\hat{\mathbf{v}}}{|-\hat{\mathbf{r}}\times\hat{\mathbf{v}}|} & -\hat{\mathbf{r}} \end{bmatrix} \tag{5.4}$$

Transformation from the OCS to the BCS is accomplished by a $1-2-3$ Euler rotation, where $[\phi, \theta, \psi]$ represent roll, pitch, and yaw, respectively, offset from nominal nadir pointing mode. The calculation is shown in (5.5), which was derived in [9].

$$[A]_{BCS}^{OCS} = [A_3(\psi)] \cdot [A_2(\theta)] \cdot [A_1(\varphi)] \tag{5.5}$$

where A_3, A_2, A_1 are the Euler rotations about the specified axis as defined in (5.6) [9].

$$\begin{aligned} [A_1(\phi)] &= \begin{bmatrix} 1 & 0 & 0 \\ 0 & \cos(\varphi) & \sin(\varphi) \\ 0 & -\sin(\varphi) & \cos(\varphi) \end{bmatrix} \\ [A_2(\theta)] &= \begin{bmatrix} \cos(\theta) & 0 & -\sin(\theta) \\ 0 & 1 & 0 \\ \sin(\theta) & 0 & \cos(\theta) \end{bmatrix} \\ [A_3(\psi)] &= \begin{bmatrix} \cos(\psi) & \sin(\psi) & 0 \\ -\sin(\psi) & \cos(\psi) & 0 \\ 0 & 0 & 1 \end{bmatrix} \end{aligned} \tag{5.6}$$

Since the boresights of the instruments or sensors are typically defined in the BCS frame and bright objects typically held fixed in an inertial frame for relatively short maneuver times, it may be advantageous to first transform the boresight vectors from the BCS to the OCS frame, as done in (5.5). Therefore, conversions between the three coordinate systems identified (ECI, OCS, and BCS) are required. The mathematical relationship is shown in

(5.7) [9]; this is an extremely useful tool when one would like to compare two separate pointing vectors in a common reference frame.

$$[A]_{BCS}^{ECI} = [A]_{BCS}^{OCS} \cdot [A]_{OCS}^{ECI} \tag{5.7}$$

5.2 The Addition of Bright Object Avoidance Operational Constraints

For targeting operations, operational constraints may impact the total slew time required to reach the target as well as the trajectory taken. One common constraint which impacts both of these is bright object avoidance which is discussed below.

5.2.1 Attitude Constraints

A schematic for constructing a canonical bright-object constraint is given in Figure 5.3. In Figure 5.3, unit vector $\hat{\mathbf{b}}^b$ denotes the orientation of the bore-sight of a light-sensitive instrument with respect to the satellite body-fixed frame. Unit vector $\hat{\mathbf{c}}^N$ denotes the location of a bright celestial body, such as the Sun, referenced to an inertial frame, N.

In order to construct an appropriate avoidance constraint, it is necessary to express $\hat{\mathbf{b}}^b$ and $\hat{\mathbf{c}}^N$ in the same frame. If it is desired to work in the inertial reference frame, the following transformation matrix (given in terms of quaternions) may be used to determine $\hat{\mathbf{b}}^N$ [23]. For notation purposes, the inertial frame (N) used from this point forward is taken as the ECI frame and the notation (b) is used as shorthand for the BCS frame.

$$C_b^N(\mathbf{q}) = \begin{bmatrix} q_1^2 - q_2^2 - q_3^2 + q_4^2 & 2(q_1q_2 - q_3q_4) & 2(q_1q_3 + q_2q_4) \\ 2(q_1q_2 + q_3q_4) & -q_1^2 + q_2^2 - q_3^2 + q_4^2 & 2(q_2q_3 - q_1q_4) \\ 2(q_1q_3 - q_2q_4) & 2(q_2q_3 + q_1q_4) & -q1^2 - q_2^2 + q_3^2 + q_4^2 \end{bmatrix} \tag{5.8}$$

In (5.8) the notation, C_b^N, is taken to imply a transformation of a vector from frame b to frame N.

If during an attitude maneuver, it is desired to maintain the bright object outside of the bore-sight cone having half-angle, θ, as in Figure 5.3, then the following constraint must be

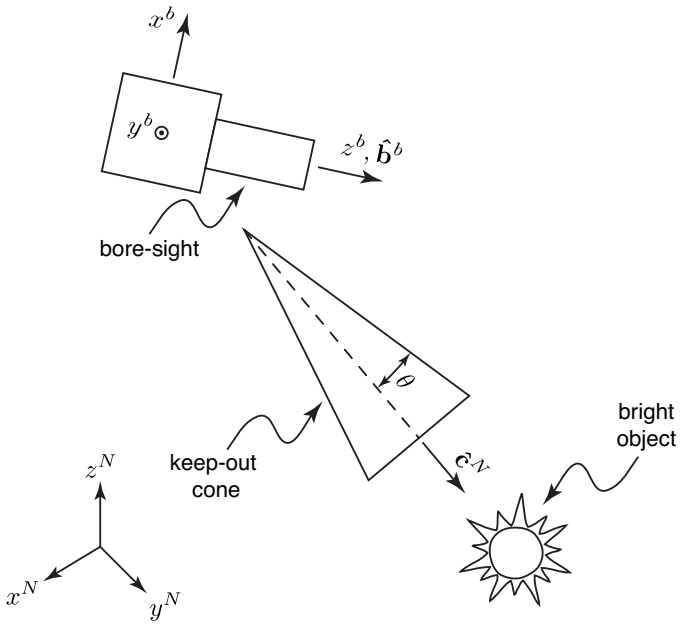

Figure 5.3. Schematic of bright-object avoidance.

satisfied at all times

$$\left[C_b^N(\mathbf{q})\hat{\mathbf{b}}^b\right]^T \hat{\mathbf{c}} \leq \cos(\theta) \tag{5.9}$$

An attitude maneuver that satisfies the constraint given by (5.9), is typically solved through use of a dog-leg maneuver, which consists of two or more separate eigenaxis rotations in order to avoid the target. It can also be developed by solving an optimal spacecraft reorientation problem wherein the inequality (5.9) is formulated as a nonlinear path constraint. The state of practice dog-leg maneuver and an appropriate optimal control problem formulation are both provided in the next chapter.

5.3 Summary

For instrument or sensor Sun avoidance, a boresight pointing vector that is typically defined in the body frame must be compared against a Sun pointing vector, which is typically defined in an inertial frame. Through the use of ephemeris data and coordinate transformation equations, one can compare any desired pointing vectors in any single frame that is desired. Oftentimes, one frame of reference may prove to be more useful than others in that sometimes simplifying assumptions can be made. For example, the Sun's position vector with respect

to the spacecraft body changes much more slowly over time in the ECI frame than in the OCS. By careful choice of the frame to view the problem in, a maneuver which may be on the order of minutes could likely keep the Sun pointing vector constant if utilizing the inertial frame, whereas this would not be a realistic assumption if referencing the OCS as orbital position will change relatively largely in that time span. These selections could prove to simplify an otherwise complex problem.

THIS PAGE INTENTIONALLY LEFT BLANK

CHAPTER 6:
Applying Optimal Control Theory to Targeting Operations

In this chapter, a background of solution techniques for solving constrained attitude maneuvers is explored. Ultimately, an optimal control problem formulation for a generic satellite will be developed and solved. Linear and nonlinear path constraints will be placed on both the control and state of the system to develop a maneuver trajectory. Emphasis will be placed on the mathematical representation of the path constraints and problem solution validation and verification. Optimality tests will be explained and verified. The concept of scaling and balancing, specifically when considering path constraints, is discussed and emphasized. Finally, a comparison is made between the minimum time solution and a typically used dog-leg maneuver. The optimal control concept can be used to automate maneuver design with bright object avoidance.

6.1 Introduction

Attitude maneuver planning is a critical aspect of satellite operations. In many cases the conventional eigenaxis maneuver [24] suffices. However, in some instances delicate instruments or optical sensors could be exposed to bright objects if an Eigenaxis maneuver is executed. Similarly, it may be necessary to ensure that the requirements on power generation or thermal loading are met during attitude maneuvers. Occasionally, performing an Eigenaxis maneuver may violate such requirements. Thus, a means for planning constrained attitude maneuvers may be required to support the day-to-day operation of a particular satellite mission. If constraint violations occur infrequently, it may be possible to develop workarounds in an ad-hoc or cut-and-try fashion. On the other hand, when constraint violations occur frequently, an automated approach may become desirable.

While a great deal of work has been done on maneuver planning in the absence of attitude constraints since the 1980s, the literature on maneuver planning in the presence of attitude constraints is more recent. A sampling of some of the early papers in this area include the work of Hablani [25], Mengali and Quarta [26], and Kim et. al [27]. In these works, the goal

was to determine so-called *feasible* solutions to the constrained reorientation problem. The notion of feasibility implies that the maneuver solution meets all of the specified constraints, e.g. point-wise constraints on the attitude keep-out zones and/or attitude dynamics, but without specific regard to maneuver time, power, or fuel requirements. More recent work on how to find feasible solutions to the constrained attitude planning problem includes the work of Kjellberg and Lightsey [28], [29], Biggs and Colley [30], and Tanygin [31].

Kjellberg and Lightsey [28] employed an A^* path-finding algorithm to find admissible paths between keep-out zones by developing a quaternion trajectory over a discretized shell of unit radius. The authors extended their work in [29] to handle keep-out/keep-in zones for multiple reference vectors in the satellite body frame. Biggs and Colley [30] define analytic paths on $SO(3)$ defined in terms of free parameters that can be adjusted to match boundary conditions and reshape a path in order to avoid forbidden regions. In instances where no single curve can be found that avoids the keep-out zone, a multi-curve (n-leg) maneuver is constructed. An approach for finding kinematically feasible n-leg maneuvers is also presented in reference [6]. In reference [31], Tanygin constructs a grid in a special minimum-distortion projected space by discretizing the attitude sphere and applies enumerated and graph search algorithms to find shortest constrained paths between target grid points. Because the above approaches are kinematic "pathfinding" methods, it is necessary to verify that the proposed attitude trajectories can indeed be implemented by the spacecraft attitude control system. These *a posteriori* checks can be done by simulating the spacecraft attitude control system or by inverting the spacecraft dynamics. If the *a posteriori* check fails, it may be necessary to iterate the maneuver planning step.

Attitude maneuver planning in the presence of attitude constraints can also be formulated as a nonlinear optimal control problem. In this framework, the spacecraft dynamical equations are considered as an integral part of the maneuver planning process, largely obviating the need for *a posteriori* checks on dynamic feasibility. In addition to the usual dynamic constraints associated with the spacecraft reorientation problem (e.g. the quaternion differential equations and/or Euler's equations), additional constraints on the orientation of the spacecraft must also be considered as part of the optimal control problem. Such constraints are generally of the form [27]

$$f\left(\mathbf{q}(t)\right) \leq \Phi_0 \quad \forall t \in [t_a, t_b] \tag{6.1}$$

or

$$\int_{t_a}^{t_b} g\left(\mathbf{q}(t)\right) dt \leq \Phi_1 \tag{6.2}$$

where f and g are appropriately defined functions of the attitude variables, Φ_0 and Φ_1 are constants, and $[t_a, t_b] \subseteq [t_0, t_f]$ with t_0 and t_f the maneuver begin and end times, respectively. Note that (6.1) is analogous to (5.9) in the previous chapter.

Kim et. al. [27] further differentiate the constraints given by (6.1) and (6.2) into a number of types. For example, the authors define a static attitude constraint as one in which a keep-out (or keep-in) zone is defined by a celestial body that is stationary with respect to an inertial frame during the time horizon of a given maneuver. In this case, the inertial unit vector describing the instrument/sensor boresight, $\hat{\mathbf{b}}(t)$, varies with time due to the attitude motion of the satellite. The inertial unit vector to the celestial object, $\hat{\mathbf{c}}$, on the other hand, is fixed in time. Such a static constraint may be cast in terms of the following scalar inequality: $\hat{\mathbf{b}}(t)^T\hat{\mathbf{c}} \leq \cos(\theta)$, where θ is the half-angle of the keep-out cone. The inequality is reversed for a keep-in constraint. Dynamic avoidance constraints [27] where $\hat{\mathbf{c}}(t)$ is time-varying are also possible and can arise when the source of the attitude constraint is actively controlled, e.g. spacecraft in a formation. In either case, due to the dependence of at least $\hat{\mathbf{b}}(t)$ on time over the horizon of the maneuver, the attitude constraints must be formulated in terms of path constraints in optimal control.

Solutions for constrained spacecraft reorientation maneuvers as a nonlinear optimal control problem has been studied by several authors including Xiaojun et. al [32] and Melton [33]. In references [32] and [33], pseudospectral methods were utilized in a hybrid approach. A kinematically feasible path is first generated using search trees, particle swarms, or other evolutionary strategies. The result of the first stage is then used as a guess and refined by the pseudospectral optimizer. Spiller et. al [34] also developed an approach based on particle swarm optimization to obtain near-optimal solutions to the constrained maneuver planning problem. One aspect that is largely missing from this body of work is the analysis of the necessary conditions for optimality, in particular those pertaining to the path constraints.

Solving nonlinear optimal control problems with path constraints has long been challenging [35]. For satellite attitude planning, in particular, a further complication arises because the control variable does not appear explicitly in the constraint equation. Thus, attitude constraints are state constraints of order ≥ 1. That is, it is necessary to take at least the first-

order time derivative of (6.1) or (6.2) to obtain an equation in which the control variables, **u**, appear. Because of this, it is quite possible (though not guaranteed) that the covector trajectories associated with the path constraints have impulsive trajectories [35], which can be challenging to solve numerically. The possibility of such jump conditions were identified by Pontryagin and his co-workers in the development of the minimum principle [36]. Because of such challenges, solutions based on nonlinear optimal control theory are normally considered difficult to obtain [33] and may be dismissed as a practical approach for autonomous attitude maneuver planning.

In this thesis, guess-free pseudospectral optimal control theory [37] will be applied towards the autonomous planning of constrained attitude maneuvers. Guess-free pseudospectral optimal control solutions eliminate the need for a hybrid approach wherein a rough solution must first be generated before the optimal control problem can be solved. The constrained attitude maneuver planning problems presented and solved throughout this thesis are solved using DIDO, a MATLAB toolbox based on pseudospectral optimal control theory for solving optimal control problems [35]. DIDO implements the guess-free algorithm described in [38] and additionally provides dual variables that can be utilized to check the necessary conditions via the covector mapping theorem discussed in [37] and the references therein. Guess-free solutions to the spacecraft reorientation problem in the absence of attitude constraints have already been successfully ground tested [39] and flight implemented on NASA spacecraft, such as the International Space Station [40], the Transition Region, and the Coronal Explorer [41]. Thus, it is logical to extend the flight proven approach to include operational scenarios that include attitude constraints.

In this chapter, control of a typical reaction wheel satellite is considered in the presence of one or more operational constraints on the satellite attitude. Particular attention is paid to the formulation and analysis of the relevant optimal control problems. The optimality of the solutions will be verified by validating the numerical results against the necessary conditions for optimality. Since solutions may admit impulsive path covectors, particular attention is paid to analyzing the nature of the path constraints obtained from the computations. Results for a kinematics only solution which account for the dynamics of the spacecraft is presented in this chapter.

6.2 Optimal Control Theory

As discussed, optimal control theory is one method to solve for a trajectory planning problem, even with the addition of nonlinear attitude path constraints. From [35] "a standard optimal control problem can be defined in terms of finding a dynamically feasible state-control function pair, $\{\mathbf{x}(\cdot), \mathbf{u}(\cdot)\}$, that transfers the state of the system, $\mathbf{x} \in \mathbb{R}^{N_x}$, from a given initial condition, $\mathbf{x}(t_0)$, to a target condition, $\mathbf{e}(\mathbf{x}_f, \mathbf{t}_f) = \mathbf{0}$, while minimizing a given cost functional, J." A standard optimal control problem takes on the following form, displayed as Problem A.

$$A : \begin{cases} \text{Minimize} & J[\mathbf{x}(\cdot), \mathbf{u}(\cdot), t_f] &= E(\mathbf{x}(t_f), t_f) + \int_{t_0}^{t_f} F(\mathbf{x}(t), \mathbf{u}(t), t)dt \\ \text{Subject to} & \dot{\mathbf{x}}(t) &= \mathbf{f}(\mathbf{x}(t), \mathbf{u}(t), t) \\ & \mathbf{x}(t_0) &= \mathbf{x}^0 \\ & t_0 &= t^0 \\ & \mathbf{e}(\mathbf{x}_f, t_f) &= \mathbf{0} \end{cases} \tag{6.3}$$

In this form, E is referred to as the endpoint cost, e is the endpoint constraint, F is the running cost, and the dynamics of the system are represented by $\dot{\mathbf{x}}(t)$, which is written in state space form and is a function of the defined states and controls of the system [35]. The cost functional for a typical minimum time maneuver is $J[\mathbf{x}(\cdot), \mathbf{u}(\cdot), t_f] = t_f$ where $E = t_f$ and $F = 0$. Additionally, path constraints can be added to the problem formulation. These path constraints will be identified using h_i and can be a function of state and/or control of the system.

Within this framework it is necessary to identify what is desired to be minimized, which is accomplished by defining the cost functional. Then, the dynamics of the system must be represented in state space form. Any known or desired initial and final states are placed in the problem formulation as endpoint conditions. Finally, any path constraints will be mathematically represented. Once these items are in place, Pontryagin's Principle may be applied, as will be shown throughout the rest of the thesis. As previously mentioned, however, it is necessary to represent the dynamics of the spacecraft and identify the path constraints in the problem formulation. Recall the kinematics model was developed in (4.10) and (4.11) and the bright object constraint was discussed in (5.9) and (6.1).

6.3 Autonomous Maneuver Planning for a Single Avoidance Cone

In this chapter, we are interested in determining time-optimal maneuvers with attitude constraints. This objective is carried out autonomously by solving an optimal control problem. In its simplest form, the minimum-time optimal control problem can be written as

$$P: \begin{cases} \text{Minimize} & J[\mathbf{x}(\cdot), \mathbf{u}(\cdot), t_f] = t_f \\ \\ \text{Subject to} & \dot{\mathbf{q}} = \mathbf{Q}(\boldsymbol{\omega})\mathbf{q} \\ & \boldsymbol{\omega} = \mathbf{u} \\ & \mathbf{q}(t_0) = \mathbf{q}^0 \\ & \mathbf{q}(t_f) = \mathbf{q}^f \\ & \hbar_1(t) \triangleq u_1^2 + u_2^2 + u_3^2 \leq u_{\max}^2 \\ & \hbar_2(t) \triangleq \left[C_b^N(\mathbf{q}(t))\hat{\mathbf{b}}^b\right]^T \hat{\mathbf{c}}^N \leq \cos(\theta) \end{cases} \tag{6.4}$$

The attitude constrained minimum-time reorientation problem can be solved numerically to determine the state-control function pair, $t \rightarrow (\mathbf{q}, \boldsymbol{\omega})$ that allows the satellite to be reoriented between the specified initial and final attitudes, $\mathbf{q}(t_0)$ to $\mathbf{q}(t_f)$, in the minimum-time without violating the bright object constraint given by path function $\hbar_2(t)$. We note that $\mathbf{q}(t_0)$ or $\mathbf{q}(t_f)$ may be unknown if there is relative motion between the satellite and the target orientation. In this case, the associated end point function can be written in terms of pointing vector. The spherical constraint on the control variables, $\hbar_1(t)$, ensures that the commanded angular rate vector does not exceed the approximated capability of the satellite attitude control system. Since the solution to (6.4) does not provide a spacecraft body-torque vector, it is assumed that the trajectories of the attitude quaternions will be tracked by the feedback law of the satellite attitude control system (see Chapter 4). Constraint $\hbar_2(t)$ was defined using the definition of a dot product between the boresight and Sun pointing vectors, which is shown in (6.5), where **a** and **b** are selected to be any two vectors placed in the same frame. The Sun pointing and boresight vectors are unit vectors, thereby simplifying the dot product even further, as shown in (6.6). As discussed in Chapter 5, it is necessary to project both vectors into the same reference frame. In this example, the boresight vector was transformed to the

inertial frame via the rotation matrix C_b^N ((5.8)) since the bright object was already defined in the inertial frame. For this problem, the bright object pointing vector was assumed to stay constant with time, a modest assumption given the low maneuver time relative to the movement of the Sun with respect to the ECI frame.

$$\mathbf{a} \cdot \mathbf{b} = |\mathbf{a}||\mathbf{b}| \cos\theta \tag{6.5}$$

$$\mathbf{a} \cdot \mathbf{b} = \cos\theta \tag{6.6}$$

Problem (6.4) will now be solved to demonstrate a typical solution to the constrained attitude maneuvering problem. Reaction wheel specifications, $\mathbf{Z}$, and $\mathbf{I}$ are assigned to be generic (but realistic) values of a small satellite and defined in (6.7) and (6.8). Values for LRO will be substituted later, when a specific case is studied. In this example, the objective is to perform a large (135-deg) negative rotation about the satellite pitch axis, from $\mathbf{q}^0 = [0, 0, 0, 1]^T$ to $\mathbf{q}^f = [0, -0.9239, 0, 0.3827]^T$. The maximum spacecraft rate is elected as $\omega_{\max} = 1.0$-deg/sec. An attitude keep-out cone with a 30-deg half-angle is aligned with the satellite $+z$-body axis, i.e. $\hat{\mathbf{b}}^b = [0, 0, 1]^T$. The unit-vector to the bright object; e.g. Sun, Moon, or the Earth, is given by $\hat{\mathbf{c}}^N = [-1, 0, 0]^T$. The geometry of the scenario is shown in Figure 6.1. Clearly, an Eigenaxis maneuver about the Euler axis $\hat{\mathbf{e}} = [0, -1, 0]^T$ would cause the satellite $+z$-body axis to violate the bright object constraint and so such a maneuver is operationally infeasible.

$$\mathbf{Z} = \begin{bmatrix} 0.8192 & 0.8192 & -0.8192 & -0.8192 \\ 0.4056 & -0.4056 & -0.4056 & -0.4056 \\ 0.4056 & 0.4056 & 0.4056 & 0.4056 \end{bmatrix} \tag{6.7}$$

$$\mathbf{I} = \begin{bmatrix} 712.5 & 0 & 0 \\ 0 & 949.5 & 0 \\ 0 & 0 & 871.5 \end{bmatrix} \text{kgm}^2 \tag{6.8}$$

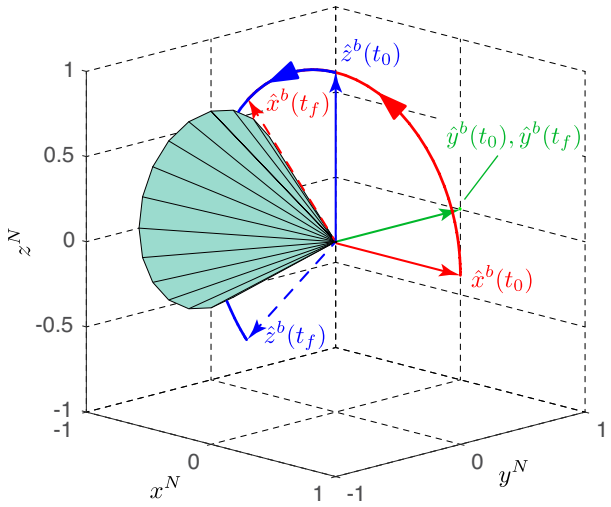

Figure 6.1. Eigenaxis maneuver violates a bright object constraint.

6.3.1 Development of the Necessary Conditions

Pontryagin's Principle is now applied to the problem formulation of (6.4) to develop the necessary conditions for optimality. A step-by-step description of the process is given in [35]. According to Pontryagin's Principle, the Hamiltonian must be minimized at each instant in time. From the definition of the Hamiltonian, shown in (6.9), the Hamiltonian may be constructed, noting that in this case $F = 0$. The adjoint covectors are represented by λ with a subscript indicative of its corresponding state. Due to the introduction of non-linear path constraints on the control and for bright object avoidance, the standard Karush-Kuhn-Tucker (KKT) conditions must be applied by developing the Lagrangian of the Hamiltonian, as in (6.10). The path KKT multipliers are represented by the symbol $\boldsymbol{\mu}$. The Lagrangian of the Hamiltonian for this problem is shown in (6.11).

$$H(\boldsymbol{\lambda}, \mathbf{x}, \mathbf{u}, t) = F + \lambda^T f(\mathbf{x}, \mathbf{u}) \tag{6.9}$$

$$\bar{H}(\boldsymbol{\mu}, \boldsymbol{\lambda}, \mathbf{x}, \mathbf{u}, t) = H(\boldsymbol{\lambda}, \mathbf{x}, \mathbf{u}, t) + \boldsymbol{\mu}^T \mathbf{h}(\mathbf{x}, \mathbf{u}, t) \tag{6.10}$$

$$\begin{aligned}\bar{H}(\boldsymbol{\mu}, \boldsymbol{\lambda}, \mathbf{x}, \mathbf{u}, t) = \frac{1}{2}\big[&\lambda_{q1}(q_4u_1 - q_3u_2 + q_2u_3) + \lambda_{q2}(q_3u_1 + q_4u_2 - q_1u_3) + \dots \\ &\lambda_{q3}(-q_2u_1 + q_1u_2 + q_4u_3) + \lambda_{q4}(-q_1u_1 - q_2u_2 - q_3u_3)\big]\dots \\ &+\mu_1(u_1^2 + u_2^2 + u_3^2) + \mu_2(\left[C_b^N(\mathbf{q}(t))\hat{\mathbf{b}}^b\right]^T \hat{\mathbf{c}})\end{aligned} \tag{6.11}$$

The Lagrangian of the Hamiltonian is minimized if it is stationary with respect to the control vector and the multiplier-constraint pair satisfies the complementarity condition. [35] The resulting necessary conditions can be grouped in terms of two KKT conditions; the stationary condition and the complementarity condition, which are defined in (6.12) and (6.13), respectively.

$$\frac{\partial \bar{H}}{\partial \mathbf{u}} = \mathbf{0} \tag{6.12}$$

$$\mu_i \begin{cases} \leq 0 \text{ if } \hbar_i = \hbar_i^{lower} \\ = 0 \text{ if } \hbar_i^{lower} < \hbar_i < \hbar_i^{upper} \\ \geq 0 \text{ if } \hbar_i = \hbar_i^{upper} \end{cases} \tag{6.13}$$

For Problem (6.4), there are two complementarity conditions which are defined in (6.14) and (6.15). In the formulation of the problem, there are technically no lower limits on the path constraints. However, based on $\hbar_1$ being calculated as a sum of squares and $\hbar_2$ being calculated from a dot product, the numerical values for the lower bounds could be expressed as 0 and -1, respectively. In this case, both path covectors will be a value of zero for all time in which the path constraint is not active and will become a positive value any time the path constraint is enforced.

$$\mu_1 \begin{cases} \leq 0 \; if \; \hbar_1 = 0 \\ = 0 \; if \; 0 < \hbar_1 < (1^\circ/s)^2 \\ \geq 0 \; if \; \hbar_1 = (1^\circ/s)^2 \end{cases} \tag{6.14}$$

$$\mu_2 \begin{cases} \leq 0 \; if \; \hbar_2 = -1 \\ = 0 \; if \; -1 < \hbar_2 < cos(30^\circ) \\ \geq 0 \; if \; \hbar_2 = cos(30^\circ) \end{cases} \tag{6.15}$$

The stationary condition gives the following:

$$\begin{aligned} \frac{\partial \bar{H}}{\partial u_1} &= \frac{1}{2}\left[\lambda_{q1}q_4 + \lambda_{q2}q_3 - \lambda_{q3}q_2 - \lambda_{q4}q_1\right] + 2\mu_1 u_1 = 0 \\ \frac{\partial \bar{H}}{\partial u_2} &= \frac{1}{2}\left[-\lambda_{q1}q_3 + \lambda_{q2}q_4 + \lambda_{q3}q_1 - \lambda_{q4}q_2\right] + 2\mu_1 u_2 = 0 \\ \frac{\partial \bar{H}}{\partial u_3} &= \frac{1}{2}\left[\lambda_{q1}q_2 - \lambda_{q2}q_1 + \lambda_{q3}q_4 - \lambda_{q4}q_3\right] + 2\mu_1 u_3 = 0 \end{aligned} \tag{6.16}$$

From the stationary condition, the controls can now be represented directly as a function of states, the adjoints, the path covectors, and time, as shown in (6.17) - (6.19). Because μ_1 appears in the denominator of the control equation, it is important to point out that $\mu_1 = 0$ at any point in time leads to an indeterminate control. From (6.14), μ_1 is only 0 if the control is not at its maximum allowable value. For a minimum time solution, in which angular velocity is the only control, the path constraint will always be activated. Thus, for this path problem, $\mu_1 > 0$ for the entire trajectory, leading to finite values for $u_i(t)$.

$$u_1(t) = -\frac{1}{4\mu_1}\left[\lambda_{q1}q_4 + \lambda_{q2}q_3 - \lambda_{q3}q_2 - \lambda_{q4}q_1\right] \tag{6.17}$$

$$u_2(t) = -\frac{1}{4\mu_1}\left[-\lambda_{q1}q_3 + \lambda_{q2}q_4 + \lambda_{q3}q_1 - \lambda_{q4}q_2\right] \tag{6.18}$$

$$u_3(t) = -\frac{1}{4\mu_1}\left[\lambda_{q1}q_2 - \lambda_{q2}q_1 + \lambda_{q3}q_4 - \lambda_{q4}q_3\right] \tag{6.19}$$

Next, the adjoint equations are derived using (6.20). Of note, the resulting equations are complicated equations and are not useful for verification of the numerical solution. The adjoint equations are shown in (6.21)-(6.24). It should also be noted that the path constraint on the attitude of the spacecraft ($\hbar_2$) must be accounted for in the adjoint equations. Recall **b** and **c** are in reference to the boresight and Sun pointing vectors described earlier. Because

each were defined along a single axis, i.e. $\hat{b}^b = [0, 0, 1]$ and $\hat{c}^N = [-1, 0, 0]$, many of the terms drop out.

$$\frac{\partial \bar{H}}{\partial \mathbf{x}} = \frac{\partial H}{\partial \mathbf{x}} + \left(\frac{\partial \mathbf{h}}{\partial \mathbf{x}}\right)^T \boldsymbol{\mu} = -\dot{\boldsymbol{\lambda}}_x \tag{6.20}$$

$$\dot{\lambda}_{q1} = \frac{1}{2}\big[\lambda_{q2}u_3 - \lambda_{q3}u_2 + \lambda_{q4}u_1\big] - 2q_3\mu_2 \tag{6.21}$$

$$\dot{\lambda}_{q2} = \frac{1}{2}\big[-\lambda_{q1}u_3 + \lambda_{q3}u_1 + \lambda_{q4}u_2\big] - 2q_4\mu_2 \tag{6.22}$$

$$\dot{\lambda}_{q3} = \frac{1}{2}\big[\lambda_{q1}u_2 - \lambda_{q2}u_1 + \lambda_{q4}u_3\big] - 2q_1\mu_2 \tag{6.23}$$

$$\dot{\lambda}_{q4} = \frac{1}{2}\big[-\lambda_{q1}u_1 - \lambda_{q2}u_2 - \lambda_{q3}u_3\big] - 2q_2\mu_2 \tag{6.24}$$

Finally, the terminal transversality conditions are evaluated by constructing the endpoint Lagrangian. The equations are given in (6.25) - (6.27), where E is endpoint cost (defined in the cost function) and e are the endpoint functions for desired end states.

$$\lambda(t_f) = \frac{\partial \bar{E}}{\partial x_f} \tag{6.25}$$

$$\bar{E} = E + \nu^T e \tag{6.26}$$

$$\bar{E} = tf + \nu_1[q_1(t_f) - q_1^f] + \nu_2[q_2(t_f) - q_2^f] + \nu_3[q_3(t_f) - q_3^f] + \nu_4[q_4(t_f) - q_4^f] \tag{6.27}$$

In (6.27), ν is the endpoint covector and superscript f denotes the final desired values. Because the ν values are unknown in this case, these variables are not useful for verification of the numerical solution.

The minimum-time maneuver plan determined by solving (6.4) was obtained using DIDO.

The results are shown in Figure 6.2 and Table 6.1. Prior to declaring the results of Figure 6.2 as a valid extremal solution. The term extremal solution refers to the fact that no other solution may exist for the problem formulation. This being said, it is important to verify the feasibility and optimality of the candidate solution.

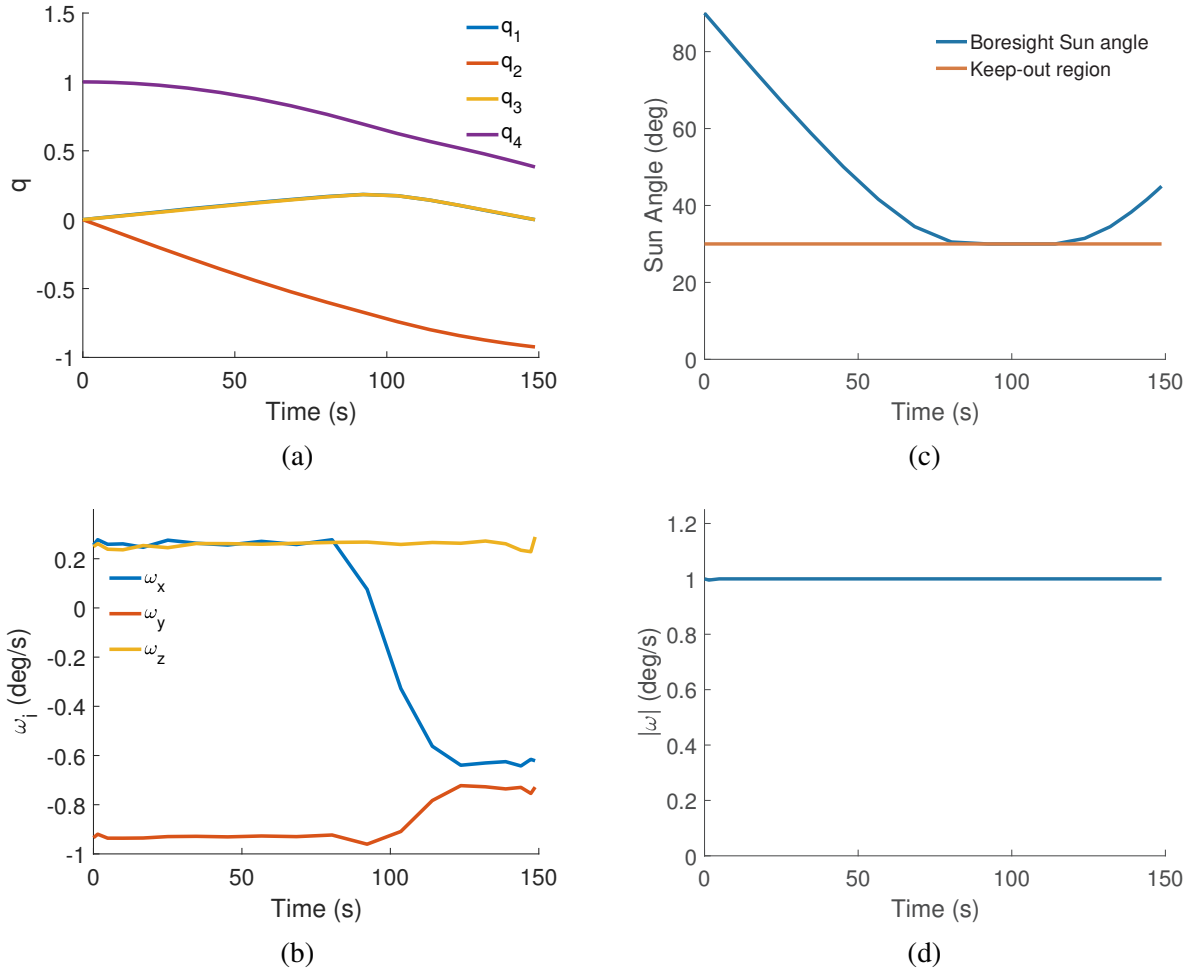

Figure 6.2. Candidate solution to a minimum time constrained reorientation problem for a 135-deg pitch: (a) quaternions; (b) angular velocity; (c) boresight to Sun angle; (d) angular velocity magnitude.

6.3.2 Feasibility Check

To test the feasibility of the time optimal solution, the optimal control trajectories were used to drive plant dynamics, as described in [35]. The optimal solution and actual

Table 6.1. Desired and achieved quaternion values.

	Desired	Actual
$q_1(t_f)$	0	3.39×10^{-14}
$q_2(t_f)$	-0.9239	-0.9239
$q_3(t_f)$	0	1.35×10^{-14}
$q_4(t_f)$	0.3827	0.3827

propagated system response for the given optimal control input were plotted on the same graph to facilitate a visual check. This test ensures that the state solution obtained from solving the optimal control problem matches the state trajectory that is obtained when the control solution is used to control the dynamics model. If these two time histories were different from one another, it would indicate that the optimal control solution does not contain sufficient resolution to properly drive the system and is therefore infeasible for implementation. The result of the feasibility check is shown in Figure 6.3. It was determined that the candidate solution of Figure 6.2 passed the feasibility check, since the numerical optimal solution (discrete points) lays on the same path as the actual system response. The terminal errors were on the order of 1×10^{-4}.

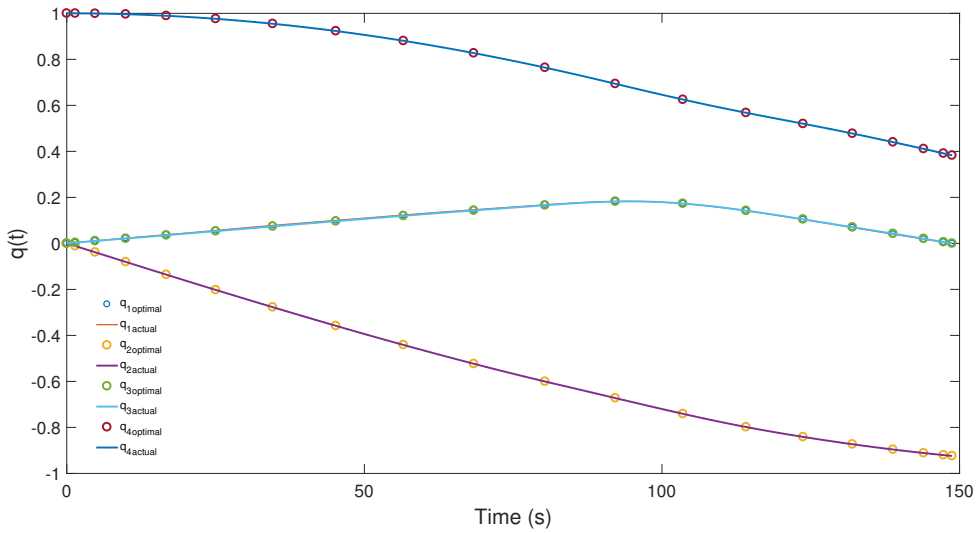

Figure 6.3. Feasibility verification for the optimal time maneuver.

6.3.3 Optimality Checks

The optimality of the candidate solution may be tested by examining the time histories of the Hamiltonian and of the complementarity conditions. For a time-optimal solution, the Hamiltonian should be a nominally constant value of -1 [35]. The Hamiltonian time history is shown in Figure 6.4a. In order to characterize H(t), the mean value and deviation over the maneuver were calculated as $\mu_H = -0.8252$ and $\sigma_H = 0.1197$. Clearly, the Hamiltonian deviates somewhat from the expected value of -1. In order to explore the reason for this discrepancy, the other dual variables can be checked. To this end, Figure 6.4 also shows the time histories of the quaternion costates, path constraints, and the associated path covectors.

The path constraints were plotted against their corresponding path covectors in Figure 6.4. The complementarity conditions, from (6.14) and (6.15), were evaluated. The path constraint associated with magnitude of angular velocity was always at its upper limit, which is logical given that this is a minimum time problem. Per the KKT conditions, $\mu_1 \geq 0$ is expected and was obtained in the numerical results. The path constraint on the Sun angle, however, does not pass the optimality check. This can be seen by examining Figure 6.4d and observing that μ_2 took on a value greater than 0 prior to the activation of the path constraint, thereby violating (6.15). The large magnitude values of λ_{q2} and λ_{q4} compared to their corresponding state ranges of -1 to 1 is also a concern because it indicates poor scaling. Given the results of Figure 6.4, it appears that the solutions of Figure 6.2 may not solve the intended problem.

It may be noted from Figures 6.4b and 6.4d that an order of magnitude difference exists between the path constraints and their associated covectors. Specifically, there are 6 orders of magnitude difference between $\hbar_1$ and μ_1. Although this large difference did not seem to impact obtaining a dynamically feasible solution, further analysis was carried out to determine if scaling and balancing the optimal control problem could improve matters.

6.3.4 Scaling and Balancing the Path Constraints

The first path constraint was scaled in an effort to ameliorate the magnitude difference between the $\hbar_1$ and μ_1. The selected scaling units are shown in (6.28), where $\hbar$ denotes the scaled path constraint. It should be noted that based on the previous results q_2 and q_4 could have also been scaled in an attempt to change the magnitude of the corresponding adjoints,

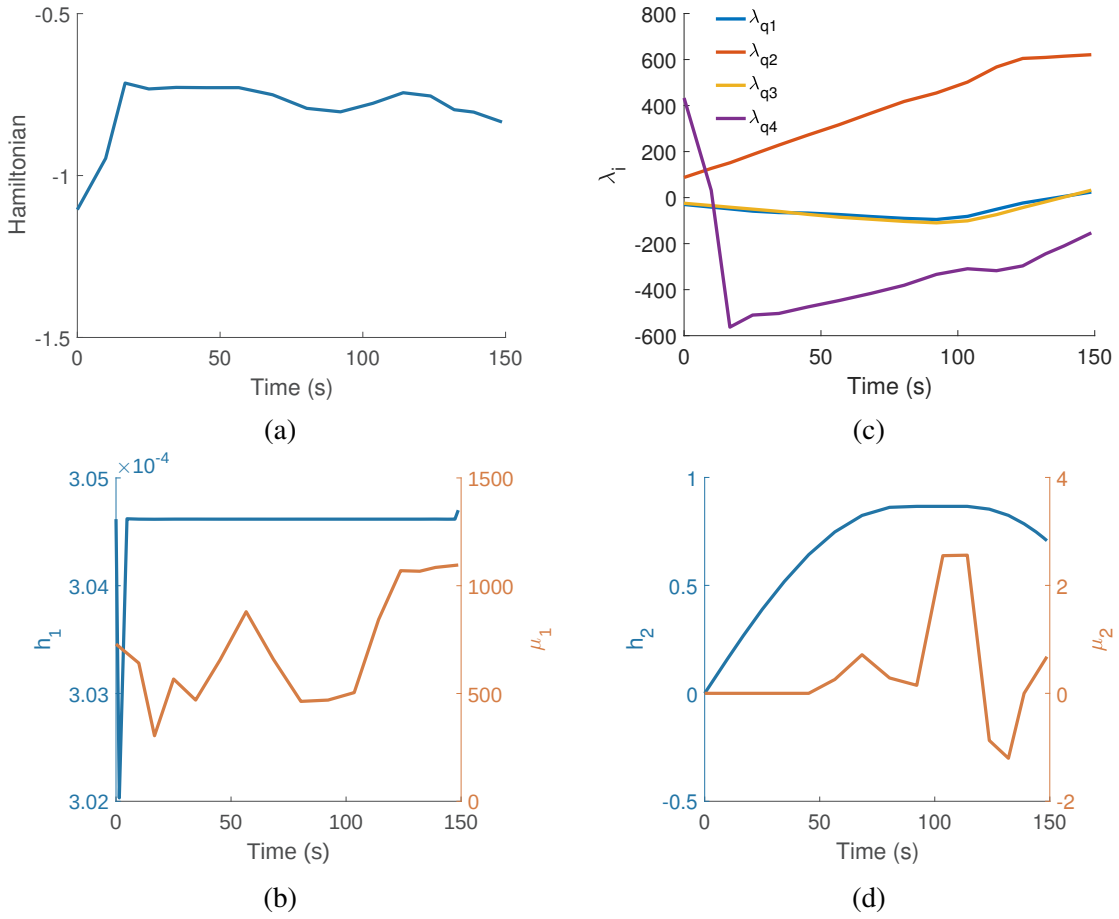

Figure 6.4. Optimization validation checks for candidate solution: (a) Hamiltonian; (b) path constraint 1; (c) costates; (d) path constraint 2.

which displayed a wide range of values (depicted in Figure 6.4c). This being said, the overwhelming difference in magnitude between the h_1 and μ_1 led to the decision to initially scale this path constraint and then follow up with any further scaling changes to q_i and λ_i if still required. Due to the inverse relationship between the primal and dual space [42], choosing $H_i U < 1$ would reduce the magnitude difference between $\hbar_1$ and μ_1.

In this case, selecting $H_1 U = 0.1$ results in the factor between h_1 and μ_1 dropping to about 55 thousand. Therefore, scaling was modified to $H_1 U = 0.01$ to further drive them together, resulting in a factor of between $\hbar_1$ and μ_1 of 550. Because the balancing was getting much better, the third and final revision was as shown in (6.28).

Numerical results obtained after scaling the two path constraints are shown in Figure 6.5.

$$\bar{h}_1 = \frac{h_1}{H_1 U}, \; H_1 U = 0.005 \tag{6.28}$$

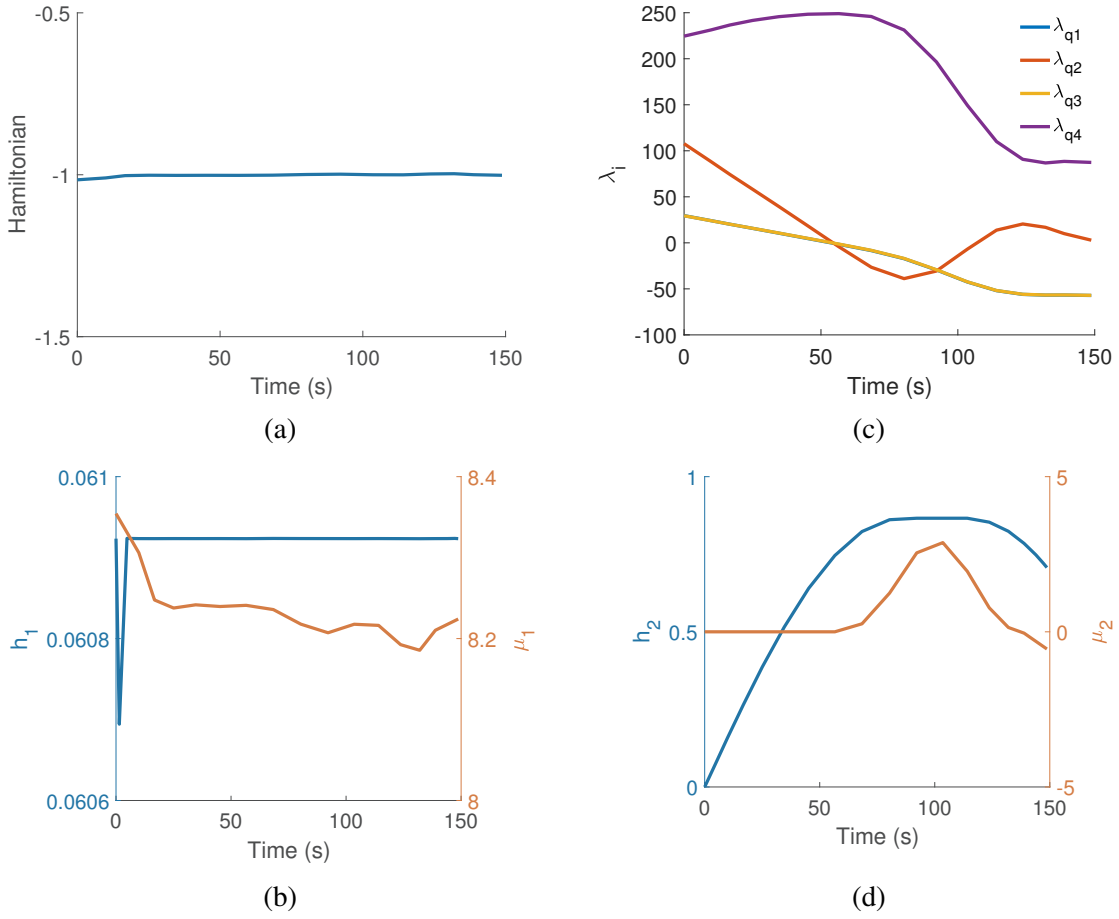

Figure 6.5. Necessary condition checks for numerical solution with scaled path constraint: (a) Hamiltonian; (b) scaled path constraint 1; (c) costates; (d) path constraint 2.

It was observed that the magnitude difference between $\hbar_1$ and μ_1 could be reduced by over 4 orders of magnitude from 3.4 million to about 130 by scaling the path constraint. The time history of μ_1 is now smoother, indicating that scaling the path constraint allowed for a better conditioned numerical problem. It is also observed that the magnitude of the adjoint variables has been reduced. It is possible to reduce their magnitude even further with

additional scaling of quaternions. Notwithstanding, the candidate solution also passed the feasibility check, the results are omitted for brevity.

The necessary conditions for optimality are now analyzed for the scaled problem. It was observed that the mean and standard deviation of the Hamiltonian (see Figure 6.5a) is nearly identical to the theoretical values of -1 and 0, respectively, with a $\mu_H = -1.003$ and a standard deviation of $\sigma_H = 0.0056$. The complementarity conditions are now analyzed (see Figure 6.5b and 6.5d). Covector $\mu_1 \geq 0$ throughout the entire maneuver because the spacecraft is at the maximum allowable angular velocity, and covector μ_2 takes on positive non-zero values only when the cone keep-out limit is binding. The solution can now be verified as extremal. The boresight trajectory is shown in Figure 6.6. As can be seen, the minimum-time maneuver satisfied the bright object constraint by coordinating an off-Eigenaxis rotation that directed the satellite $+z$-body axis around the keep-out cone.

Using DIDO, a numerical solution is obtained at discrete points in time (pseudo-spectral grid). The discrete time slices are referred to as nodes. Typically, it is advantageous to use the smallest number of nodes to reduce computation time. Solving the scaled problem required only 15 nodes while the unscaled problem required at least 20 nodes. Increasing the number of nodes of the unscaled problem slightly (e.g. 25) caused predetermined feasibility and optimality tests to fail–another indication of having a poorly conditioned problem.

This example shows that proper scaling of the optimal control problem (in this case the path constraints in particular) may prevent one from obtaining a solution to the constrained re-orientation problem. On the other hand, by properly scaling the problem, it was seen that the number of required nodes and execution time for the solution could be reduced while the accuracy of the solution was simultaneously enhanced. The next example introduces a more complicated scenario with additional bright object constraints to further emphasize the importance of scaling.

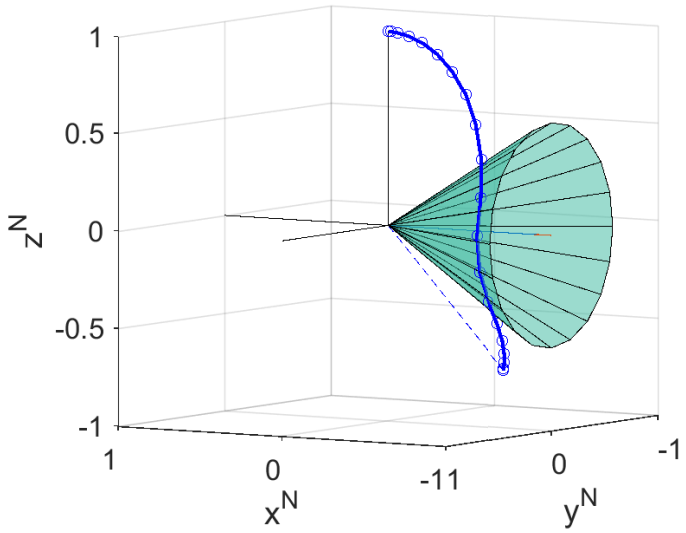

Figure 6.6. Boresight path for single cone avoidance problem.

6.4 Multi-Cone Avoidance Problem

The reorientation problem of the last section is reconsidered, but with the addition of two more boresights and two more bright objects. As mentioned earlier, these additional bright objects could represent the Sun-reflection off the Moon or Earth for certain sensors. For this scenario, there is a total of ten path constraints–the first as a result of the spherical angular velocity constraint and the additional nine as a result of the all possible combinations of the boresight keep out cones with any of the three bright objects.

In addition to the boresight and bright object from the previous example, now referred to as $\hat{\mathbf{b}}_{\mathbf{1}}^{b} = [0, 0, 1]^T$ and $\hat{\mathbf{c}}_{\mathbf{1}}^{N} = [-1, 0, 0]^T$ respectively, two attitude keep-out cones with a 15-deg half-angle were defined to lie nominally in the xy and yz planes. The unit-vectors to the additional bright objects are given by $\hat{\mathbf{c}}_{\mathbf{2}}^{N} = [0.4082, 0.4082, 0.8165]^T$ and $\hat{\mathbf{c}}_{\mathbf{3}}^{N} = [0.6963, 0.6963, -0.1741]^T$. These unit vectors were chosen arbitrarily but are reasonable to represent a situation with a practical system.

6.4.1 Initial Unscaled Solution

The problem with the additional path constraints was coded by using Problem (6.4) as a template. Then, a candidate solution was obtained using DIDO. The maneuver time for the

candidate solution was 157.2 seconds. The solution was examined and it was determined that the keep-out constraints were not violated. A three dimensional visualization of the maneuver is shown in Figure 6.7. The solution also passed the feasibility check.

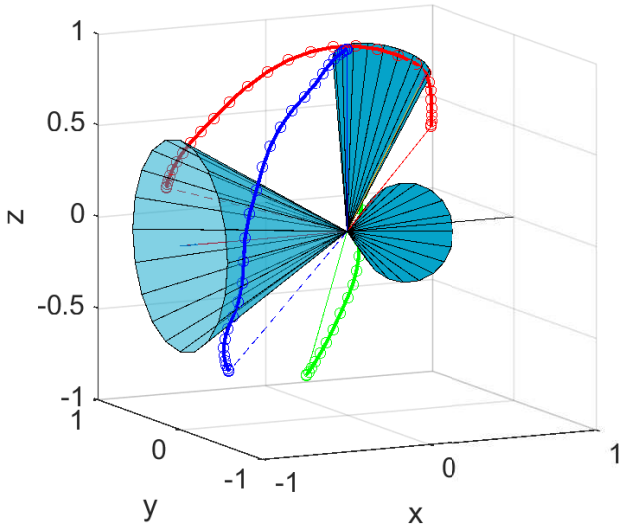

Figure 6.7. Boresight path for a multi-cone avoidance problem.

The optimal solution activated four of the ten path constraints; the magnitude constraint on angular velocity and one constraint for each of the keep-out cones. In this case, b_1 to c_1, b_2 to c_2, and b_3 to c_3 path constraints were activated over a portion of the trajectory. Referring to Figure 6.8a, the necessary condition on the Hamiltonian value is satisfied, with $\mu_H = -0.9995$ and standard deviation of $\sigma_H = 0.0048$. The costate trajectories are reasonable considering the associated quaternion value range of -1 to 1. It was also observed that keep-out cone path constraints were well behaved. A representative keep-out cone path constraint (path constraint 2) is shown in Figure 6.8d. The angular velocity constraint, however, had a multiple of over 4.5 million between h_1 and μ_1. With the exception of Figure 6.8b, every other piece of data would seem to indicate that the solution achieved is in fact extremal. In fact, if this solution was implemented, it would undoubtedly meet the goal of observing all the path constraints. As far as being a valid minimum time solution, though, the dual variables for any state, costate, or path constraint should take on reasonable values when compared to the range of its associated variable. Therefore, scaling of the path constraint h_1 (see Figure 6.8b) was implemented.

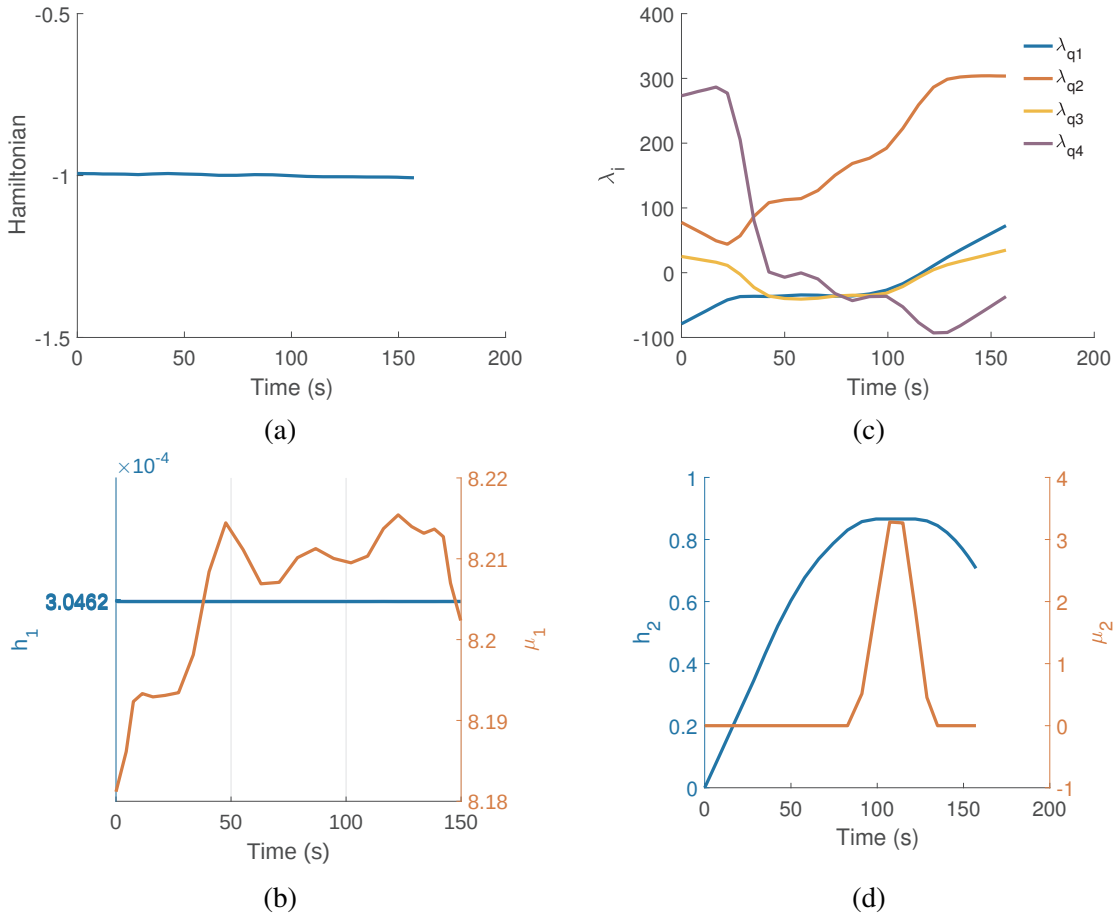

Figure 6.8. Necessary condition checks for unscaled multi-cone problem: (a) Hamiltonian; (b) path constraint 1; (c) costates; (d) path constraint 2.

6.4.2 Scaled Problem

The same problem formulation displayed in the previous section was solved, with the exception that the angular velocity path constraint was scaled in accordance with (6.28). The initial scaling was attempted based on the previous scaled solution results and was implemented because the unscaled μ_1 values for the single and three cone problem formulations were reasonably close in value. After scaling, a new solution with $t_f = 149.8$ seconds was obtained. The new transfer time was 7.4 seconds less than the previously obtained solution. In this case, the shape of the trajectory also completely changed, as shown in Figure 6.9.

The scaled solution passed the feasibility check and the necessary conditions were evaluated (see Figure 6.10). The Hamiltonian value condition again passed, with $\mu_H = -0.9995$ and

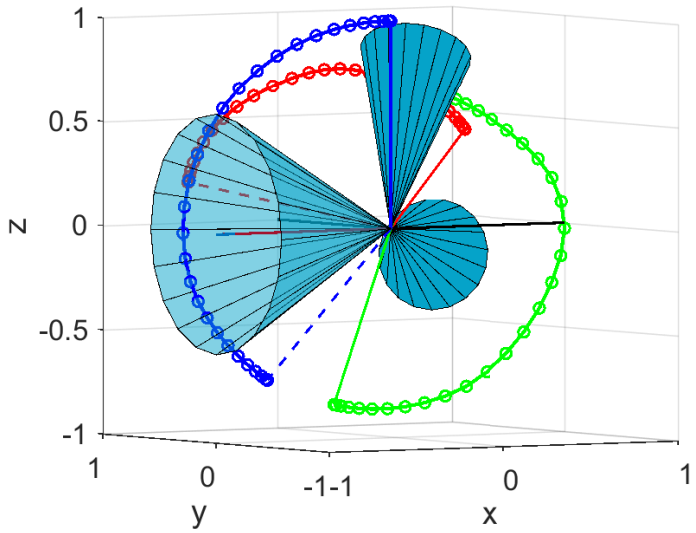

Figure 6.9. Boresight path for scaled multi-cone avoidance problem.

$\sigma_H = 0.0013$. The magnitude difference between h_1 and μ_1 was reduced from over 4.5 million to 135. Both of these are indications that the solution is extremal.

In the absence of an evaluation of the dual space, the initial unscaled solution would have likely been incorrectly accepted as the minimum time solution. However, once it was identified that there was an 'unreasonable' magnitude discrepancy between a path constraint and its multiplier, scaling the problem could be done to obtain the correct solution. Clearly, analysis of the dual space is mandatory for solving and verifying an optimal control problem, particularly if autonomous solutions are sought.

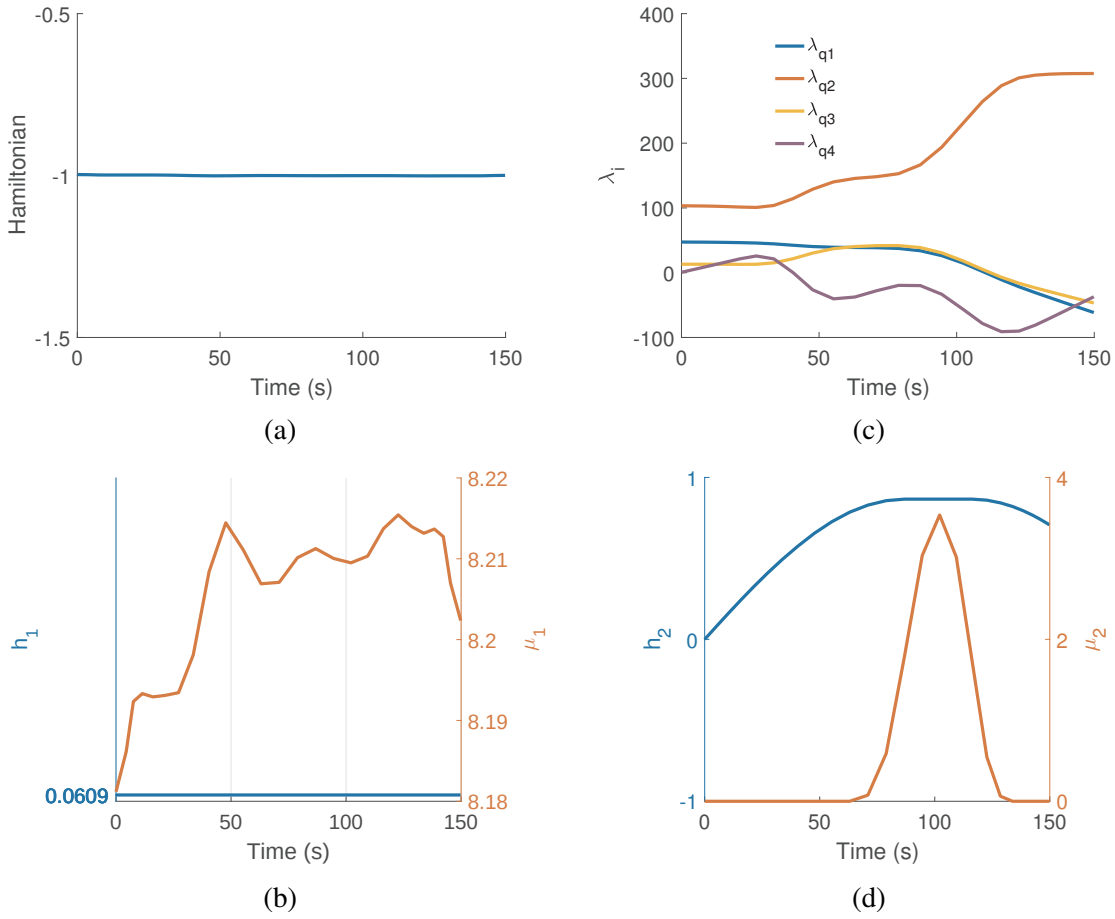

Figure 6.10. Necessary condition checks for scaled multi-cone avoidance problem: (a) Hamiltonian; (b) path constraint 1; (c) costates; (d) path constraint 2.

Comparison to a Typical Technique for Bright-Object Avoidance

As mentioned in Chapter 2, NASA often employs a dog-leg maneuver to avoid pointing instruments and sensors into bright objects. For this method, a middle point in the maneuvering space is defined which allows for two separate maneuvers of the spacecraft. The point is selected such that the bright object constraint will not be violated.

A standard dog-leg maneuver was constructed for the single-cone avoidance example used throughout this chapter. The middle quaternion state was selected such that a 'ZYX' rotation of the BCS was 60, -67.5, and 0 degrees about the yaw, pitch, and roll axis, respectively.

The corresponding quaternion for the selected middle point is shown in (6.29).

$$q_{mid} = \begin{bmatrix} 0.2778 & -0.4811 & 0.4157 & 0.7201 \end{bmatrix}^T \tag{6.29}$$

The state and control solutions are shown in Figure 6.11. The time history of the boresight with respect to the Sun vector is shown in Figure 6.12. It can be seen that the maximum allowable angular velocity of the spacecraft was kept throughout the maneuver and the Sun keep out constraint was not violated. Each leg of the total maneuver took the same amount of time. The total time of maneuver was 175.74 seconds. The 3D representation of the maneuver is shown in Figure 6.13.

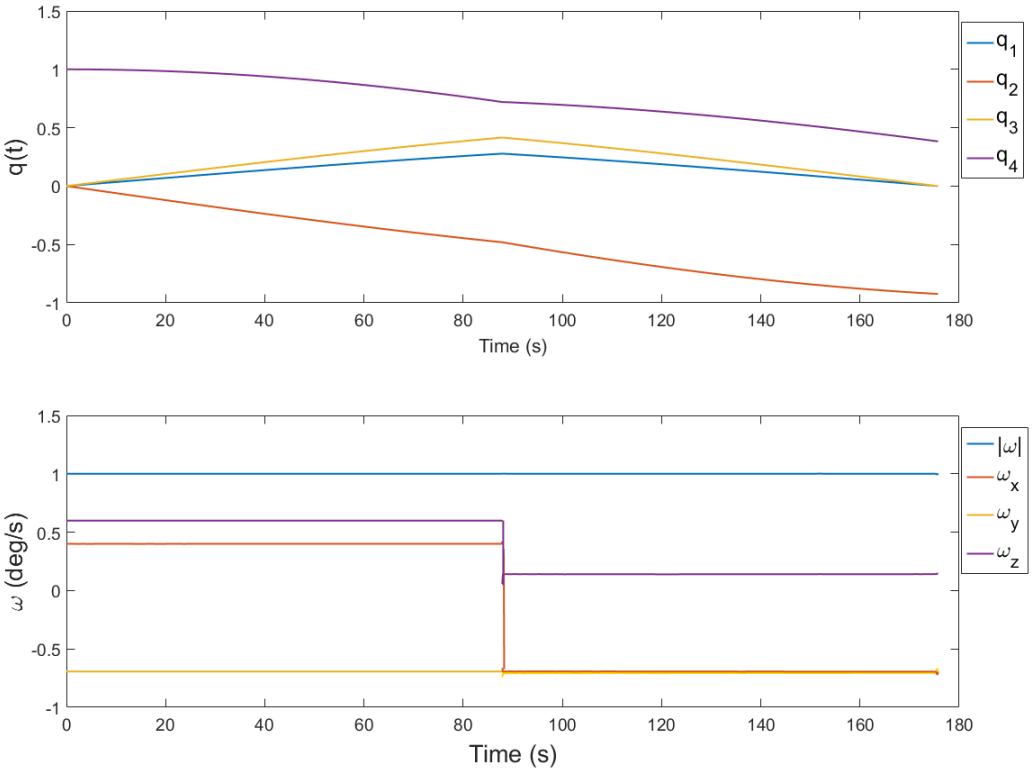

Figure 6.11. Dog-leg maneuver state and control solution.

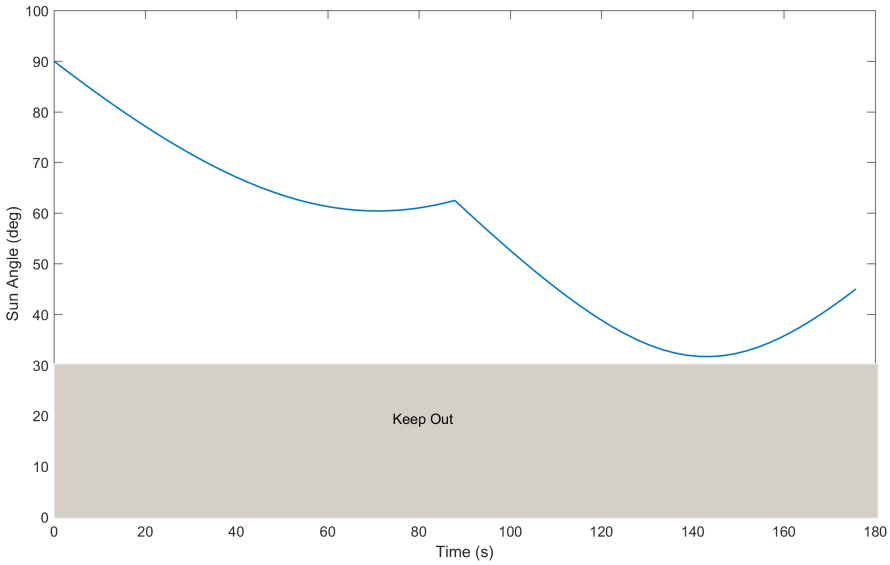

Figure 6.12. Time history of angle between the boresight and Sun vectors for dog-leg maneuver.

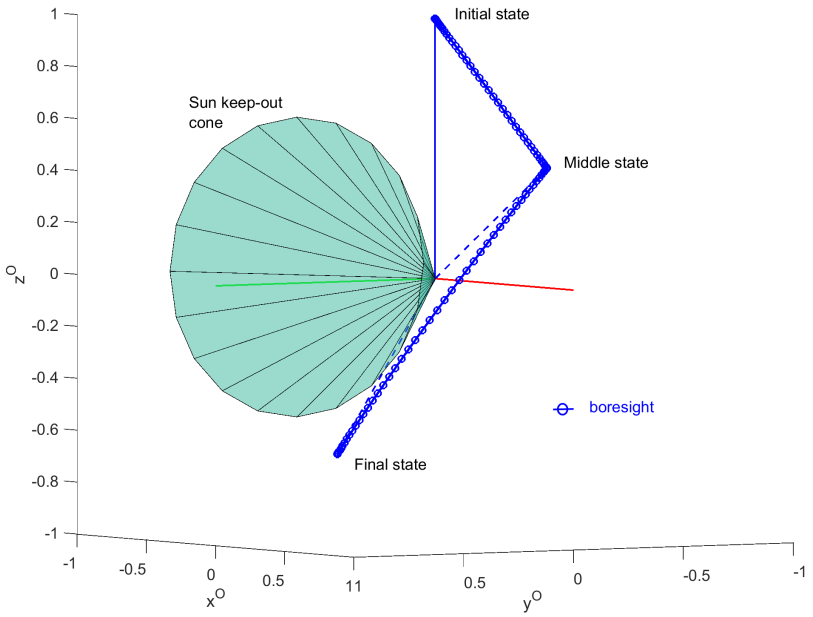

Figure 6.13. State space trajectory for dog-leg maneuver.

Comparison Between Optimal and Current State of Practice

The required time of maneuvers for the single-cone avoidance problem were compared between optimal and current state of practice techniques, as shown in Table 6.2. Included in the comparison is a single positive pitch rotation, which also avoids the bright object constraint. Therefore, a comparison can be made between single axis (eigenaxis), dog-leg, and rapid (or time optimal) maneuvers. In this case, a 225 degree positive-pitch rotation is required, since a single negative pitch rotation of 135 degrees violates the constraint.

Table 6.2. Comparison of time required for the three different maneuver methods.

	Time Required (sec)
225 − *deg* Rotation about +Y axis	225.0
Dog-Leg Maneuver	175.7
Minimum Time Solution	148.7

The minimum time solution required 27 seconds less time than the typically used dog-leg maneuver and 76.3 seconds less time than the single-axis rotation solution. Being that the minimum time solution represents only 85% of the required slew time of the dog-leg maneuver, it can be concluded that applying the optimal problem formulation resulted in the desired effect of reducing time-of-maneuver. This kinematics only solution does not take into account the spacecraft starting and stopping at rest—something the dog-leg maneuver must adhere to for both the middle and final points of the trajectory. This presents another advantage that the minimum time solution may have when compared to the dog-leg maneuver, and can be addressed by including a higher-fidelity dynamics model of the spacecraft in the optimal problem formulation. This is the topic of the next chapter.

6.5 Summary

This chapter has shown that practical solutions to the attitude constrained spacecraft reorientation problem can be obtained by formulating and solving an optimal control problem. In this chapter, a low fidelity model was considered. Solving the problem may be considered as challenging due to the presence of path constrains which may not depend explicitly on the control. In this chapter, pseudospectral optimal control theory, as implemented in

DIDO, was used to obtain solutions autonomously and without the need for a guess. A prerequisite is a properly scaled and balanced numerical problem. In particular, scaling the problem path constraints was found to play a key role in determining solution quality and reducing overall computation time. It was also observed that creating a seemingly more 'complicated' problem by adding numerous path constraints (especially those that are a function of the state) creates a simpler problem to solve by reducing the admissible region of the state space. The results of this chapter could prove extremely useful for automating maneuver planning of attitude constrained satellite operations.

CHAPTER 7:
High Fidelity Maneuver Design

In this chapter, a higher fidelity dynamics model will be used to solve the three cone avoidance problem discussed in Chapter 6. The conservation of momentum will be presented in terms of a path constraint, which allows for the spacecraft angular velocity to be treated as a control. The higher fidelity model will more closely represent the spacecraft physical limitations and allows for a rest-to-rest maneuver. Additionally, advantages of using this model are discussed.

7.1 Higher Fidelity Problem Formulation

So far, a low fidelity dynamics model has been used to illustrate the steps required to autonomously solve the constrained re-orientation problem using optimal control. In practice, such a low fidelity solution could be used as an input to an inner loop attitude control system to replicate the desired trajectory as closely as possible. In such a situation, it is highly desirable that a higher fidelity model be used to better represent the spacecraft dynamics in order to reduce the load on the inner loop. An appropriate problem formulation to solve the higher fidelity problem (Problem H), for a satellite with four reaction wheels, is shown in (7.1).

$$
H: \begin{cases}
\text{Minimize} & J[\mathbf{x}(\cdot), \mathbf{u}(\cdot), t_f] = t_f \\
\\
\text{Subject to} & \dot{\mathbf{q}} = \mathbf{Q}(\boldsymbol{\omega})\mathbf{q} \\
& \dot{\mathbf{h}}_{rw} = \boldsymbol{\tau}_{rw} = [\tau_{rw_1}, \tau_{rw_2}, \tau_{rw_3}, \tau_{rw_4}]^T \\
& \boldsymbol{\omega} = [u_1, u_2, u_3]^T \\
& \boldsymbol{\tau}_{rw} = [u_4, u_5, u_6, u_7]^T \\
& \mathbf{x}(t_0) = [\mathbf{q}^0, \mathbf{h}_{\mathbf{rw}}^{\mathbf{0}}]^T \\
& \mathbf{x}(t_f) = [\mathbf{q}^f, \mathbf{h}_{\mathbf{rw}}^{\mathbf{f}}]^T \\
& \hbar_1(t) \triangleq -0.16 \leq \tau_{rw_1} \leq 0.16\ Nm \\
& \hbar_2(t) \triangleq -0.16 \leq \tau_{rw_2} \leq 0.16\ Nm \\
& \hbar_3(t) \triangleq -0.16 \leq \tau_{rw_3} \leq 0.16\ Nm \\
& \hbar_4(t) \triangleq -0.16 \leq \tau_{rw_4} \leq 0.16\ Nm \\
& \hbar_5(t) \triangleq -14.45 \leq h_{rw_1} \leq 14.45\ Nms \\
& \hbar_6(t) \triangleq -14.45 \leq h_{rw_2} \leq 14.45\ Nms \\
& \hbar_7(t) \triangleq -14.45 \leq h_{rw_3} \leq 14.45\ Nms \\
& \hbar_8(t) \triangleq -14.45 \leq h_{rw_4} \leq 14.45\ Nms \\
& \hbar_9(t) \triangleq I_{11}\omega_x + Z_{11}h_{rw_1} + Z_{12}h_{rw_2} + Z_{13}h_{rw_3} + Z_{14}h_{rw_4} = 0 \\
& \hbar_{10}(t) \triangleq I_{22}\omega_y + Z_{21}h_{rw_1} + Z_{22}h_{rw_2} + Z_{23}h_{rw_3} + Z_{24}h_{rw_4} = 0 \\
& \hbar_{11}(t) \triangleq I_{33}\omega_z + Z_{31}h_{rw_1} + Z_{32}h_{rw_2} + Z_{33}h_{rw_3} + Z_{34}h_{rw_4} = 0 \\
& \hbar_{12}(t) \triangleq \left[C_b^N(\mathbf{q}(t))\hat{\mathbf{b}}_1^b\right]^T \hat{\mathbf{c}}_1 \leq \cos(\theta_1) \\
& \hbar_{13}(t) \triangleq \left[C_b^N(\mathbf{q}(t))\hat{\mathbf{b}}_2^b\right]^T \hat{\mathbf{c}}_1 \leq \cos(\theta_2) \\
& \hbar_{14}(t) \triangleq \left[C_b^N(\mathbf{q}(t))\hat{\mathbf{b}}_3^b\right]^T \hat{\mathbf{c}}_1 \leq \cos(\theta_3) \\
& \hbar_{15}(t) \triangleq \left[C_b^N(\mathbf{q}(t))\hat{\mathbf{b}}_1^b\right]^T \hat{\mathbf{c}}_2 \leq \cos(\theta_1) \\
& \hbar_{16}(t) \triangleq \left[C_b^N(\mathbf{q}(t))\hat{\mathbf{b}}_2^b\right]^T \hat{\mathbf{c}}_2 \leq \cos(\theta_2) \\
& \hbar_{17}(t) \triangleq \left[C_b^N(\mathbf{q}(t))\hat{\mathbf{b}}_3^b\right]^T \hat{\mathbf{c}}_2 \leq \cos(\theta_3) \\
& \hbar_{18}(t) \triangleq \left[C_b^N(\mathbf{q}(t))\hat{\mathbf{b}}_1^b\right]^T \hat{\mathbf{c}}_3 \leq \cos(\theta_1) \\
& \hbar_{19}(t) \triangleq \left[C_b^N(\mathbf{q}(t))\hat{\mathbf{b}}_2^b\right]^T \hat{\mathbf{c}}_3 \leq \cos(\theta_2) \\
& \hbar_{20}(t) \triangleq \left[C_b^N(\mathbf{q}(t))\hat{\mathbf{b}}_3^b\right]^T \hat{\mathbf{c}}_3 \leq \cos(\theta_3)
\end{cases} \tag{7.1}
$$

In the formulation of Problem H, the quaternion and angular momentum of the each reaction wheel form the state vector and the spacecraft angular velocity and torque of each reaction

wheel form the control vector. Although this may seem counter-intuitive in that making the angular velocity a control would imply the spacecraft has infinite acceleration, adherence to the dynamics is obtained by implementing three additional path constraints ($\hbar_9$ through $\hbar_{11}$) to enforce momentum conservation at all times between the spacecraft body and the reaction wheel array for a zero net-bias maneuver. By setting up the path constraint in this way, the angular velocity is directly tied to the reaction wheel momentum state, and therefore implicitly to the reaction wheel torques. Similarly, the angular velocity could have been implemented as a state and $\hbar_9$ through $\hbar_{11}$ could have been eliminated by inserting Euler's equations as part of the dynamics. Note that the torque and angular momentum limits of the reaction wheels are also path constraints and are represented by $\hbar_1$ through $\hbar_8$. These are physical limitations and are often referred to as box constraints. The nine keep-out zone constraints ($\hbar_{12}$ through $\hbar_{20}$) used in the low fidelity 3 cone avoidance problem were also replicated in this problem.

Rest-to-rest boundary conditions allow the satellite the opportunity to start and stop at rest, which is more reasonable for practical maneuvers. In the low fidelity solutions, a rest-to-rest maneuver is not achievable. In this section, the same 135-deg pitch maneuver will be solved but the spacecraft will start and stop at rest. The magnitude of the angular velocity path constraint used in the low fidelity models was an estimate of the ACS to replicate the limit capabilities over the sphere. The actual capabilities of reaction wheels are an angular momentum capability of 14.45 Nms and a torque limitation of ±0.16 Nm. To ensure the rest-to-rest conditions are met, the initial and final angular momentum states of the reaction wheels were selected to be zero ($\mathbf{h}_{rw}^0 = \mathbf{h}_{rw}^f = \mathbf{0}$ Nms).

7.2 Development of the Necessary Conditions

The process outlined in Chapter 6 was used for the high-fidelity problem formulation to develop the necessary conditions. In doing so, possible relationships between primal and dual variables were identified which could be used to also validate the results. With twenty path constraints, many of the equations became quite complex; for purposes of this chapter, only the complementarity and stationary conditions will be highlighted. The complementarity conditions are shown in (7.2) through (7.6).

$$\mu_i = \begin{cases} \leq 0 \text{ if } \hbar_i = -0.16 \\ = 0 \text{ if } -0.16 < \hbar_i < 0.16 \\ \geq 0 \text{ if } \hbar_i = 0.16 \end{cases} \quad \text{for } i = 1, 2, 3, 4 \tag{7.2}$$

$$\mu_i = \begin{cases} \leq 0 \text{ if } \hbar_i = -14.45 \\ = 0 \text{ if } -14.45 < \hbar_i < 14.45 \\ \geq 0 \text{ if } \hbar_i = 14.45 \end{cases} \quad \text{for } i = 5, 6, 7, 8 \tag{7.3}$$

$$\mu_i = \text{arbitrary} \quad \text{for } i = 9, 10, 11 \tag{7.4}$$

$$\mu_i = \begin{cases} \leq 0 \text{ if } \hbar_i = -1 \\ = 0 \text{ if } -1 < \hbar_i < \cos 30^\circ \\ \geq 0 \text{ if } \hbar_i = \cos 30^\circ \end{cases} \quad \text{for } i = 12, 15, 18 \tag{7.5}$$

$$\mu_i = \begin{cases} \leq 0 \text{ if } \hbar_i = -1 \\ = 0 \text{ if } -1 < \hbar_i < \cos 15^\circ \\ \geq 0 \text{ if } \hbar_i = \cos 15^\circ \end{cases} \quad \text{for } i = 13, 14, 16, 17, 19, 20 \tag{7.6}$$

The stationary conditions are shown in (7.7) through (7.13).

$$\frac{\partial \bar{H}}{\partial u_1} = \frac{1}{2}\left[\lambda_{q1}q_4 + \lambda_{q2}q_3 - \lambda_{q3}q_2 - \lambda_{q4}q_1\right] + I_{11}\mu_9 = 0 \tag{7.7}$$

$$\frac{\partial \bar{H}}{\partial u_2} = \frac{1}{2}\left[-\lambda_{q1}q_3 + \lambda_{q2}q_4 + \lambda_{q3}q_1 - \lambda_{q4}q_2\right] + I_{22}\mu_{10} = 0 \tag{7.8}$$

$$\frac{\partial \bar{H}}{\partial u_3} = \frac{1}{2}\left[\lambda_{q1}q_2 - \lambda_{q2}q_1 + \lambda_{q3}q_4 - \lambda_{q4}q_3\right] + I_{33}\mu_{11} = 0 \tag{7.9}$$

$$\frac{\partial \bar{H}}{\partial u_4} = \lambda_{h_{rw1}} + \mu_1 = 0 \tag{7.10}$$

$$\frac{\partial \bar{H}}{\partial u_5} = \lambda_{h_{rw2}} + \mu_2 = 0 \tag{7.11}$$

$$\frac{\partial \bar{H}}{\partial u_6} = \lambda_{h_{rw3}} + \mu_3 = 0 \tag{7.12}$$

$$\frac{\partial \bar{H}}{\partial u_7} = \lambda_{h_{rw4}} + \mu_4 = 0 \tag{7.13}$$

Some of these necessary conditions provide one with the opportunity for additional validation checks once a candidate solution is obtained. Along with evaluating μ_i a posteriori, the stationary conditions can be re-arranged and checked a posteriori as well. This provides seven possible additional checks to validate optimality of the solution. These checks are shown in (7.14) through (7.20).

$$\mu_9 = -\frac{1}{2I_{11}}\left[\lambda_{q1}q_4 + \lambda_{q2}q_3 - \lambda_{q3}q_2 - \lambda_{q4}q_1\right] \tag{7.14}$$

$$\mu_{10} = -\frac{1}{2I_{22}}\left[-\lambda_{q1}q_3 + \lambda_{q2}q_4 + \lambda_{q3}q_1 - \lambda_{q4}q_2\right] \tag{7.15}$$

$$\mu_{11} = -\frac{1}{2I_{33}}\left[\lambda_{q1}q_2 - \lambda_{q2}q_1 + \lambda_{q3}q_4 - \lambda_{q4}q_3\right] \tag{7.16}$$

$$\mu_1 = -\lambda_{h_{rw1}} \tag{7.17}$$

$$\mu_2 = -\lambda_{h_{rw2}} \tag{7.18}$$

$$\mu_3 = -\lambda_{h_{rw3}} \tag{7.19}$$

$$\mu_4 = -\lambda_{h_{rw4}} \tag{7.20}$$

7.3 High Fidelity Solution

The minimum-time maneuver plan determined by solving (7.1) was obtained autonomously by solving the optimal control problem without a guess. The solution gave $t_f = 209.1$ seconds. The additional constraint to start and stop at rest added about 60 seconds to the low fidelity minimum time solution which illustrates the discrepancy arising by assuming a kinematics only solution. The optimal high fidelity trajectory is shown in Figure 7.1. The state and control solutions are shown in Figure 7.2.

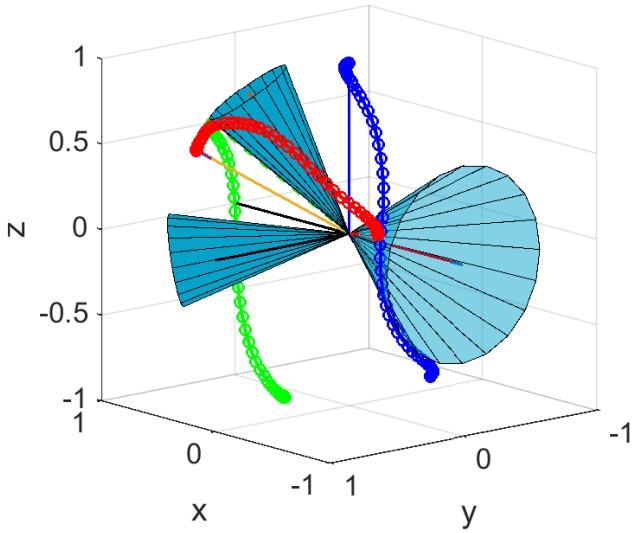

Figure 7.1. Boresight path for high fidelity multi-cone avoidance.

Using the lessons learned on scaling, a solution was obtained that passed feasibility and optimality checks. It can be seen from Figure 7.2 that the spacecraft achieved the desired initial and final orientation while starting and stopping at rest. The magnitude of the angular velocity reached a value slightly higher than 1-deg/s, indicative of how the spherical angular velocity constraint used previously is a conservative estimate of the available momentum space associated with the reaction wheels. As expected, the utilization of a better model of the spacecraft dynamics has impacted the solution. Namely, the inclusion of the rest-to-rest condition adds about 60 seconds to the maneuver (recall in the low fidelity model rest-to-rest requirements could not be asserted). Moreover, the correlation between the numerical solution of Figure 7.2 and a practical implementation of the maneuver will be improved by using the high fidelity model.

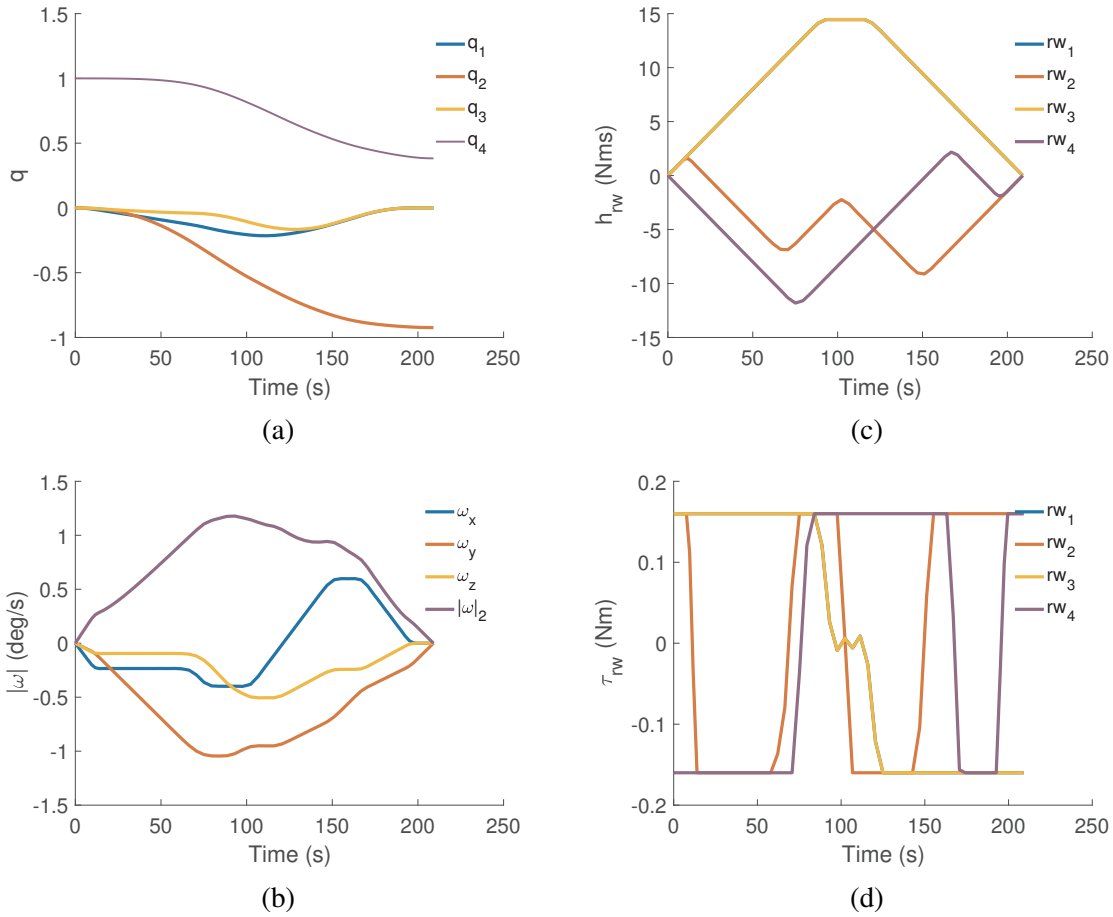

Figure 7.2. High fidelity solution for multi-cone avoidance: (a) quaternion; (b) angular velocity; (c) reaction wheel angular momentum; (d) reaction wheel torque.

7.3.1 Feasibility Checks

The optimal solution and actual propagated system response for the given optimal control input were plotted on the same graph to facilitate a visual feasibility check, as was completed for the low fidelity model in the previous chapter. In this case, however, there are more states and controls. The optimal versus propagated representations are included for the quaternion and angular momentum states. Recall the propagated values are only a function of inputting the optimal control solution into the high-fidelity dynamics equations. All feasibility checks passed and are shown in Figures 7.3 and 7.4. Note that for Figure 7.4, angular momentum time histories for reactions wheels 1 and 3 are identical.

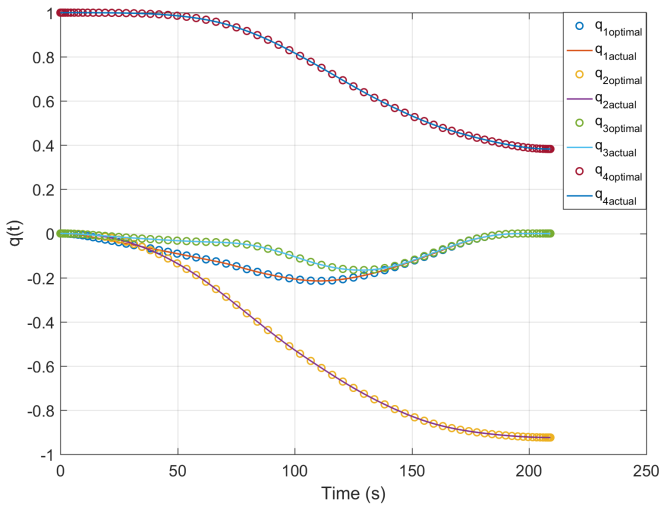

Figure 7.3. Quaternion feasibility check of the high-fidelity optimal solution.

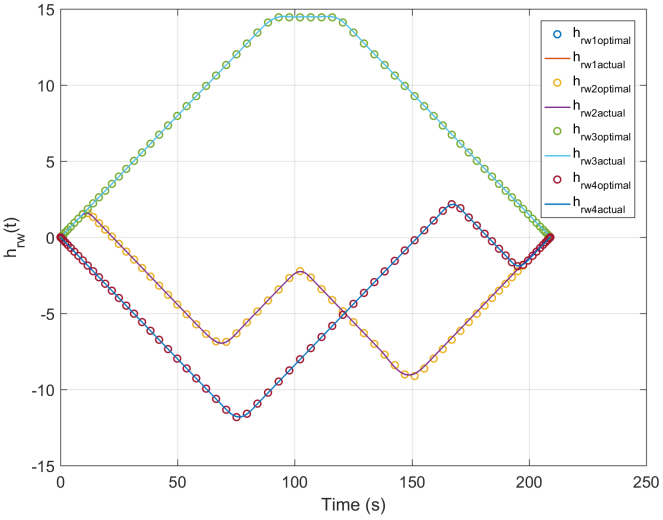

Figure 7.4. Angular velocity feasibility check of the high-fidelity optimal solution.

7.3.2 Optimality Checks

Referring to Figure 7.5a, the necessary condition on the Hamiltonian value is satisfied, with $\mu_H = -0.9954$ and standard deviation of $\sigma_H = 0.0422$. Sample solutions of the time history plots of control, path constraint, and state variables versus their respective dual variables

are displayed in Figure 7.5b, 7.5c, and 7.5d. As can be seen, the solution was well balanced overall. Referring to Figure 7.5b and 7.5d, it is seen that the complementarity conditions are met for these path constraints.

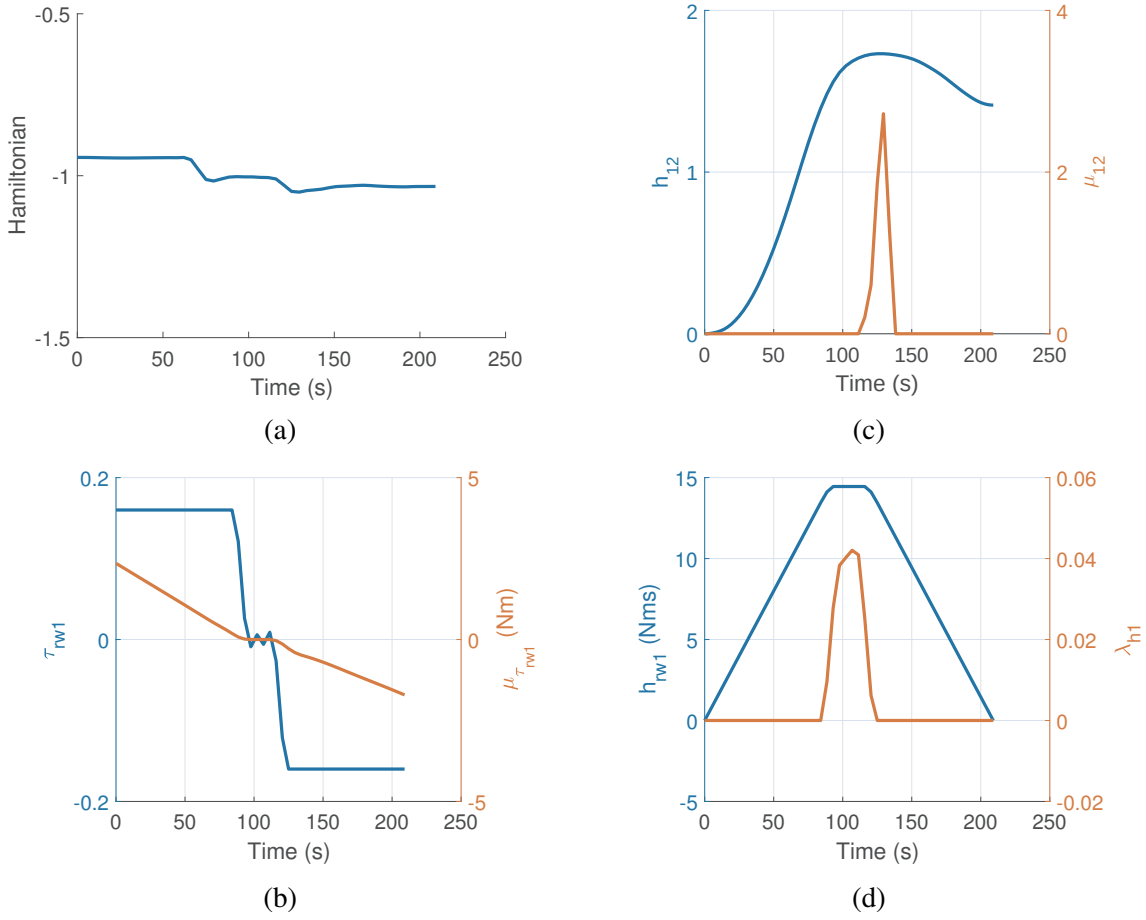

Figure 7.5. Necessary condition checks for high fidelity multi-cone avoidance: (a) Hamiltonian; (b) control/KKT pair; (c) path constraint 12/KKT pair; (d) angular momentum/costate pair.

The stationary conditions on the path covectors for the reaction wheel torque constraints provided a useful metric to further validate the solution. According to (7.17) through (7.20), $\mu_i + \lambda_{h_{rwi}} = 0$ for $i = 1,\ 2\ 3,\ 4$. These theoretical zero values were compared against actual throughout every time step. The mean and standard deviations are displayed in Table 7.1. The check on these stationarity conditions was deemed successful, considering the mean values were, with one exception, within a hundredths place of theoretical after having been calculated post-solution (where computer precision limits and round-off errors are present).

The largest tolerance was associated with μ_3 and $\lambda_{h_{rw3}}$. However, Figure 7.6 shows how these two co-variables take on a symmetric shape, as (7.19) dictates. Between the mean value and visual tests, the stationarity check for the third reaction wheel were deemed successful as well.

Table 7.1. Stationarity conditions check.

Stationary Condition Equation	Theoretical Mean Value	Actual Mean Value	Standard Deviation
$\mu_1 + \lambda_{h_{rw1}}$	0	−0.0405	0.3518
$\mu_2 + \lambda_{h_{rw2}}$	0	−0.0346	0.0657
$\mu_3 + \lambda_{h_{rw3}}$	0	0.1242	0.3275
$\mu_4 + \lambda_{h_{rw4}}$	0	0.0880	0.1515

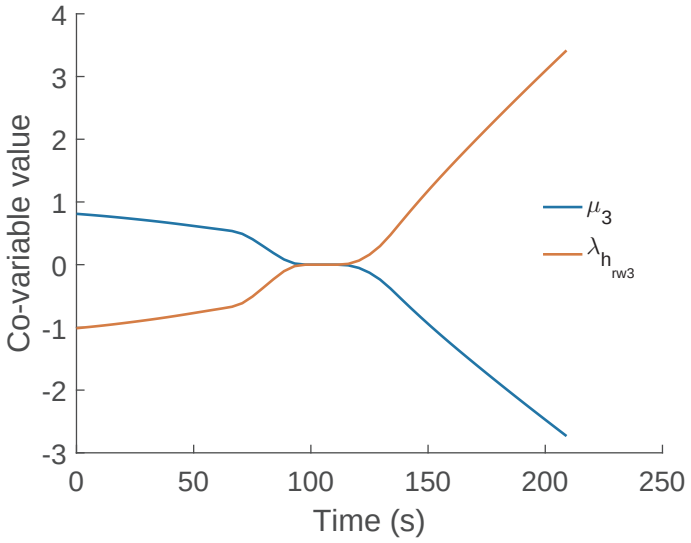

Figure 7.6. Path and state co-variable time histories for torque constraint and angular momentum state (RW3).

7.4 Summary

This chapter has demonstrated that higher fidelity dynamic representations of spacecraft are achievable within the optimal control theory framework. Advantages of utilizing the higher fidelity model include more accurately representing the physical limitations of the spacecraft as well as possibly determining a more useful input to the actual spacecraft.

Although the problem formulation may seem more complex, proper scaling and balancing of states, control, path constraints and their associated covectors allows for an autonomous optimal solution. It has also been shown that both the complementarity and stationary conditions can be used as a validation tool when testing optimality.

THIS PAGE INTENTIONALLY LEFT BLANK

CHAPTER 8:
Application to the LRO

This chapter will examine a real-world scientific application of the LRO. The scientific objective of gathering dust scatter along the Lunar horizon, just following Sunset, using the LOLA instrument will be studied. The current maneuver design will be compared against the minimum time solution, using the version of the high-fidelity model studied in Chapter 7. It will be shown that the scientific mission can be enhanced by allowing for less time in transit to target. Comparisons will be made by applying a minimum time solution to two independent LOLA maneuvers which were actually flown by NASA; the first on October 30, 2017 and the second on November 17, 2017.

8.1 Scientific Mission Specifics

As previously mentioned, the LRO and its instruments have continued delivering valuable scientific data since the satellite's launch in 2008. One recent mission of the LOLA instrument has been to point the instrument along the horizon of the Moon in the minutes prior to Sunrise or following Sunset (over the local horizon). In doing so, LOLA can measure dust within the solar illumination (or glow) near the surface. Note that the component of LOLA which points along the horizon is not from the main nadir-pointing part; rather, the anti-nadir pointing component. A depiction of this maneuver is shown in Figure 8.1. Note how the instrument field-of-view (FOV) is pointed along the horizon while the Sun is located just beneath the Lunar horizon.

The LOLA science team is located in NASA GSFC in Goddard, Maryland, conveniently co-located with the LRO Missions Operations Center (MOC). Presently, LOLA scientists submit the horizon slew request to the MOC [11]. The verbal description of the scientific objective is translated into a sequence of roll and pitch maneuvers. From previous experience, it has been observed that a two-leg maneuver consisting of independent roll and pitch slews is a typical solution. Referencing nominal nadir pointing, a roll of approximately 70 degrees or more is needed, followed by a pitch maneuver, the size of which is dependent on the Sun Beta angle and how ecliptic the orbit [11]. The LOLA science team request is only concerned with a pointing vector from the spacecraft to a specific target for a duration of

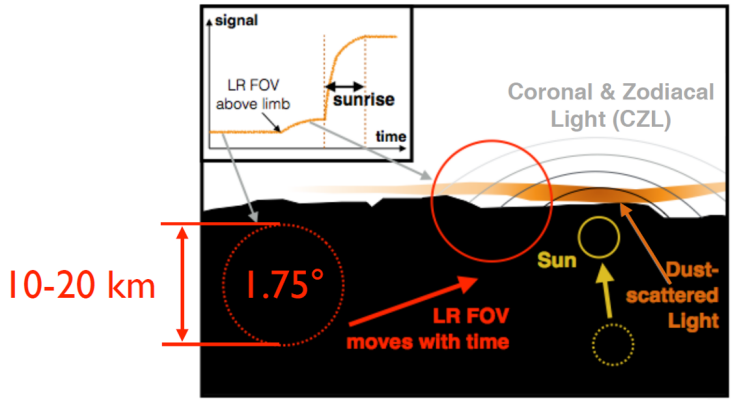

Figure 8.1. Lunar horizon-pointing mission for LOLA. Source: [11].

time. Since the science team is not concerned with the orientation of the FOV during the data collection, yaw is a free constraint.

The coarse estimate of required roll and pitch maneuvers along with desired time-on-target is input into LRO AttMan software. Currently, the NASA team typically uses an iterative process to hone in on an acceptable solution. As discussed in the LRO overview in Chapter 2, if there are any violated constraints flagged from AttMan, the MOC will reach back to the LOLA science team to modify, cancel, or re-schedule the desired maneuver. It should be noted, as well, that the LOLA science team must also ensure their mission does not conflict with other science team requests. Having said this, it is reasonable to assume that reducing slew times would reduce the footprint of the LOLA team on the planning schedule. Thus, there's benefit to reducing slew time from this point of view as well as allowing for greater time on target.

For any mathematical framing of the problem, it is important to understand the targeting requirements of the LOLA science team. In this case, they are providing a pointing vector and a desired time on target. The pointing vector is given in the ECI coordinate system with which the nominally anti-nadir boresight of the LOLA instrument must be aligned. If aligned, the boresight should be pointed to the Sun (along the Lunar horizon) at the desired time. The orientation of the spacecraft is then held in place and the science is gathered in the minutes when the Sun is just below horizon, whether at Sunrise or Sunset. When the Sun is in view, this boresight component of LOLA is saturated and does not gather science,

but it is not damaged (i.e., it does not have to be turned off). Prior to moving forward with the example maneuvers, it is important to translate the output of the LOLA team into a desired target quaternion in an appropriate reference frame.

8.2 Determining the Quaternion at Time on Target

Given the desired pointing vector (**P**) at a desired time on target (TOT), the final quaternion can be calculated using the ephemeris data of the Moon and LRO and the coordinate transformation equations discussed in Chapter 5. The ephemeris of the Sun will also be required to ensure any bright object constraints of the nadir instrument deck or star trackers are not violated. The specific ephemeris data used was the data tied to the desired TOT. Knowing a target quaternion would be needed for the optimal control problem formulation, the method below was developed for purposes of this thesis, which is independent to that of the LRO MOC.

One method to calculate the final quaternion ($\mathbf{q}_f$) relies on relating two vectors to one another in the same reference frame. With two free vectors in the same reference frame, one can use the definitions of dot and cross-products to directly compare them (as discussed in Chapter 4). In this case, since the used portion of the LOLA boresight is exactly 180 degrees off the nadir instrument deck, the negative of the pointing vector was calculated and compared against the nominal attitude of the LRO, with the main instrument suite pointed nadir. This is the same problem; it just focuses on aligning nominal nadir to the negative of the pointing vector rather than the negative of the nominal nadir to the positive of the pointing vector. This method was selected since most of the other missions rely on pointing the main instrument suite to a desired target and is a more general approach to solve future problems that are not LOLA specific.

With this one transformation, one can now define the nadir pointing vector and the pointing vector in the OCS. Per the definition of the OCS, LRO nadir boresight is defined as $\mathbf{b}_1 = [0\ 0\ 1]^T$. Given **P** and $\mathbf{b}_1$, the eigenaxis and rotation angle can be calculated using the cross and dot products between the vectors (see (4.19) and (4.20)). In this case, the nadir and pointing vectors are both free and can be placed onto the LRO body. The Lunar OCS can be held fixed at the moment in time these two vectors are compared, since they are both defined in the same reference frame. Ultimately, by solving for the eigenaxis (**e**) and its

associated angle of rotation (Φ), a final quaternion can be calculated (see (4.21)).

With an initial and final quaternion now calculated, the problem for LRO minimum-time maneuvers can be formulated.

8.3 LRO Rapid Slew Formulation

The high fidelity dynamics model used in Chapter 7 with LRO's parameters was used to solve for LRO specific maneuvers. The actual moment of inertia tensor was updated to the actual values implemented in NASA's high-fidelity dynamics model, which changes based on satellite solar panel configuration. The reaction wheel distribution matrix of LRO is identical to the example from the previous chapter, which is restated in (8.1).

$$\mathbf{Z} = \begin{bmatrix} 0.8192 & 0.8192 & -0.8192 & -0.8192 \\ 0.4056 & -0.4056 & -0.4056 & -0.4056 \\ 0.4056 & 0.4056 & 0.4056 & 0.4056 \end{bmatrix} \tag{8.1}$$

Problem H (7.1) from Chapter 7 was updated to reflect LRO capabilities and constraints. Most notably, the allowable range of angular momentum was decreased to $h_{rw} = \pm\ 2.1$ Nms to represent the allocated slew momentum. The bright object vectors $\mathbf{c}_2$ and $\mathbf{c}_3$ were also updated to represent the unit vector to the Earth and Moon, respectively, since the star tracker (ST) boresights, represented by $\mathbf{b}_2$ and $\mathbf{b}_3$ have operational constraints on these bodies (in addition to the Sun) as discussed in Chapter 2. In this context, LRO is less conservative than the high-fidelity solution from the previous examples because the LRO MOC allows one ST to be within a bright object constraint at any given time, given its not for an extended period [11]. The way in which the problem has been set up allows for a rest-to-rest maneuver from nadir to the final quaternion at the specified TOT. The initial maneuver time can then be calculated by subtracting the required time of maneuver (TOM) from the TOT.

Currently, NASA has increased its initial restriction placed on LRO angular velocity of 0.1 deg/s per axis to 0.13 deg/s per axis. In this chapter, this restriction was not placed on the problem for two reasons. Firstly, the higher fidelity model used allows for a more accurate representation of the actual physical limitations of the satellite, based on reaction wheel

specifications. Secondly, the distribution of the reaction wheel assembly is heavily favored for rotation about the body x-axis (roll), as shown in the first row of (8.1). Therefore, there are some typical roll heavy maneuvers that could benefit from the configuration that is already in place.

Two maneuvers for LOLA science actually flown by NASA will be explored. A minimum-time solution will be presented and compared against NASA's selected maneuver. The NASA maneuver will be represented in two ways; firstly, by the attitude prediction output of the AttMan planner and, secondly, by the actual telemetry data received from the LRO after having completed the maneuver. Due to the nature of this particular LOLA mission, the Sun constraint for the main instrument suite was not a subject of concern. This was due to the fact that the anti-nadir component of LOLA was being pointed directly at the Sun as it set, leaving the main instrument suite pointed directly away from the Sun. This being said, the problem formulation still accounted for all constraints (they were simply non-binding) and can be used for all scientific and calibration maneuvers. The first maneuver discussed took place on October 30, 2017 (Day 303) and was selected because this was mostly a roll maneuver, so the benefit of taking advantage of the reaction wheel momentum distribution could be explored further.

It should be noted that the problem formulation presented in this chapter did not account for any line-of-sight blockage caused periodically by the Moon when it is positioned between an instrument or sensor field-of-view and the Sun or Earth. In that sense, the approach used here is conservative. In this method, however, one can check the path constraints against these blockage time-periods, and re-solve the problem with the keep-out cone deactivated if that proved to be the case. This will be addressed further in the next chapter in the discussion about possible future work.

8.4 Day 303 Maneuver Results

8.4.1 Minimum Time Solution

The minimum time state and control trajectories for the Day 303 maneuver were solved. The desired TOT was 09:49:00 (hh:mm:ss). The total time of maneuver required was 418 seconds. The quaternion and reaction wheel angular velocity state trajectories were

propagated using the solved optimal control to ensure feasibility. The feasibility check was successful. The results are shown in Figures 8.2 and 8.3. The solution also passed all optimality checks, which were discussed at length in the previous two chapters, and hence omitted for brevity here.

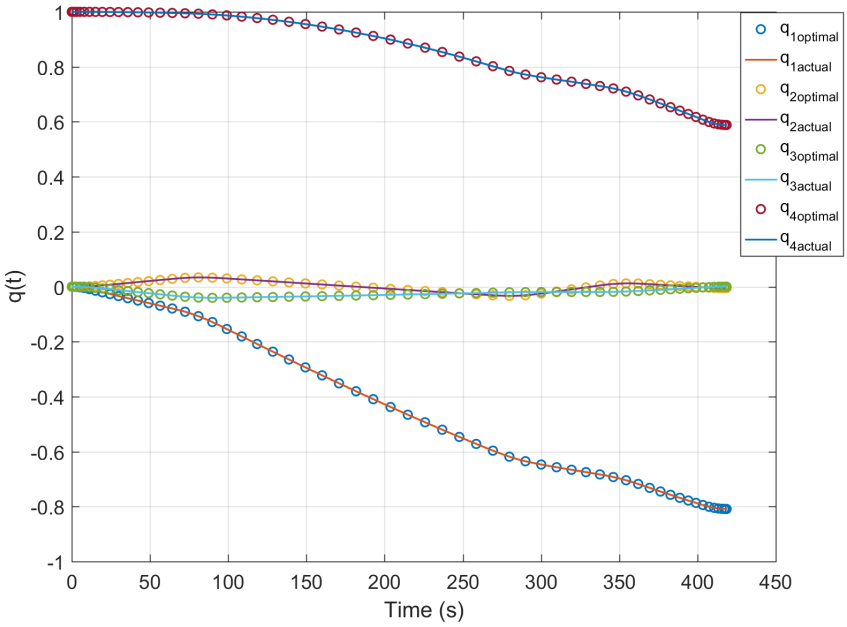

Figure 8.2. Quaternion results with feasibility check.

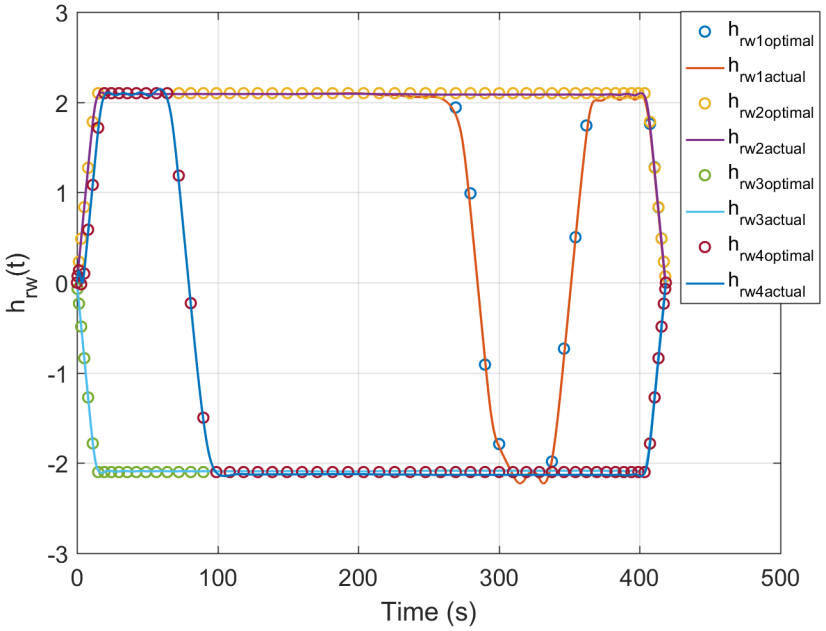

Figure 8.3. RW angular momentum results with feasibility check.

8.4.2 Comparison to Current State of Practice

The quaternion time histories of the AttMan output and LRO telemetry, along with the optimal trajectory, were visualized in the Systems Tool Kit (STK) program, which allows one to enter the ephemeris of the LRO orbit along with attitude profiles. Conveniently, STK allows the user to select from any of many epochs as well as enter attitude in an inertial or local reference frame. The results of all three sets of data were also plotted against each other to check for any pointing or timing error associated with the pointing vector and desired TOT. The results of the anti-nadir LOLA component pointing error, as a function of time, is shown in Figure 8.4.

Clearly, the optimal trajectory has the advantage in that the maneuver can be initiated well after it was in practice. The overall results are displayed in Table 8.1, where θ_{error} is used to represent the pointing error of the instrument boresight.

It was observed that the optimal solution was able to achieve zero-pointing-error precisely at the requested TOT of 09:49:00. The optimal solution did this in 50% of the time for the planned maneuver in AttMan and 48% of the time of the actual maneuver interpreted

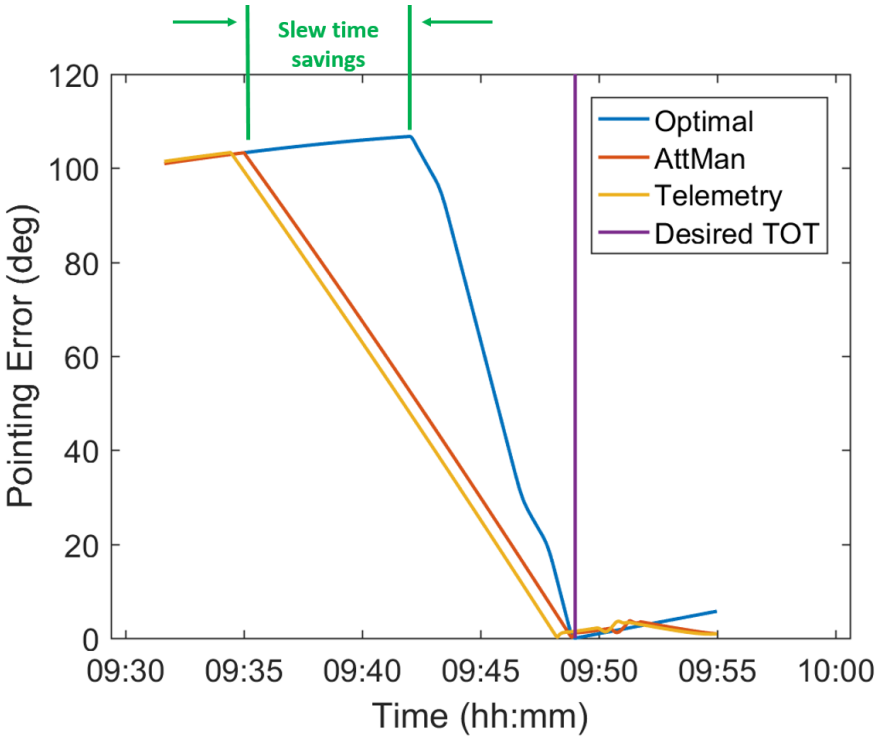

Figure 8.4. Pointing error for Day 303 maneuver.

Table 8.1. Day 303 maneuver comparison results.

Data Type	**Required Maneuver Time (min:sec)**	**Maneuver Start Time (hh:mm:ss)**	θ_{error} **at TOT (deg)**	**Minimum** θ_{error} **(deg)**	**Time of Minimum** θ_{error} **(hh:mm:ss)**
Rapid Slew	6:59	09:42:02	0.0	0.0	09:49:00
AttMan	13:59	09:35:01	1.14	0.205	09:48:52
Telemetry	14:34	09:34:26	1.46	0.2153	09:48:15

from the telemetry. For NASA's maneuver, the instrument of LOLA had a minimum angle of approach to the Sun earlier than desired, with the angle error increasing as it progressed toward desired TOT. Although the team was still able to collect data, a more precise angle and timing alignment could improve collection efforts [11]. The STK visualization validated the result, as shown in Figure 8.5. The field of view of the anti-nadir component of the LRO is a simple-conic shape, with a cone half angle of 1.75 degrees [11].

In this scenario, the Sun was setting beneath the horizon and the orientation was held for 600 seconds to gather the science data.

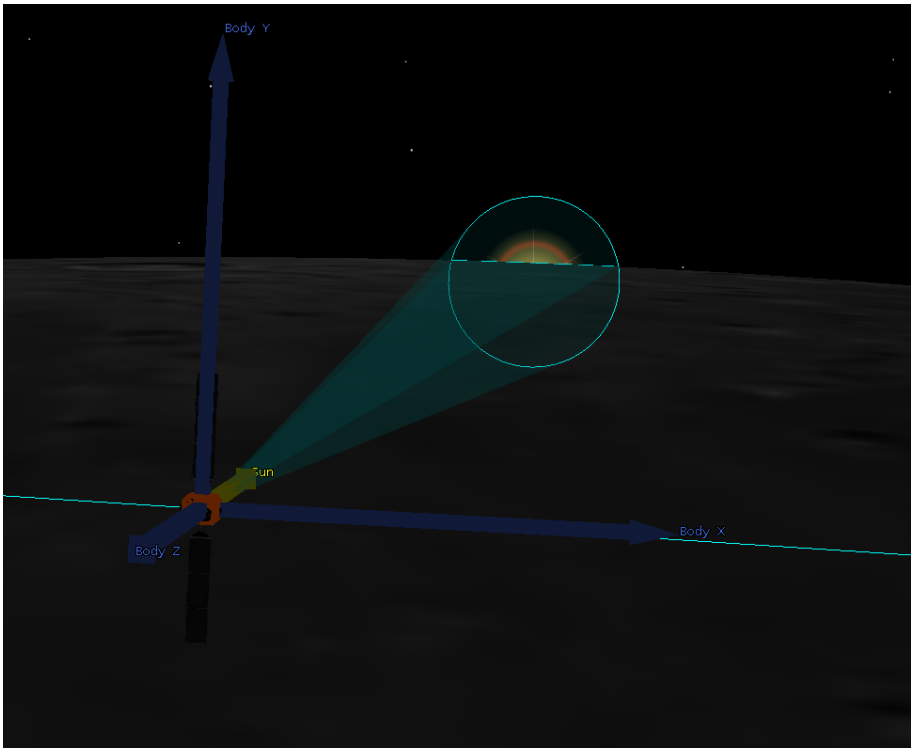

Figure 8.5. STK visual result for day 303 optimal maneuver.

Although the nature of this maneuver does not place the main instrument boresight at risk for entering the Sun keep-out cone, the two star trackers (ST1 and ST2) bright object constraints on the Sun, Earth, and Moon still had to be checked. The resulting ST boresight angles with the respective celestial bodies is shown in Figure 8.6. It can be observed in Figure 8.6e that the 15 degree cone half-angle constraint was violated, but ST1 was fully operational at that point in time. Therefore, it meets the conditions placed by the LRO MOC.

Knowing in practice that NASA implemented a nearly roll-only maneuver, the Euler angles of roll and pitch time histories were plotted for the three data sets in Figure 8.7. Note that yaw was not included as it has no effect on the desired orientation of the boresight. Varying yaw only changes the orientation in which the field-of-view observes the given area. By lifting this constraint, a slight reduction in required maneuver time may be possible and will be addressed further in the concluding chapter. It was observed that the optimal solution

incorporated some positive and negative pitch in the maneuver where the AttMan solution had none. It was also seen that there was about a 2 degree discrepancy between roll and pitch values between the AttMan output and the telemetry data, although the reason behind it is unclear.

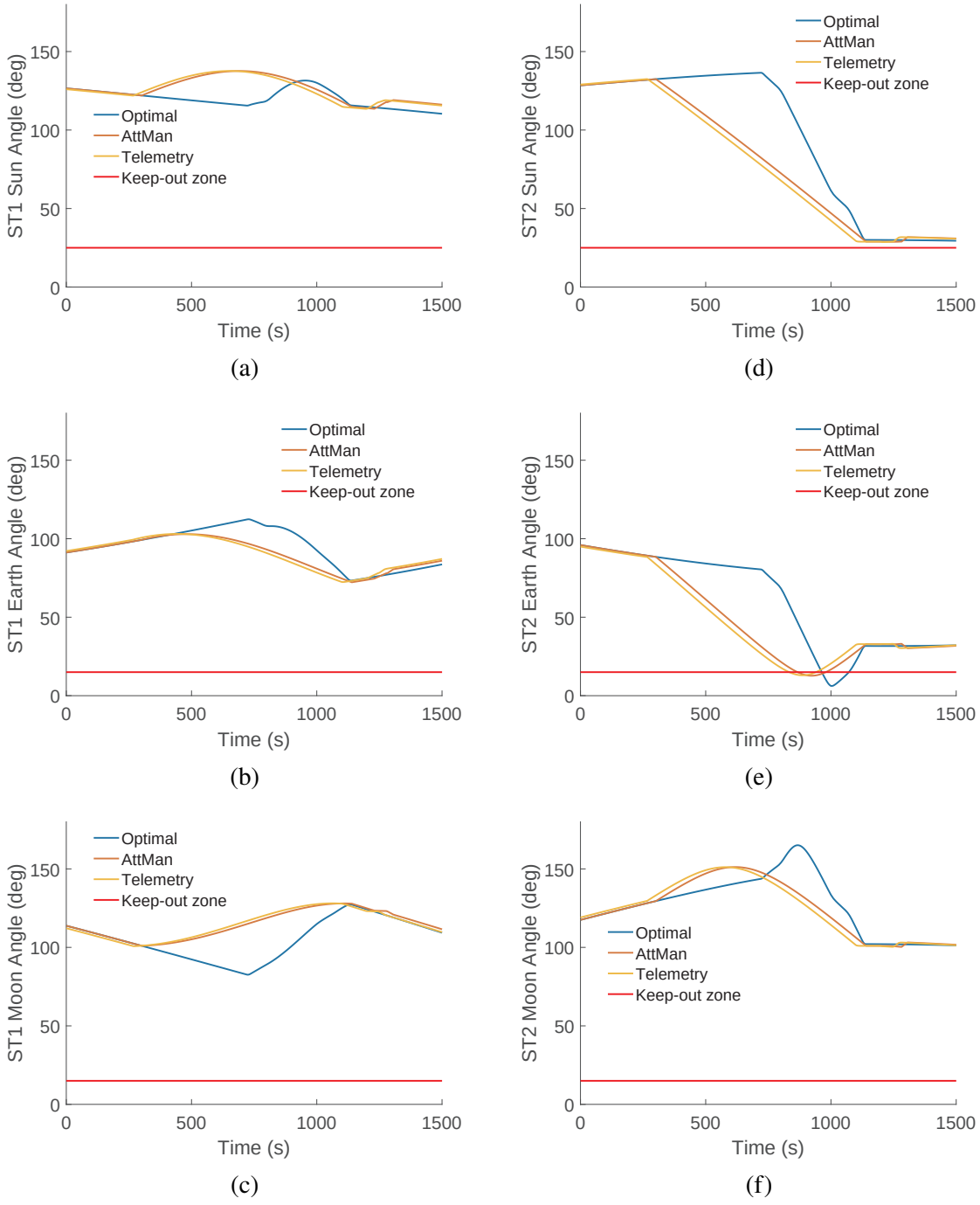

Figure 8.6. Star tracker orientation with respect to the Sun, Earth, and Moon: (a) ST1 to Sun; (b) ST1 to Earth; (c) ST 1 to Moon; (d) ST 2 to Sun; ST2 to Earth; ST2 to Moon.

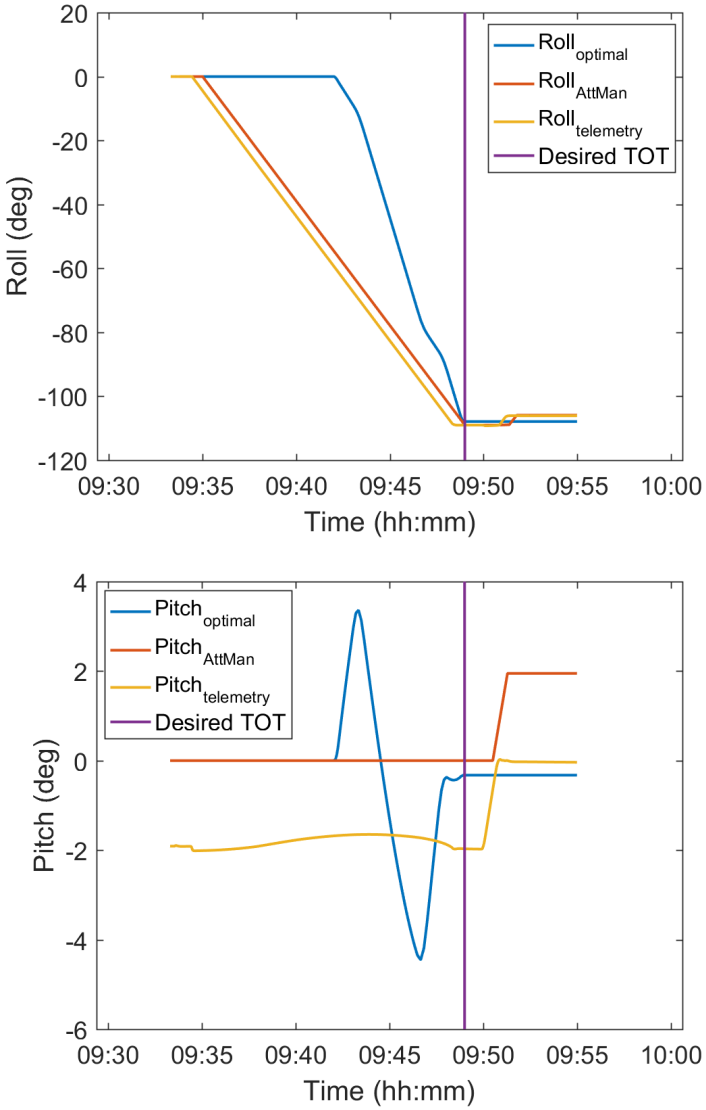

Figure 8.7. Roll and pitch angles for Day 303 maneuver.

8.4.3 Analysis

For the Day 303 maneuver, the slew time reduction was quite sizable due to two contributions. First, the trajectory of the spacecraft was not limited to a roll-only maneuver and an optimal solution, which took into account a non-uniform inertia tensor and the distribution of the reaction wheel assembly torques. Second, the angular velocity about any given body-axis was not limited to 0.13 deg/s, but rather defined by the ±2.1 Nms momentum limits of the individual wheels. This can be seen in the angular velocity time history, shown in Figure 8.8.

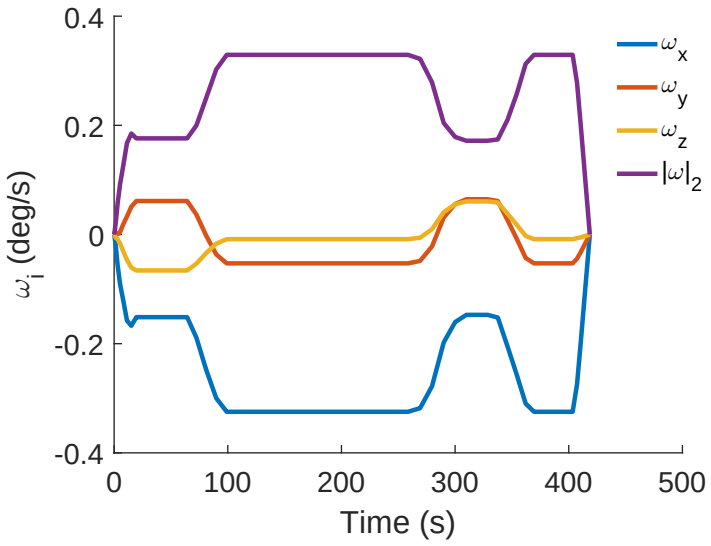

Figure 8.8. Angular velocity time history for minimum time Day 303 maneuver.

Per (8.1), each of the four reaction wheels is placing the majority of its torque output about the x-axis, based simply on distribution matrix (evidenced by the first row values of $\mathbf{Z}$). Therefore, by not limiting each of the three axes to a singular value, a faster maneuver could be accomplished. In the optimal case, angular velocity was not limited per say; rather, the specifications of the reaction wheels and their orientation determined the maximum body angular velocity capability. It should be noted, however, that minimum-time solutions with bright-object avoidance would still show a reduction in maneuver time, even if NASA would like to maintain or re-establish a maximum limit of angular velocity—whether constant or varying limits are established for each axis.

8.5 Day 321 Maneuver Results

8.5.1 Minimum Time Solution

The minimum time state and control trajectories for the Day 321 maneuver were solved. The desired TOT was 03:23:58 (hh:mm:ss). The total time of maneuver required was 675.4 seconds. The quaternion and reaction wheel angular velocity state trajectories were propagated using the solved optimal control to ensure feasibility. The feasibility check was successful. The results are shown in Figure 8.9 and 8.10. The solution also passed optimality checks.

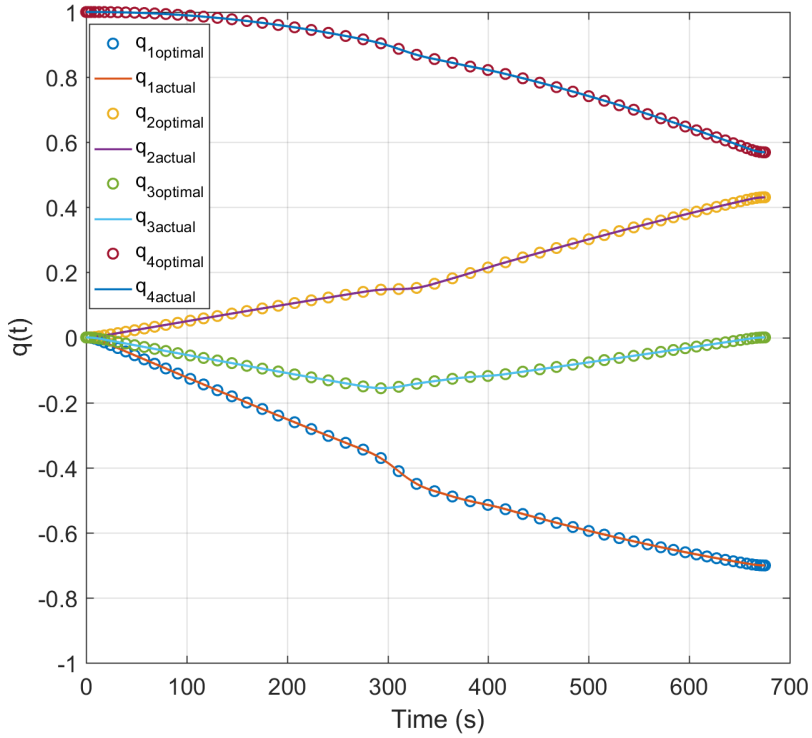

Figure 8.9. Quaternion results with feasibility check for Day 321 maneuver.

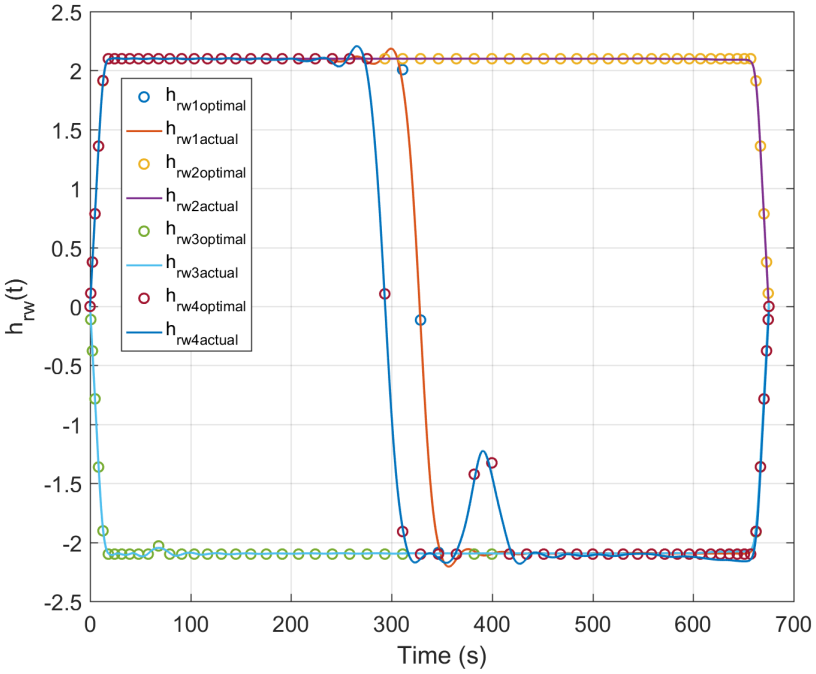

Figure 8.10. RW angular momentum results with feasibility check for Day 321 maneuver.

8.5.2 Comparison to Current State of Practice

The results of the anti-nadir LOLA component pointing error, as a function of time, is shown in Figure 8.11. Again, the optimal trajectory has the advantage in that the maneuver can be initiated well after it was in practice. The overall results are displayed in Table 8.2.

Just like in the first example, it was observed that the optimal solution was able to achieve zero-pointing-error precisely at the requested TOT (03:23:58). The optimal solution did this in about 65% of the actual maneuver time. For NASA's maneuver, the instrument of LOLA had a minimum angle of approach to the Sun later than desired, with relatively high angle error at desired TOT. The STK visualization validated the result, as shown in Figure 8.12. In this scenario, the Sun was setting beneath the horizon and the orientation was held for 600 seconds to gather the science data. For comparison purposes, the predicted orientation provided by AttMan data at TOT is included in Figure 8.13.

The ST boresight angles with the respective celestial bodies is shown in Figure 8.14. None

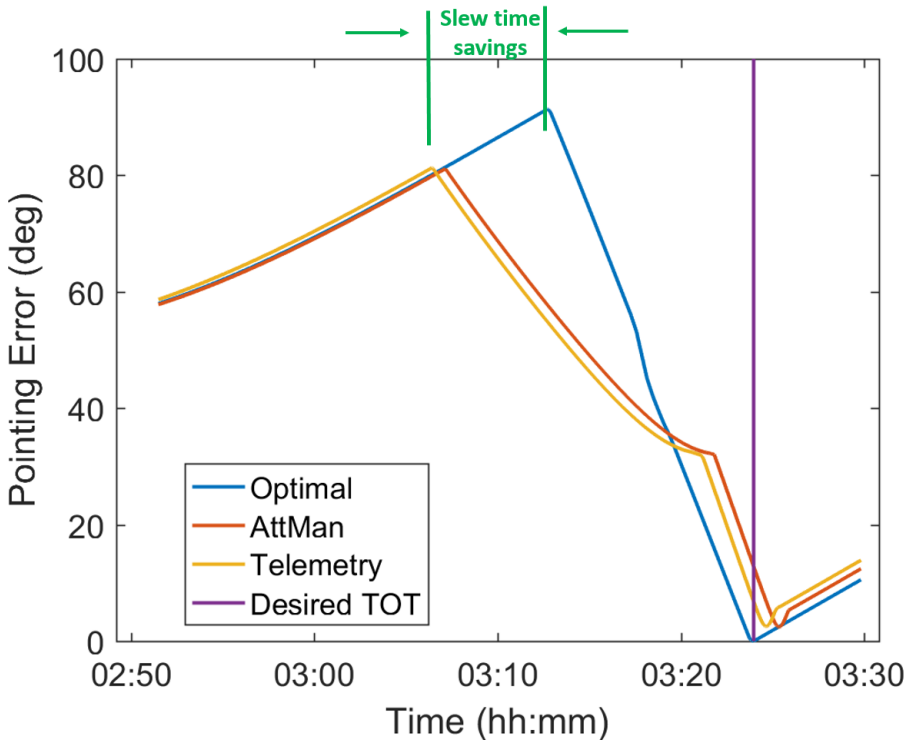

Figure 8.11. Pointing error for Day 321 maneuver.

Table 8.2. Day 321 maneuver comparison results.

Data Type	**Required Maneuver Time (min:sec)**	**Maneuver Start Time (hh:mm:ss)**	θ_{error} **at TOT (deg)**	**Minimum** θ_{error} **(deg)**	**Time of Minimum** θ_{error} **(hh:mm:ss)**
Rapid Slew	11:15.5	03:12:43	0.0	0.0	03:23:58
AttMan	16:49	03:07:09	12.81	2.42	03:25:21
Telemetry	17:33	03:06:25	6.79	2.52	03:24:39

of the bright object constraints were violated.

The roll and pitch responses of LRO were plotted for the three data sets, as shown in Figure 8.15. It was observed that NASA's solution separated the maneuver into a roll first, then pitch sequence. It was again observed that a slight discrepancy exists between AttMan prediction and telemetry values, which probably contributed to the large variation in angle error between the two at desired TOT (from Table 8.2).

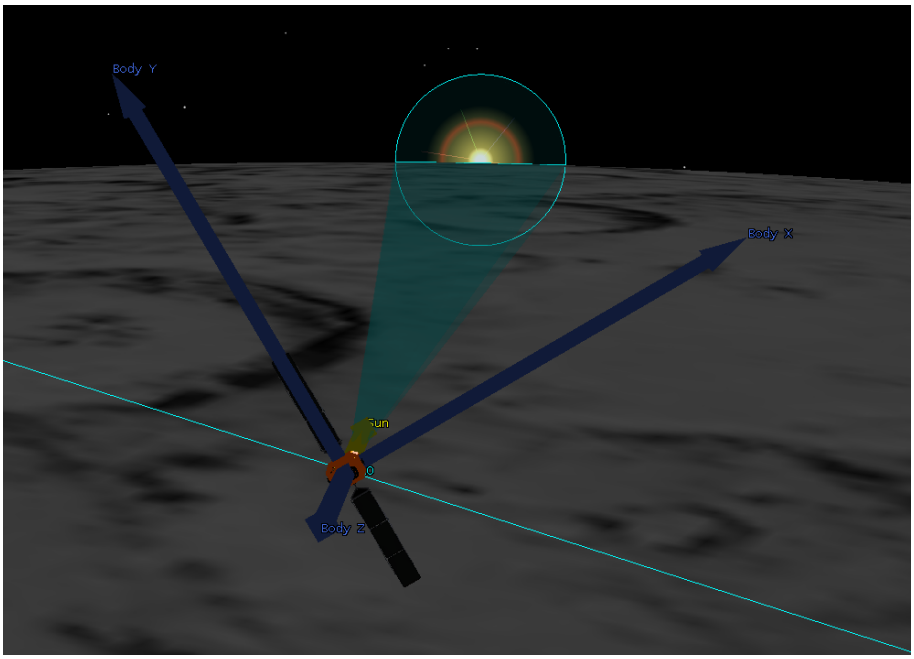

Figure 8.12. STK visual result for Day 321 optimal maneuver.

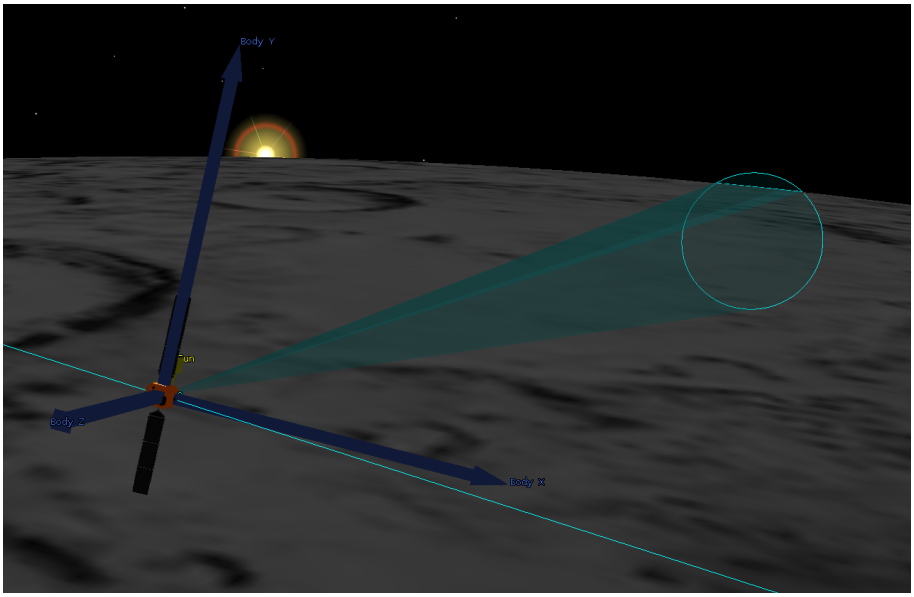

Figure 8.13. STK visual result for Day 321 AttMan maneuver.

The angular velocity time history is shown in Figure 8.16. The inclusion of a higher ending pitch requirement resulted in a more modest overall magnitude of angular velocity when

compared to the roll-heavy example from the previous example. Nonetheless, the full capability of the reaction wheel array is used, allowing the 0.13 deg/s limits imposed by NASA to be exceeded.

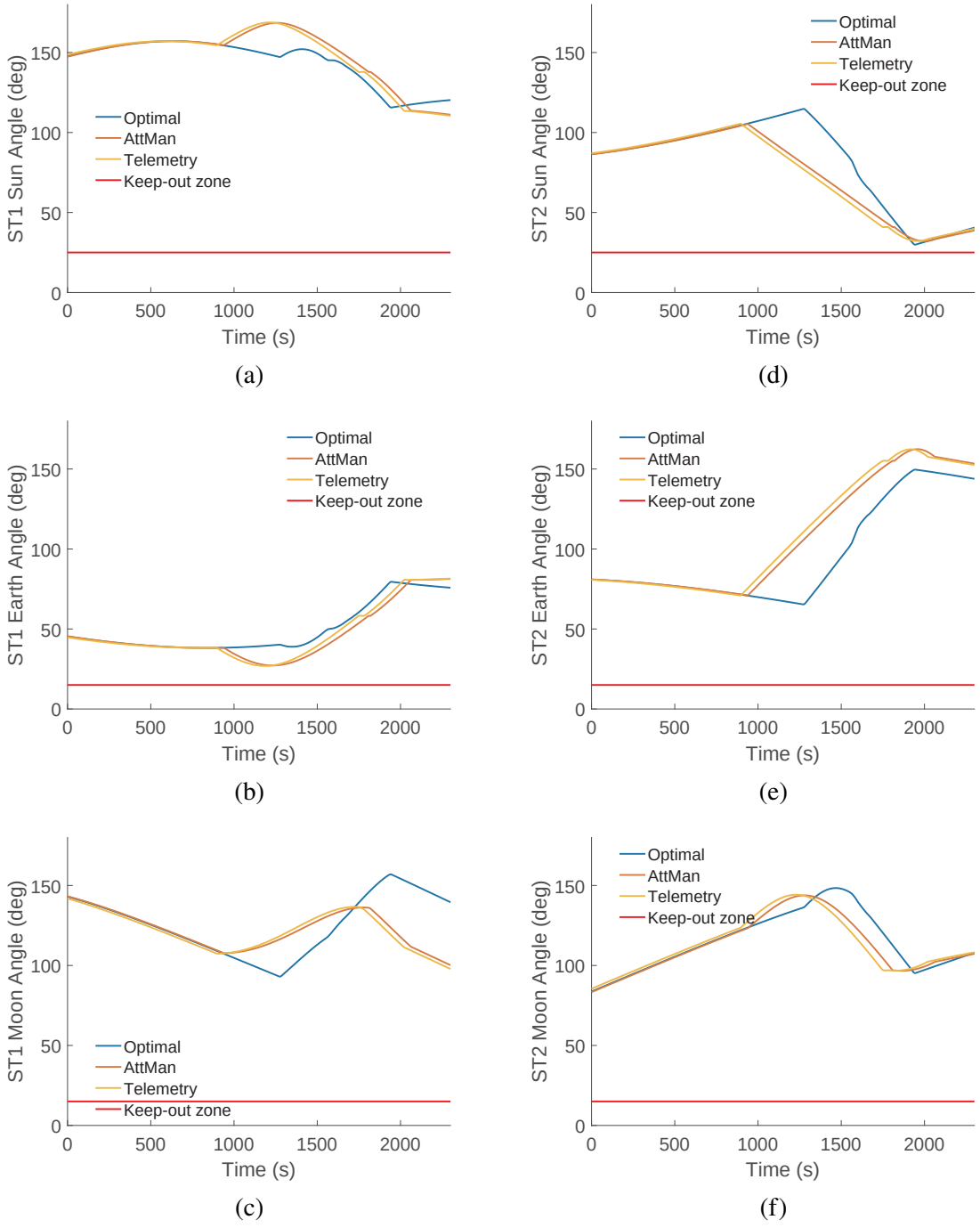

Figure 8.14. Star tracker orientation with respect to the Sun, Earth, and Moon: (a) ST1 to Sun; (b) ST1 to Earth; (c) ST 1 to Moon; (d) ST 2 to Sun; ST2 to Earth; ST2 to Moon.

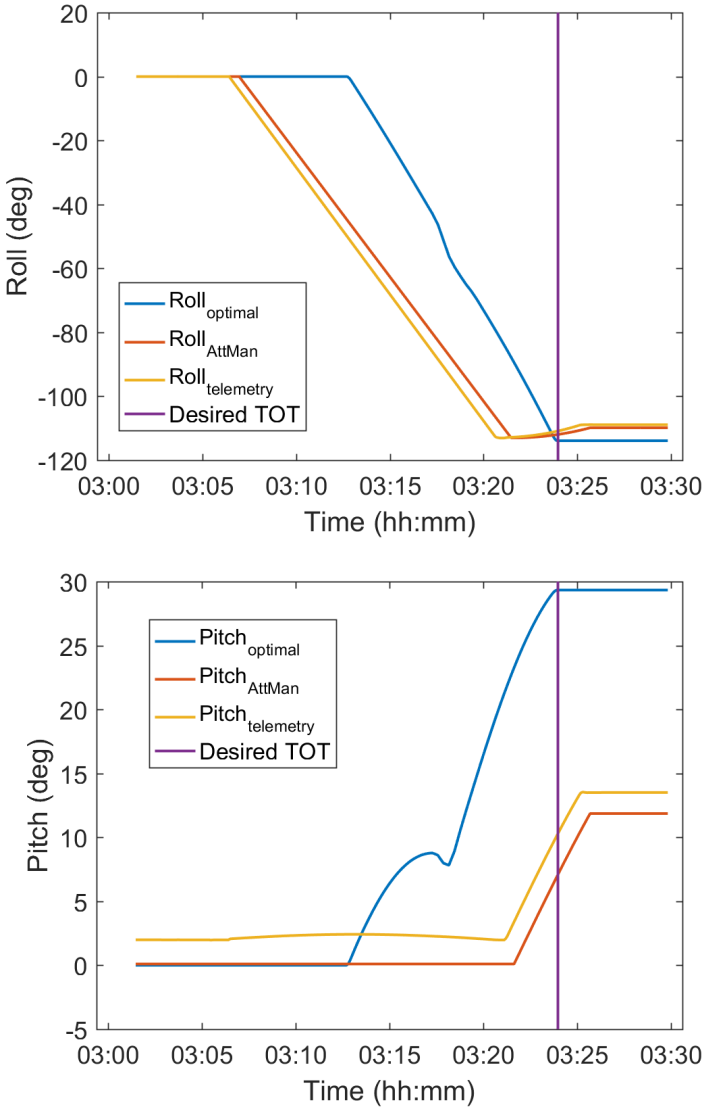

Figure 8.15. Roll and pitch angles for Day 321 maneuver.

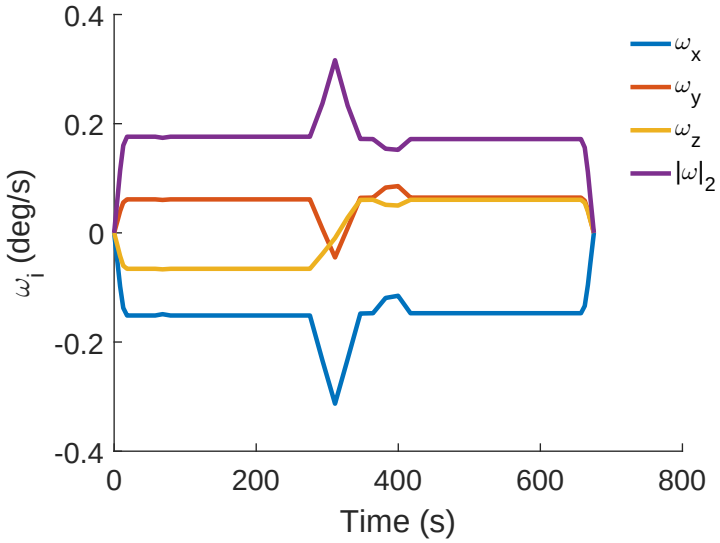

Figure 8.16. Minimum time angular velocity histories for Day 321 maneuver.

8.5.3 Analysis

Unlike the Day 303 maneuver, the Day 321 maneuver had a sizable roll and pitch requirement. Even without the immediate presence of bright object constraints, NASA typically employs a dog-leg maneuver, where roll and pitch can be iteratively adjusted until an acceptable solution is validated through AttMan. It was demonstrated that, by allowing roll and pitch to occur simultaneously, the required maneuver time can be significantly reduced. This simultaneous rotation about more than one-axis is leveraging off-eigenaxis rotation. Figure 8.15 is also very helpful to observe how a non-intuitive solution may oftentimes be the optimal one, as the angle profiles are not typical by any means. However, that does not mean the flight profile is any harder for the ADCS to execute.

8.6 Summary

Applying optimal control theory to NASA's LRO is an exciting possibility which could prove to enhance its scientific gathering capability. No hardware changes are required for the LRO. The guidance trajectory is the only modification suggested. The inner loop ADCS for LRO can still work as it always has and the optimal control solution can be patched into NASA's dynamics model to include any additional, lower order constraints, such as reaction wheel friction. Overall, this case study demonstrated the viability of including optimal control considerations into the mission planning process. The demonstrated time that could be saved also applies for the return trajectory to nadir, following the target capture. Streamlining minimum-time solutions for day-to-day operation could greatly increase the amount of data that could be collected as well as significantly reduce the burden on the planning process by reducing the overall footprint of the LOLA science missions team in iteratively planning missions.

CHAPTER 9:
Conclusion and Future Work

Just like all programs, space applications must consider the cost, schedule, and performance of any satellite. Space platforms are expensive, complicated, and need to be reliable. With such a high cost associated with space applications, most notably science gathering satellites, it is imperative to try and gain the most value possible. This thesis has addressed several high reaching questions:

1. How can one prioritize or assign a value to a specific target?
2. Can target selection be accomplished autonomously?
3. Once a target is selected, how can a rapid slew be performed in order to maximize the number of total targets captured?
4. How can the satellite autonomously take into consideration operational path constraints, such as bright object avoidance?

This thesis has demonstrated that automated target selection strategy could be developed based on bipartite graph theory. The input of the system would be the desired science objectives and the output would be the quaternion associated with the most valuable target. The required control and trajectory of the satellite could then be solved using optimal control theory. The advantages of using optimal control theory in this case are twofold. Firstly, one can solve for a minimum time solution, thereby solving for the most rapid slew possible and opening up the opportunity to increase the number of targets collected. Secondly, the optimal control framework allows for the autonomous control solution while taking into account operational constraints.

Following the bipartite graph example for a sample LRO target selection, the remaining content of the thesis had to be developed and integrated to ultimately solve for a rapid slew maneuver of the LRO while accounting for bright object constraints. It was shown that applying the concepts laid out in this thesis can save up to 50% of the required slew time for the satellite to go from nadir to target. In this case, results were obtained using an LRO-specific mission set (through the use of its LOLA instrument). The next steps could be to compare the presented rapid slew techniques to the remaining six instruments to evaluate

how much time can be saved.

Although there is no necessity to apply this to the LRO, future academic work of this thesis could address a Real Time Optimal Scheduler, or RTOS. The RTOS could act as the interface between the output of the Bipartite Expert System and the minimum-time maneuver program. The job of the RTOS would be to update the available targets at any given time, based on the satellite orbit as well as de-prioritize any target once it is captured. For example, if an instrument collects on a given target because it was deemed the most valuable, it needs to be updated as a zero priority immediately following the collect. The satellite could then collect on what has previously been selected as the second most valuable target.

The target selection and rapid slew maneuvers presented in this thesis were ultimately tied to the LRO. The LRO is an extremely successful satellite that continues to provide scientific data that contributes to a better understanding of the lunar surface, its history, and a more general understanding of human spaceflight for future terrestrial missions. Data gathered from LRO will likely help humankind habitat Mars some day. By incorporating the concepts explored in this thesis, the mission set of LRO could be even further expanded at the same, or even lower, expense to NASA. Not only can the amount of obtainable science collection increase, the manpower placed on the planning portion within the Missions Operations Center and science mission teams can be reduced. In order to show what a possible operational flow could look like for a spacecraft (using LRO as an example) a new state of practice can be proposed, as shown in Figure 9.1.

The human de-confliction, weekly collection plan, and slew planning tool (AttMan) observed in the LRO current state of practice has been replaced by the Bipartite Expert System and RTOS. As previously mentioned, there is closed loop feedback between RTOS and the bipartite system so the available targets can be updated in real-time. In Figure 9.1, the AttMan software has been included as an optional verification tool, but the actual trajectory solution of the satellite would be obtained via the optimal control framework, and, for simplicity, termed the "LippMan" minimum time maneuver program. Ideally, for future spacecraft, commands would not have to be up-linked in real-time. Rather, this could be a recurring process on board the satellite itself. In this scenario, one would only need to provide the target or calibration target request directly to the satellite. The on board

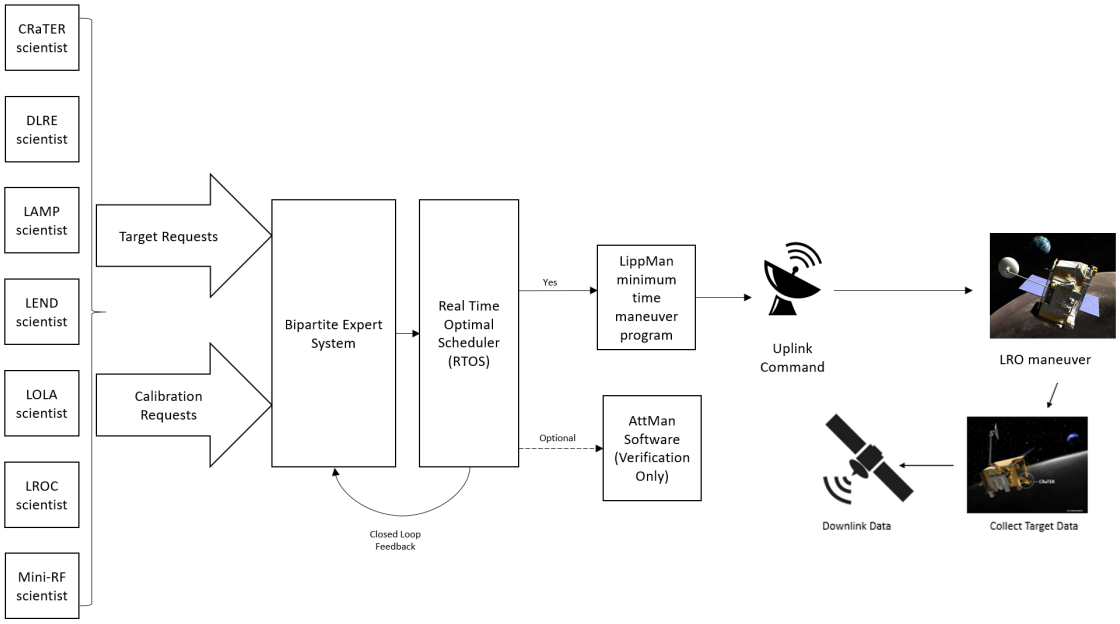

Figure 9.1. Proposed state of practice for the LRO. Adapted from [7].

processor, then, could include the bipartite system, RTOS, and the minimum time maneuver program.

Additional future work can include inputting the optimal solutions obtained in Chapter 8 into AttMan to test against other operational constraints, such as power and thermal. Along these same lines, future higher-fidelity optimal control problem formulations can try to model these additional constraints. Another concept which can be explored is how to account for when the Moon stands between the LRO and Sun or Earth, within the context of the optimal control problem. By properly formulating that problem, one would not have to manually check the solution to see if a seemingly 'violated' bright object constraint occurred while the bright object was blocked by the Moon. Finally, the concept of allowing for a changing yaw while pointing at the target can be further studied for instruments in which the science team has no preference on orientation of the instrument field-of-view.

Although some may think adding autonomous capability to space applications is too complex or unnecessary, it should still be explored. The instrument, sensor, and computing capability on board spacecraft has rapidly increased in recent history. By autonomously selecting targets and performing rapid slews, efficiency and data collection can increase

while decreasing both manpower and actual cost of operations of the spacecraft. One only needs to look at the automobile industry to observe how these concepts may help with space applications. Fifty years ago, people probably never actually thought a car could autonomously parallel park itself; however, by studying and understanding concepts tied to autonomous control and control feedback, a self-parking car is available, which decreases human-interface complexity as well as the chance of a collision with another vehicle. The inclusion of modern concepts into space applications can further enhance an already successful industry!

List of References

[1] NASA/Jet Propulsion Laboratory. California Institute of Technology. [Online]. Available: https://www.jpl.nasa.gov/missions/explorer-1/. Accessed Oct. 26, 2017.

[2] Karl Hille, ed. NASA. [Online]. Available: https://www.nasa.gov/mission_pages/LRO/overview/index.html. Accessed Jan. 11, 2017.

[3] G. Chin *et al.* (2007). *Lunar Reconnaissance Orbiter Overview: The Instrument Suite and Mission*. [Online]. Available: http://citeseerx.ist.psu.edu/viewdoc/download?doi=10.1.1.544.5839&rep=rep1&type=pdf

[4] "Views of the lunar South Pole/Lunar Reconnaissance Orbiter." Image. Accessed Dec. 13, 2017. [Online]. Available: https://lunar.gsfc.nasa.gov/images/polardata-white-large.jpg

[5] LRO Program Office, private communication, Dec. 2016.

[6] J. Sedlak and M. Houghton, "Lunar reconnaissance orbiter (lro) attitude maneuver planning," *Proceedings of the 21st International Symposium on Spaceflight Dynamics*, Toulouse, France, 2009.

[7] Chris Meaney. NASA photograph. NASA. [Online]. Available: http://crater.unh.edu/. Accessed Oct. 26, 2017.

[8] J. Sedlak, "Flight dynamics (fd) task order 178 lunar reconnaissance orbiter (lro) attitude maneuver (attman) utility functional specifications," Goddard Spaceflight Center, Greenbelt, MD, 2008.

[9] J. Garrick, "Lunar reconnaissance orbiter project, lro attitude control system (acs) alignments and coordinate systems," Goddard Spaceflight Center, Greenbelt, MD, 2007.

[10] Neerav Shah and others. PoleCATS. [Online]. Available: https://ntrs.nasa.gov/archive/nasa/casi.ntrs.nasa.gov/20100014880.pdf. Accessed Sep. 29, 2017.

[11] LRO Program Office, private communication, Oct. 2017.

[12] N. Biggs, *Graph Theory 1736-1936*. Oxford: Clarendon Press, 1976.

[13] "Konigsberg bridges." Image. Accessed Dec. 13, 2017. [Online]. Available: http://www-history.mcs.st-andrews.ac.uk/Extras/Konigsberg.html

[14] The Seven Bridges of Konigsberg. [Online]. Available: https://www.math.ku.edu/~jmartin/courses/math105-F11/Lectures/chapter5-part1.pdf. Accessed Oct. 26, 2017.

[15] D. B. West, *Introduction to Graph Theory*. Upper Saddle River, NJ: Prentice Hall, 1996.

[16] A. Asratian, *Bipartite graphs and their applications*. NY: Cambridge University Press, 1998.

[17] B. Wie, *Space Vehicle Dynamics and Control, Second Edition*. Reston, VA: American Institute of Aeronautics and Astronautics, 2008.

[18] M. J. Sidi, *Spacecraft Dynamics and Control: A Practical Engineering Approach*. New York: Cambridge University Press, 2000.

[19] M. F. Walters, "A management option for momentum control systems," Master's thesis, Dept. of Mechanical and Aerospace Engineering, Naval Postgraduate School, Monterey, CA, 2016.

[20] J. Garrick, "Lunar reconnaissance orbiter project, lro attitude control system (acs) algorithm specifications," Goddard Spaceflight Center, Greenbelt, MD, 2008.

[21] Spirent. [Online]. Available: https://www.spirent.com/Blogs/Positioning/2010/August/2010-08-16_What_is_an_ephemeris. Accessed Nov. 5, 2017.

[22] JPL Horizons Solar System Dynamics Web Interface. [Online]. Available: https://ssd.jpl.nasa.gov/horizons.cgi. Accessed Dec. 8, 2017.

[23] F. L. Markley and J. L. Crassidis, *Fundamentals of Spacecraft Attitude Determination and Control*. New York: Springer, 2014.

[24] H. B. Hablani, "Target acquisition, tracking, spacecraft attitude control, and vibration suppression with ipfm reaction jet controllers," *Proceedings of the AIAA Guidance, Navigation, and Control Conference*, 1992.

[25] H. B. Hablani, "Attitude commands avoiding bright objects and maintaining communications with ground station," *Journal of Guidane, Control, and Dynamics*, vol. 22, no. 6, pp. 759–767, 1999.

[26] G. Mengali and A. Quarta, "Spacecraft control with constrained fast reorientation and accurate pointing," *The Aeronautical Journal*, vol. 108, no. 1080, pp. 85–91, 2004.

[27] Y. Kim, M. Mesbahi, G. Singh, and F. Y. Hadaegh, "On the constrained attitude control problem," *Proceedings of the AIAA Guidance, Navigation, and Control Conference*, Paper number: AIAA-2004-5129, 2004.

[28] H. C. Kjellberg and E. G. Lightsey, "Discretized constrained attitude pathfinding and control for satellites," *Journal of Guidance, Control, and Dynamics*, vol. 36, no. 5, pp. 1301–1309, 2013.

[29] H. C. Kjellberg and E. G. Lightsey, "Discretized quaternion constrained attitude pathfinding," *Journal of Guidance, Control, and Dynamics*, vol. 39, no. 3, pp. 710–715, 2016.

[30] J. D. Biggs and L. Colley, "Geometric attitude motion planning for spacecraft with pointing and actuator constraints," *Journal of Guidance, Control, and Dynamics*, vol. 39, no. 7, pp. 1669–1674, 2016.

[31] S. Tanygin, "Fast autonomous three-axis constrained attitude pathfinding and visualization for boresight alignment," *Journal of Guidance, Control, and Dynamics*, vol. 40, no. 2, pp. 358–370, 2017.

[32] C. Xiaojun, C. Hutao, C. Pingyuan, and R. Xu, "Large angular autonomous attitude maneuver of deep spacecraft using pseudospectral method," 3rd International Symposium on Systems and Control in Aeronautics and Astronautics (ISSCAA), Harbin, China, 2010.

[33] R. G. Melton, "Hybrid methods for determining time-optimal, constrained spacecraft reorientation maneuvers," *Acta Astronautica*, vol. 94, no. 1, pp. 294–301, 2014.

[34] D. Spiller, L. Ansalone, and F. Curti, "Particle swarm optimization for time-optimal reorientation with keep-out cones," *Journal of Guidance, Control, and Dynamics*, vol. 39, no. 2, pp. 312–325, 2016.

[35] I. M. Ross, *A Primer on Pontryagin's Principle in Optimal Control*. San Francisco, CA: Collegiate Publishers, 2015.

[36] L. S. Pontryagin, V. G. Boltyanskii, R. V. Gamkrelidze, and E.F. Mishchenko, *The Mathematical Theory of Optimal Processes*. New York, London: Interscience Publishers, John Wiley & Sons, Inc, 1962.

[37] I. M. Ross and M. Karpenko, "A review of pseudospectral optimal control: from theory to flight," *Annual Reviews in Control*, vol. 36, no. 2, pp. 182–197, 2012.

[38] I. M. Ross and Q. Gong, "Guess-free trajectory optimization," AIAA/AAS Astrodynamics Specialist Conference and Exhibit, AIAA paper: 2008-6273, Honolulu, HI, 1992.

[39] M. Karpenko and R. J. Proulx, "Experimental implementation of riemann-stieltjes optimal control for agile imaging satellites," *Journal of Guidance Control and Dynamics*, vol. 39, no. 1, pp. 144–150, 2016.

[40] N. Bedrossian, S. Bhatt, W. Kang, and I. M. Ross, "Zero-propellant maneuver guidance," *IEEE Control Systems Magazine*, pp. 53–73, 2009.

[41] M. Karpenko, S. Bhatt, N. Bedrossian, and I. M. Ross, "Flight implementation of shortest-time maneuvers for imaging satellites," *Journal of Guidance, Control and Dynamics*, vol. 37, no. 4, pp. 1069–1079, 2014.

[42] I. M. Ross, Q. Gong, M. Karpenko, and R. J. Proulx, "Scaling and balancing for faster trajectory optimization," AAS/AIAA Astrodynamics Specialist Conference, Paper number: AAS-17-675, Stevenson, WA, 2017.

Initial Distribution List

1. Defense Technical Information Center
   Ft. Belvoir, Virginia

2. Dudley Knox Library
   Naval Postgraduate School
   Monterey, California